MICROSTRUCTURAL PHASE EVOLUTION IN LASER DEPOSITED COMPOSITIONALLY GRADED TITANIUM CHROMIUM ALLOYS

Jonova Thomas, B.E

Thesis Prepared for the Degree of

MASTER OF SCIENCE

UNIVERSITY OF NORTH TEXAS

May 2016

APPROVED:

Thomas W. Scharf, Major Professor

Rajarshi Banerjee, Committee Member

Marcus L. Young, Committee Member

Andrey Voevodin, Chair of the Department of Material Science and Engineering

Costas Tsatsoulis, Dean of the College of Engineering and Toulouse Graduate School

Thomas, Jonova. *Microstructural Phase Evolution in Laser Deposited Compositionally Graded Titanium Chromium Alloys*. Master of Science (Material Science and Engineering), May 2016, 134 pp., 9 tables, 75 figures, references, 47 titles.

A compositionally graded Ti-xCr (10≤x≤30 wt%) alloy has been fabricated using Laser Engineered Net Shaping (LENSTM) to study the microstructural phase evolution along a compositional gradient in both as-deposited and heat treated conditions (1000°C followed by furnace cooling or air cooling). The alloys were characterized by SEM BSE imaging, XRD, EBSD, TEM and micro-hardness measurements to determine processing-structure-property relations. For the as-deposited alloy, α-Ti, β-Ti, and TiCr2 (C15 Laves) phases exist in varying phase fractions, which were influential in determining hardness values. With the furnace cooled alloy, there was more homogeneous nucleation of α phase throughout the sample with a larger phase fraction of TiCr2 resulting in increased hardness values. When compared to the air cooled alloy, there was absence of wide scale nucleation of α phase and formation of ω phase within the β phase due to the quicker cooling from elevated temperature. At lower concentrations of Cr, the kinetics resulted in a diffusionless phase transformation of ω phase with increased hardness and a lower phase fraction of TiCr2. In contrast at higher Cr concentrations, α phase separation reaction occurs where the β phase is spinodally decomposed to Cr solute-lean β1 and solute-rich β2 resulting in reduced hardness.

ACKNOWLEDGMENTS

I would like to express my gratitude to my advising professor Dr. Thomas W Scharf who not only gave me the opportunity to continue my graduate studies in Material Science and Engineering a relatively new field to me, but also happened to be one of the greatest mentors I have had the privileged to learn from. His trust in me to apply my ideas at various stages of my research has deeply broadened my understanding of the field and helped me grow as an intellectual person.

I would like to thank Dr. Rajarshi Banerjee for his invaluable knowledge on Ti alloys that help guide this research and generous help in providing access to his laboratory and instrument usage. I would also like to extend my thanks to Dr. Marcus Young for agreeing to be my committee member and providing brilliant suggestions to improve the quality of my research.

I would also like to thank the MTSE departmental staff and Dr. Deep Choudhuri for his help in TEM analysis, Srinivas A M, Bharat .G, Vishal.S, Chris. Y and Calvin .M for their patience in teaching me how to use various equipment's and analyze data from them. I would also like to acknowledge Dr. Victor Ageh and Jon-Erik Mogonye who helped me in FIB lift outs and gave me the push to initiate my research. I am deeply grateful to Andres C Garcia, Michael .L, Hussain Rizvi, Rodolfo .G and everyone else who helped me at every stage of my 2 years as a graduate student at UNT. I would also like to extend a hand of thanks to the supervisors of Center for Advanced Research and technology (CART) at University of North Texas for permitting me to use their equipment. Last but never the least, I would like to thank God, my parents and siblings for their endless support throughout my life without whom, I would not have been where I am today.

TABLE OF CONTENTS

LIST OF TABLES

LIST OF FIGURES

CHAPTER 1

INTRODUCTION AND MOTIVATION

1.1 Introduction

Titanium (Ti) is a lustrous silver white transition metal that is well known for its high strength-to-weight ratio and resistance to corrosion when compared to other metals. Alloys of titanium being much lighter and stronger than other commonly used materials have been widely used in industries especially from naval ships, medicine, aircraft to space technology. Titanium being nontoxic, highly biocompatible along with osseo-compatibility makes it a perfect choice for bio implants.

A survey conducted in 2014 (Fig. 1.1) has stated that about 40% of Ti in markets is being used for aerospace applications in which two third of that is used for air craft engine production (1).

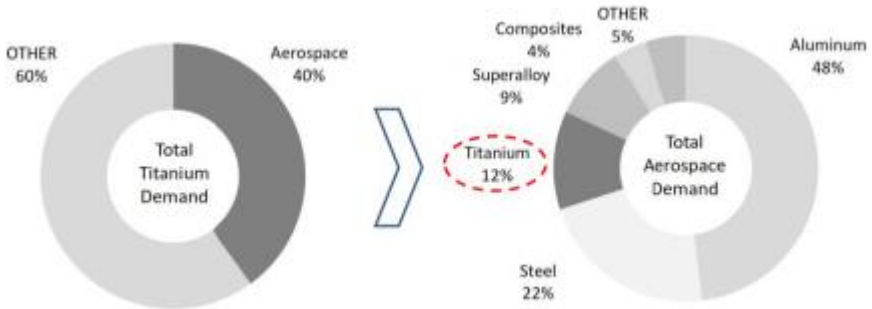

Fig 1.1: Titanium usage in aerospace (1)

The cost of Ti being relatively expensive with respect to other materials available is compromised by mixing or alloying it with other elements. This process of alloying in

turn reduces the cost required for production of parts. For example, heavy steel air frames that were used in aircrafts are now being replaced with Ti alloys. Replacing the commonly used materials with Ti alloys results in benefits of reduced weight, corrosion resistant, and high strength. The reason for Ti and its alloys high corrosion resistance is largely due to its high reactivity to oxygen where it forms a protective oxide layer. Furthermore, Ti alloys are well known for replacing Al parts and lowering life cycle cost of various part production (2,3).

In recent years, the manufacturing of metallic components has been carried out by novel techniques of direct metal fabrication. This manufacturing technology shows great promise, since if perfected, bulk metallic components could be manufactured by net shaping deposition of multiple thin layers using an energy beam (4). Fusing of the metal powders used in this process is carried out using a laser beam of adequate energy. United Technologies Research Center (UTRC) in 1979 were one of the first to pioneer this sort of manufacturing. This process of metal manufacturing is commonly termed as layer glazing (4).

A bilateral use of concepts of stereo lithography and layer glazing led to a new form or rather generation of laser deposition processes for bulk metallic production. Laser Engineered Net Shaping (LENS^{TM}) (5) and direct light fabrication (DLF) (6) processes are part of the above novel processes.

The introduction of LENS^{TM} process was developed by Sandia National Laboratories in the 1990's which led to the eventual commercialization by Optomec Design Company of Albuquerque, New Mexico (7). DLF process was developed at Los Alamos National Laboratories during the early 1990's. Similarity between the two

processes are noteworthy as they both use a laser beam as a heat source to melt metallic powders and create a three dimensional solid of required shape and size as specified by an inputted 3D CAD file.

A large variety of metals and their alloys can be deposited using LENS^{TM} deposition process (5, 6,8). The alloys are deposited from a pre-alloyed blend of element powders to achieve the desired composition. This provides a high potential to reduce production costs. In addition to usage of elemental powder blends, chemically and structurally graded depositions can be achieved within the same sample. The process of fabrication is considered to be extremely useful in order to reduce waste of materials, and power consumption, and to study the change in microstructure over a range of compositions with respect to equilibrium alloy phase diagrams. Studies on elemental powder blends by laser deposition (9, 10) there are relatively few when compared to as cast processes. Some of the early studies of LENS^{TM} depositions were carried out by Takeda et al (9) and Sheen et al (10) having produced Fe-Cr-Ni and Fe-Co-Al alloys, respectively.

Since Ti based alloys having wide applications in medical and aerospace industries, it is expected that LENS^{TM} technology will play a vital role in the future for manufacture of complex and intricate near net shape components. The initial experiments carried out using elemental powders blends with Ti as the primary component has suggested that the important factor deciding the microstructure and the composition homogeneity of the alloy depends on the enthalpy of mixing of the constituent element used (11).

The process of creating graded composition parts has a high potential application in bio implants. Bones have variation in toughness, stress/strain experienced and load bearing along its length. Creation of prosthetics with varying compositions along the length of the implant will result in novel prosthetics with properties as close as possible to the bone that is to be replaced (29). Compositionally graded implants can be created by LENS^{TM} operation by controlling the speed of the flow rate of the powders dispersed from the powder hoppers during deposition, number of layers required for the part, and melt time for the powders to blend with each other.

The main aim of this thesis is to explore the as-deposited and annealed microstructure, phase change and properties of Ti-Cr binary alloy system using the LENS^{TM} system. The range of the alloy system studied is between Ti-10 wt% Cr to Ti-30 wt% Cr. A total of 5 different alloys were produced with an approximate increment of 5 wt% Cr on a single one inch specimen. The Cr composition of the alloy is expected to vary along the length of the specimen. The LENS^{TM} system was chosen for the purpose of the study as it is a comparatively new method of production with respect to as cast alloys. The depositions achieved by LENS^{TM} will be under non-equilibrium conditions due to the rapid heating and cooling of powders. This study will also provide a valuable insight into the change in microstructure with respect to changing composition and heat transfer from the upper regions of the laser deposited powders. Ti-Cr alloys have been selected for study because of its high temperature strength, wear resistance, exceptional oxidation resistance, biocompatibility and its property of hydrogen solubility (12,13,14).

Previous work done by Ho et al stated that for as cast Ti-Cr alloys of Cr content ranging from 5-30 wt%, Ti-20Cr alloys had interesting properties with respect to the other

as cast alloys and could be considered for dental applications as prosthetics (13). Ti-10Cr alloys studied by Hsu et al has shown to have the highest grindability and hardness due to formation of ω phase within the constituent (14). Ti-30Cr alloys exhibit a higher bond strength to fusing with porcelain than all other Ti-Cr alloys and commercially pure Ti due its comparatively low coefficient of thermal expansion (14). When the Cr wt% exceeds 15 wt%, there are formation of Laves phases of $TiCr_2$ (11). The microstructure of the alloys from this system is highly sensitive to the Cr content and the methods of preparation. Unlike the as cast Ti-Cr alloys, the laser deposited Ti-Cr alloys primarily consist of a β stabilized bcc matrix of βTi (Cr) with precipitates of α or $TiCr_2$ formation along the grain boundaries at different compositions (11).

1.2 Objectives

(A) Study the microstructural phase evolution in laser deposited compositionally graded Ti-10Cr to Ti-30Cr alloys.

(B) Determine the structure property relations of the deposited alloys, in particular the effect of the graded microstructure on the hardness of the alloys.

(C) Analyze how various heat treatments change the structure property relations of the graded alloys.

1.3 Organization of Thesis

There are to be a total of 7 chapters within the thesis. The first chapter provides an insight on the introduction to LENS^{TM} deposited alloys and motivation for selecting the particular topic of microstructural evolution of a compositionally graded TiCr alloy prepared by LENS^{TM}. Chapter 2 is a background literature review with introduction to the

microstructure of pure Ti and its alloys, reason for selection of the binary TiCr alloy system, and purpose of heat treatments. In addition, a small review on LENS^{TM} and characterization tools used is presented. Chapter 3 provides a detailed explanation of experimental procedures of processing and characterization of compositionally graded Ti-10Cr to Ti-30Cr alloys. It also details the various conditions and introduction of analysis tools used to fabricate and characterize the alloys. Chapters 4, 5 and 6 are the results and discussion of the processing-structure-property interrelationships for the as-deposited, furnace cooled and air cooled Ti-Cr alloys. Lastly, chapter 7 summarizes the present study and proposes future work that can be carried out later on this alloy system.

CHAPTER 2

BACKGROUND AND LITERATURE REVIEW

This chapter is divided into 4 sections. Section one discusses microstructural changes and the effect of alloying different elements with Ti along with a strong metallurgical focus on the Ti binary alloy system Ti-Cr. Section two is a review of the LENS^{TM} instrument as a tool to fabricate graded specimens with use of elemental powders. Section three provides a brief description on the effects of heat treatment and section four is an introduction of the characterization tools and experiments conducted on LENS^{TM} deposited Ti-Cr.

2.1 Metallurgy of Titanium

2.1.1 Introduction

Titanium and its alloys have numerous use in the aviation, marine, medicinal and chemical industries. The reason for this is their unique collection of properties such as high strength, oxidation and corrosion resistance as well as relatively high fracture toughness (2, 16).

2.1.2 Phases of Titanium

Ti in its pure form generally exists as a hexagonal closed packed (HCP) structure commonly termed as α-Ti. When temperature is raised to 882°C or higher, a phase transformation occurs (17), α-Ti transforms to β-Ti which is a body centered cubic (BCC)

structure. The below figure 2.1 (a, b) depicts the crystal structures of α-Ti and β-Ti, respectively.

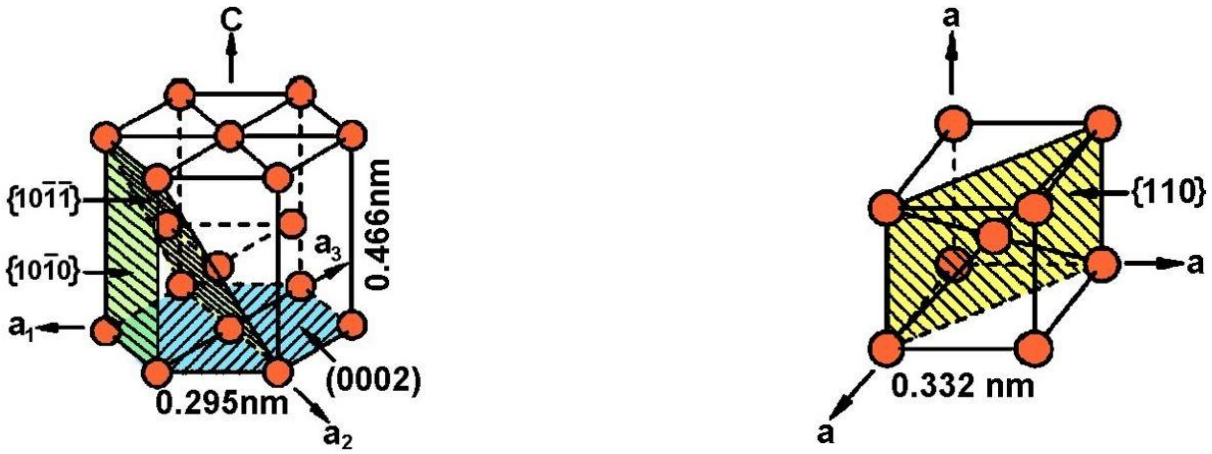

Fig 2.1: Crystal structures of (a) α-Ti (15), (b) β-Ti (15)

2.1.3 Phases of Alloyed Titanium

The alloying element plays a major role in determining a particular phase of the material. Based on the type of alloying element, they can classified into two groups. Elements such as Al, N, and O are known to increase the phase transformation temperatures and thereby stabilize α phase at higher temperatures (39). They are hence termed as α stabilizer elements. Whereas elements such as Mo, V, and Cr are known for decreasing the phase transformation temperatures and stabilizing the β phase more easily. They are termed as β stabilizers.

The phases of Ti alloys are extremely dependent on factors such as temperature, pressure, composition, presence of equilibrium and non-equilibrium phases. Thermodynamics of the lowest free energy state is of concern to determine a particular phase in an alloy system. When non-steady state, kinetics are responsible for the generation of metastable phases.

The possible phases that exist for titanium alloys are:

a) α phase - phase of pure and certain alloys of titanium at room temperature or lower with a HCP structure.
b) β phase - phase of pure as well as alloyed titanium above 882°C with a BCC structure. At this temperature a phase transformation from α to β occurs. The temperature of transformation is specifically denoted as β transus temperature.
c) Martensitic phase - phase that occur due to non-equilibrium cooling. The two phases that are formed are α' and α'' (39). α' is formed due to quick quenching and α'' is known to possess a higher solute concentration with respect to α'.
d) ω phase - a metastable phase formed during the transition from β to α phase. The structure can be hexagonal or trigonal. The phase structure is dependent on the extent of completion of the phase transformation.

2.1.4 Alloying Element Classification in Titanium

Commercially used Ti alloys are classified into various categories on basis of their equilibrium constitutions (2). The two major alloying groups (α and β stabilizers) can be further subdivided into smaller categories on basis of degree of stabilization of the alloying element (17 - 20).

2.1.4.1 α Stabilizers:

a) Certain alloying elements can cause limited solubility in the α phase with a peritectoid transformation of α to β and some other phases. Examples of such elements are B, C, and Al.

b) Complete solubility of certain alloying element in the α phase cause the α phase to extend to the liquid region. Examples of such elements are O and N.

2.1.4.2 β Stabilizers:

a) Elements that can express excessive solubility in β phase and low α phase solubility, such as Mo, and Ta.
b) Few elements can exhibit complete solubility in both α and β phase, such as Zr and Hf.
c) β eutectoid elements that show limited solubility in β phase. The transformation usually occurs from β to α and some other compound or intermetallic, such as Cr, Fe, Cu, and Ni.

2.1.5 Alloy Classification on Industrial Basis

The alloys used in industries for commercial purposes are broadly classified into three categories: α alloys, β alloys and α+β alloys. The compositions of the α+β alloys dictates the phase that will be dominating, although they consist of both α and β alloy elements, the more dominating phase is β phase than α phase.

2.1.5.1 α Titanium Alloys

These include pure Ti and its alloys having a stable HCP structure at room temperature. The alloying elements of this group are strictly α stabilizers. These alloys usually do not undergo heat treatment but are known for their high strength and toughness (21). Small amounts of β stabilizing elements are usually added within the α-Ti alloys to help in the better manipulation of the microstructure (22).

2.1.5.2 α+β Titanium Alloys

Alloys having larger proportion of α phase with respect to β at room temperature fall into these categories. They exhibit martensitic phase transformation when quenched from a temperature above the β transus temperature. The higher the concentration of β stabilizers, the greater the hardenability of the alloy. Lower concentration of β stabilizers in Ti alloys is preferred for weldability and heat resistance applications. Ti-6Al-4V is an all-purpose α+β Ti alloy. A majority of production of Ti alloys in industries is dedicated to Ti-6Al-4V production.

2.1.5.3 β Titanium Alloys

These are alloys that retain β phase at room temperature upon quenching from above the β transus temperature (25). Addition of β stabilizing elements could create martensitic phases. These alloys are usually heat treated to generate dual α and β phase which generally provides the desired mechanical or other properties. Solution heat treating is carried out for most of these alloys preventing the need of early processing (3, 2, 21). Heat treatment of these alloys also lead to increase in hardenability, reduction in stresses during manufacture and change in phases (22).

2.1.6 Binary Titanium Systems

The binary Ti-X system taken into study for this thesis is the Ti-Cr alloy system that has been compositionally graded on basis of weight percent to range between Ti-10Cr to Ti-30Cr. The Ti-Cr alloy system is classified as a β stabilized Ti alloy.

2.1.6.1 Ti-Cr System

Chromium is a beta-eutectoid element. From the phase diagram of Ti-Cr alloy system shown in Figure 2.2., it is evident that the solid phases of the system are α-Ti, β-

Ti and $TiCr_2$ polymorphs. $TiCr_2$ has been determined as an intermetallic phase that occurs only with the increase in Cr composition. The intermetallic $TiCr_2$ exists as Laves phase of either α-$TiCr_2$ (C15), β-$TiCr_2$ (C36), or ϒ-$TiCr_2$ (C14) (23, 24). Prior studies on this system has stated that β and ϒ $TiCr_2$ have hexagonal symmetry (Space group #194: $P6_3/mmc$), while α $TiCr_2$ has cubic symmetry (Space group # 227: Fd-3m).

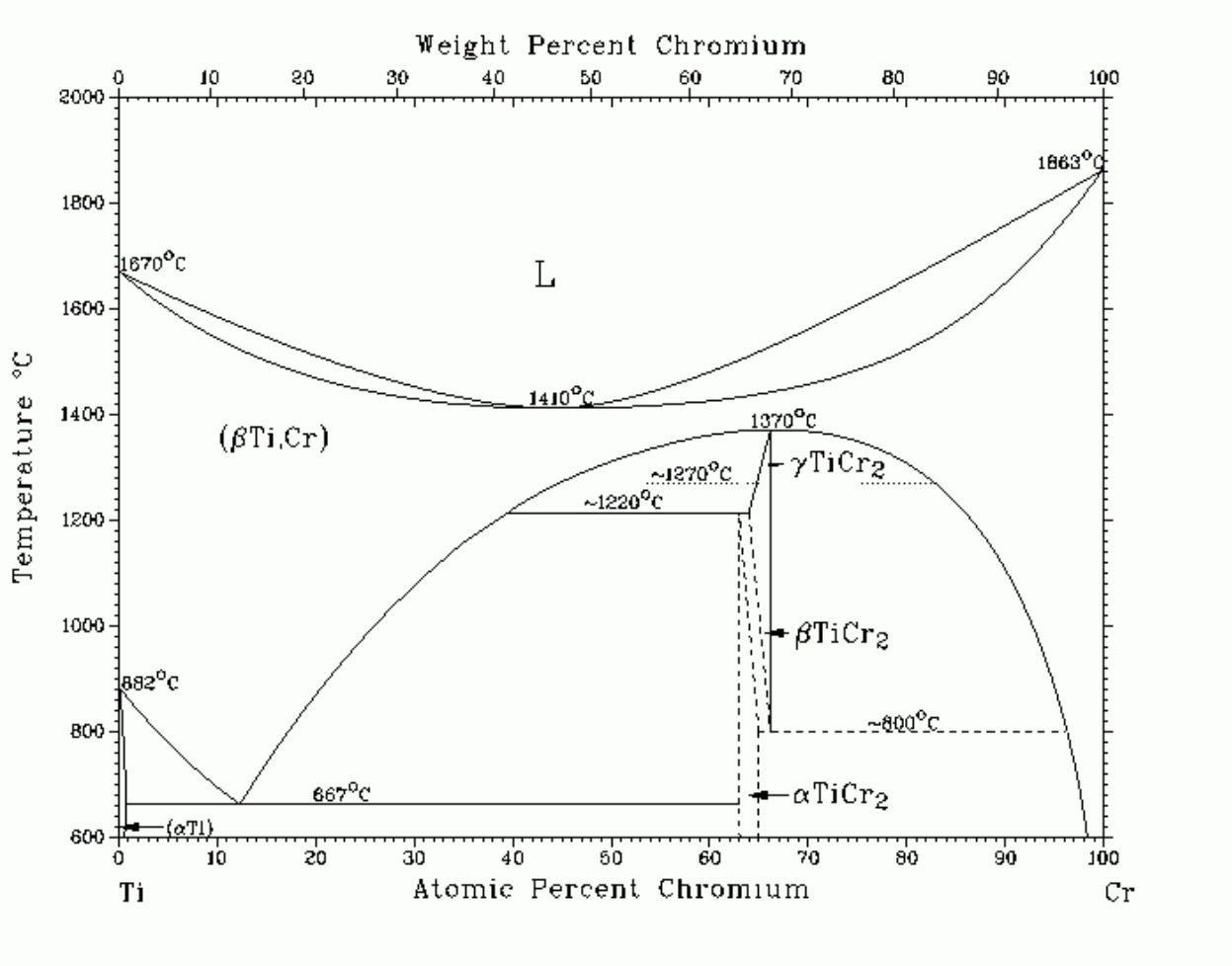

Fig 2.2:- Ti-Cr Equilibrium Phase Diagram (5)

The Ti-Cr binary alloy system has a eutectoid reaction at lower concentrations of Cr that causes β-Ti to transform into α-Ti and $TiCr_2$. The eutectoid temperature being at 667°C implies that the presence of $TiCr_2$ phase can be noticed at a temperature below the eutectoid temperature. The formation of an intermetallic phase is relatively sluggish

and slow and hence not observed below 5wt% (2, 33, 34). $TiCr_2$ intermetallic phase is well known to increase the hardness in alloys that inevitably reduces the ductility of the system. Depending on the use of the alloy $TiCr_2$ phase may or may not be preferred (2).

The Ti-Cr binary alloy system has a eutectoid reaction at lower concentrations of Cr that causes β-Ti to transform into α-Ti and $TiCr_2$. The eutectoid temperature being at 667°C implies that the presence of $TiCr_2$ phase can be noticed at a temperature below the eutectoid temperature. The formation of an intermetallic phase is relatively sluggish and slow and hence not observed below 5wt% (2, 33, 34). $TiCr_2$ intermetallic phase is well known to increase the hardness in alloys that inevitably reduces the ductility of the system. Depending on the use of the alloy $TiCr_2$ phase may or may not be preferred (2).

Unlike the other β stabilizing elements, α’ has been the only reported martensitic phase that occurs, the commonly seen α’’ has not been observed when the system is cooled from a temperature above β transus rapidly (35-37). Welsch G et al (16) and Luhman et al (37) stated that athermal ω will substitute α’ when the composition of Cr in the system exceeds 7wt% and that β phase is entirely retained once Cr wt% exceeds 11wt%. The reason for this change is because Cr is a β stabilizing element when alloyed to titanium.

It has also been observed that at higher Cr content in the Ti-Cr alloy system, a spinodal decomposition of the Cr to β1 solute lean and β2 solute rich tend to occur due to the presence of a large miscibility gap (11, 35, 38).

Studies done by G Hari Narayan et al (32) stated that for a Ti-15Cr alloy, the phase separation process in metastable β phase is a transition reaction, in other words β1+β2

is metastable when compared to ω+β or α+β. ω phase formation can be manipulated into the Ti-Cr system via appropriate heat treatments leading to phase separation, a mode of β decomposition

2.2 Laser Engineered Net Shaping (LENS^{TM})

LENS^{TM} processing is a methodology that is used to fabricate metal parts or alloys using a three dimensional solid model in Computer aided Design (CAD). This process of fabrication is quite dependable and efficient when compared to conventional methods. The rapid cooling or solidification improves the microstructure, mechanical properties and enable homogeneous powder distribution during part creation. An Nd-YAG laser is commonly used as the laser for a specified part deposition.

The study done on Fe-Cr-Ni alloys system (9); an alloy of three different compositions were alloyed by laser deposition on a substrate with varying Cr:Ni ratios. The ratios that were used are 13:6, 18:9 and 25:20. These ratios were specifically chosen on basis of Schaeffer diagrams of martensitic, austenite/martensitic ferrite and austenite/ferrite microstructures (9). Two mechanisms of production were involved: one used a single hopper while the other used a triple hopper assembly. The conclusion reached by these authors are that the homogeneity of the laser deposited alloy depends directly on the melt time which indirectly states its dependency on travel speed, and point of powder impingement. A more recent study conducted on the Fe-Co-Al system (10) aimed at studying the influence of cobalt on pitting resistance of Fe-Co-Al alloys deposited by LENS^{TM}. Deposition of the ternary system was carried out with the help of a novel triple hopper powder feeder system that has automatic calibration for the powder flow rates.

The purpose of laser engineering net shaping is that many different alloy

compositions can easily be deposited when compared to other deposition techniques. A 3D CAD solid shape of the required specimen is loaded into the computer and the metallic powders required for the process are typically a size range between 50μm-150μm (-100/+325 mesh). The Nd-YAG laser along with the powder from the feeder and CAD file specifying the number of layers are used to create an object of necessary size. A detailed explanation of how the LENS^{TM} system work is provided in chapter 3.

2.3 Heat Treatment

Heat treatment of Ti and Ti alloys are carried out for several different reasons. The positive attributes of heat treatment include reduced stresses developed during fabrication process, better combination of ductility and structural stability, and increase in strength. Other advantages include prevention of preferential chemical attack in corrosive environment (25).

The α and near α alloys do not under go much change in microstructure. This implies that high strength cannot be developed in α alloys by heat treatment. However, the α+β and β alloys undergo a microstructural change with respect to heat treatment (22). This leads to the conclusion that stress relieving and hardness variations can occur due to the change in phase or microstructure due to heat treatments.

In α+β Ti alloys, an isothermal ω phase that is usually undesired can be formed when cooled from annealing temperature, while in β-Ti, the β phase largely decomposes fairly easily and transform mostly to the α phase (25). This occurs since the β phase is a metastable phase.

The β annealing is carried out at various temperatures above the β transus temperature of the alloy to improve the fracture toughness of Ti alloys. . This β annealing

is usually carried out at a temperature slightly above the β transus temperature to prevent grain growth. The time held during annealing is dependent on the thickness of the sample (25). Air cooling or water cooling will help to prevent formation of phase at β grain boundaries.

2.4 Material Characterization Methods

2.4.1 X-Ray Diffraction

X-Ray diffraction is carried out to determine the crystallographic phases of the deposited materials. An X-ray source of Cu kα generated by 40KLV and 44mA with a wavelength of 4.54Å is typically used. The diffracted rays are received to the receiver at different angles (Bragg angles) and different intensities. A further explanation on the working procedure, processing and results are discussed in chapters 3 and 4.

2.4.2 Scanning Electron Microscopy (SEM)

SEM is used for imaging of the surface microstructures for all Ti-Cr compositions. Imaging in the SEM is carried out in both Secondary Electron imaging (SE), Back Scattering Electron imaging (BSE) modes. A more detailed explanation on use and results are discussed in chapters 3, 4, 5 & 6.

2.4.3 Energy Dispersive Spectroscopy (EDS)

Being a surface analysis technique, EDS inside the SEM is used to determine the composition of a particular phase at an area of interest in conjunction with the various SEM imaging modes. . The compositional information attained can be used to gauge where the phases exist on the equilibrium phase diagram. A more detailed explanation along with experimental results are discussed in chapters 3, 4, 5 & 6.

2.4.4 Electron Back Scatter Diffraction (EBSD) Mapping

EBSD, also known as Orientation imaging microscopy (OIM), is also acquired inside the SEM using and EBSD detector. EBSD can be used to determine the crystallographic orientation of polycrystalline and single crystal materials. Phase fractions, crystallographic grain orientation relationships, and grain size can also be determined by EBSD. A detailed study of the EBSD scans at various compositions are described in chapters 3, 4 & 5.

2.4.5 Vickers Micro-Hardness Testing

A Vickers hardness machine is used to determine the mechanical hardness of a specimen. Individual hardness values can be measured corresponding to different compositions and microstructures of the specimen. Acquiring hardness values and correlating them to the XRD, SEM, EDS, and EBSD results will allow structure-property relations to be determined for particular phases and compositions for the compositionally graded LENS^{TM} deposited specimens. Further explanation on the testing and results are discussed in chapters 3, 4, 5 & 6.

2.4.6 Dual Beam Focused Ion Beam

Dual Beam Focused Ion Beam (FIB)-SEM is used for the preparation of an electron transparent cross-section to be subsequently analyzed in TEM. Milling of the area of interest on the sample is carried out by ion milling process in the SEM chamber. A more detailed explanation is discussed in chapter 3, 5 & 6.

2.4.7 Transmission Electron Microscopy (TEM)

TEM imaging and analysis is done on the area of interest made electron transparent by FIB sectioning. The purpose of taking various images and microscopic diffraction at high spatial resolution is explained in more detail in chapters 3, 5 & 6.

CHAPTER 3

MATERIALS AND EXPERIMENTAL PROCEDURE

3.1 Fabrication of the Alloy

The compositionally graded Ti-10Cr to Ti-30Cr alloy was composed of 5 regions with a targeted increase in 5 weight percent of Cr per region. The Ti and Cr powders had a mesh size of 150. This size was chosen to enable a free and smooth flow during the process of making the sample with the Optomec LENS^{TM} 750 system.

Two containers each containing 300 grams of Ti-10Cr and Ti-30Cr powders were prepared on the basis of weight percentage. The first container consisted of 90% of Ti and 10% of Cr (weight percentage), while the second container was loaded with 70% Ti and 30% Cr (weight percentage). Both the containers were placed on a ball milling machine that uses a twin roller mixer. The containers were ball milled for about 4 to 6 hours at a speed of 300 revolutions per minute (rpm). Doing this achieves a homogeneous mixture of the powders in the container before starting the LENS^{TM} deposition.

#	SAMPLE	Ti (wt%)	Cr (wt%)
1	Ti10Cr	90	10
2	Ti15Cr	85	15
3	Ti20Cr	80	20
4	Ti25Cr	75	25
5	Ti30Cr	70	30

Table 3.1: Composition of Samples to be Prepared

Caution must be taken to prevent the powder mixing for a long duration on the ball mill as this may lead to oxidation of the powders. The sample compositions are listed in Table 3.1

3.2 Laser Engineered Net Shaping (LENS^{TM})

LENS^{TM} is an additive manufacturing technology used to build 3-Dmaterials. Information for each layer of powdered material is sent to the manufacturing unit which carries out the process by initiating stage movements. The laser rastering on the powdered materials blown in from the powder feeder hopper, semi melts the particles and bonds them during solidification. This process when coupled with movement of the stage enables the production of a part of desired shape and size. After the deposition of each layer, the deposition head moves upward with respect to the CAD file provided in order to start the next layer deposition, i.e. bottom-up deposition (27, 28). The entire process is carried out in a glove box filled with argon gas. The argon gas is constantly purged during the process to circumvent metallic oxidation. A substrate metal is provided for deposition of the sample. Most commonly used substrate for Ti alloy deposition is Ti-6Al-4V, 6 mm thickness, which is selected due to its low cost, ease in availability and good match with the deposited Ti-Cr alloy. Powders blown from the feeders at different speed rates can be attained by changing the amps sent to the hopper onto a substrate. With the help of a laser the blown powders are semi melted and cooled rapidly enabling the formation of an alloy of desired composition. Changing the amps sent to the feeder will determine the composition of the build.

3.2.1 Instrument Parts

The different parts of the LENSTM system is shown in Fig 3.1. The laser cavity is placed above the glove box or controlled atmosphere chamber with an ante chamber on the right for introduction of the substrate in the machine. The two powder feeders are shown on the left of the system.

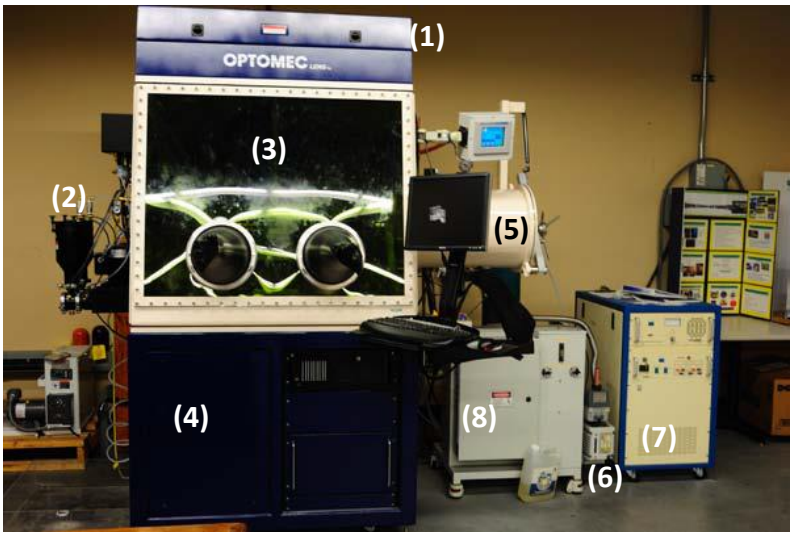

(1) Laser Cavity and Beam delivery system
(2) Powder Feeders
(3) Controlled Atmosphere Process Chamber
(4) Ar Recirculation and Power distribution Unit
(5) Ante Chamber
(6) Vacuum pump
(7) Laser Power unit
(8) Dri-Train System

Fig 3.1: The LENS™ 750 system at the University of North Texas.

The location and setup of the argon air supply, vacuum pump, laser power unit, air circulation system, and power distribution system are as indicated above.

3.2.2 Laser Cavity

The power for laser generation is provided from the Laser unit which is then sent to the power distribution unit eventually entering the laser cavity. The Laser Cavity on top of glove box is shown in Fig 3.2. The laser is set to be converged onto the objective lens with the help of turning mirrors. The objective lens within the deposition head is adjusted in a manner so that the focal point of both the lens and the four converging delivery nozzles is almost if not the same. The power of the laser for deposition depends on a

number of factors such as the powder being used, the flow of the powder, the powder cloud formed when processing is taking place, and the turning of each mirror and the objective lens.

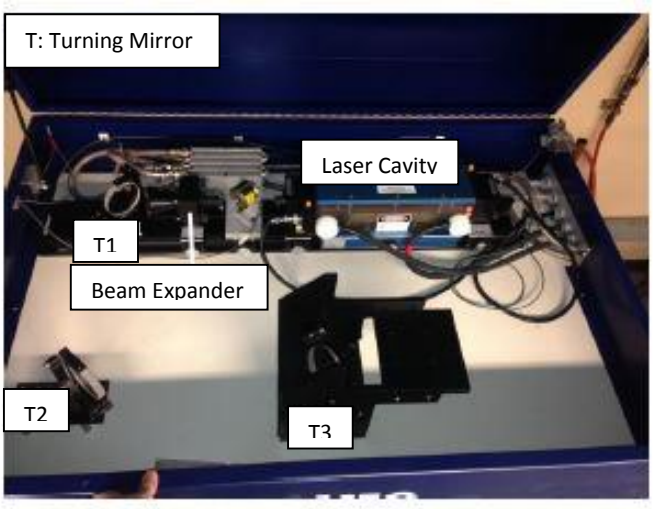

Fig 3.2: The laser cavity and laser delivery system on top of the glove box of the Optomec LENS™ 750 system at the University of North Texas

The maximum power of laser in Optomec LENS™ 750 is 535 W at 46 A current (1).

3.2.3 Powder Description and Powder Feeder

High purity metal powders of Ti and Cr were used to allow the free flow during processing time of the material. Ti and Cr of 99.9% purity and mesh size 150 are used for alloy preparation by the LENS^{TM} process. After preparing a mixture of Ti-10Cr and Ti-30Cr in separate containers and rolling them for homogeneous mixing of at a minimum of six hours, they are placed in the powder feeders 1 and 2, respectively, shown in Fig. 3.3. It is a necessity to determine the optimal flow rate of both the powder feeder for 0.1 inches in order to ensure proper flow and mixing of the required 5 compositional regions.

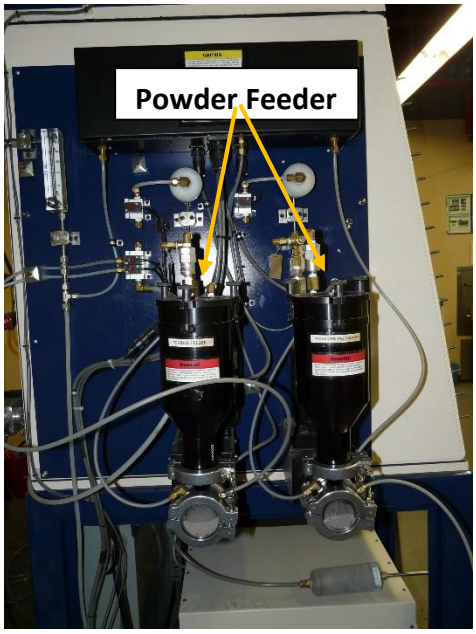

Fig. 3.3: The powder feeders installed on the LENS™ system, University of North Texas

The optimal flow is determined to be 0.5 which was determined by running a few initial depositions for a certain height of 0.1 inch and ensuring that over or under deposition does not occur with respect to the response shown by the program. The feeders that are responsible for blowing the powder for production consist of spinning wheels and cavity through which argon gas is passed to move the powder to the glove box. The spinning wheel, cavity and powder are located in the interior of the powder feeders. The voltage provided to the spinning wheel determines the amount of powder entering the glove box.

3.2.4 Programming of CAD File

A cylinder was fabricated of height 1 inch and radius 0.19 inch of Ti-xCr (10<x<30) graded specimen with 5 different compositions regions. The design file has 100 layers with each layer specified to be of 0.01 inches in size. The total number of layers divided

by the compositional increments will provide the required number of layers in each region or gradient. Since the deposition is determined to have 5 regions with 5 percent weight increase of Cr in each region, the number of layers per gradient is determined to be 20 (100/5 layers per region). A 3D CAD file consisting of the following specification of layers and dimensions is made and loaded in the computer for manufacturing the required Ti-Cr alloy specimen. Feeder 1 is loaded with homogeneously mixed Ti-10Cr powders and feeder 2 with Ti-30Cr powders. The amps required by the feeder for optimal flow is found for both the hoppers separately by initial depositions. The amps required for particular compositions are then calculated and provided to the feeders along with the region height. The summary of amps with respect to feeders flow rate, expected Cr and Ti weight percent and height are listed in table 3.2.

#	FEEDER 1 Flow rate (Ti-10Cr)	FEEDER 2 Flow rate (Ti-30Cr)	Cr (wt %)	Ti (wt %)	LAYERS	HEIGHT (INCHES)
1	0.5	0	10	90	0-20	0-0.2
2	0.375	0.125	15	85	20-40	0.2-0.4
3	0.25	0.25	20	80	40-60	0.4-0.6
4	0.125	0.375	25	75	60-80	0.6-0.8
5	0	0.5	30	70	80-100	0.8-1.0

Table 3.2: Summary of Ti-Cr alloy processing parameters.

3.2.5 Processing

Based on studies performed on the same LENS^{TM} system, Ti-Cr processing is done with a power of 460W using a Nd: YAG laser (30). When turned on, the laser is

focused on the Ti-6Al-4V substrate, shown in Fig 3.4. A melt pool is created on the substrate onto which a powder is blown in from the feeder though a nozzle. The construction of nozzle is such that the powders converge at the same point where the laser is focused onto. This ensures that the powder being deposited is nearly molten enabling a good mixing of the powders. The laser head moves with respect to the 3D CAD file provided by the computer to create thin layers of controlled thickness and width shown in Fig. 3.4. The scanning speed of the laser was set to 10 inches per minute, the design file is a cylinder with 100 layers, a total size of 1 inch and radius of 0.19 inches. Once the optimal flow rate was found for both feeders, the gradient was made from Ti-10Cr to Ti-30Cr with 5% weight increase in Cr after every 20 layers. The process was carried out in a chamber with oxygen below 5 parts per million (PPM) via manual purge.

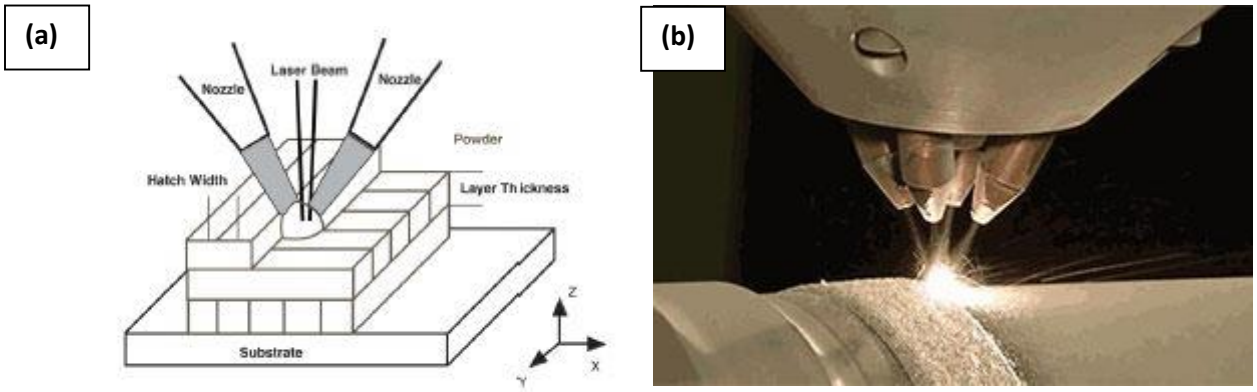

Fig 3.4: (a) Schematic representation of LENS™ process [159] and b) the image of the head and the deposited objects (image courtesy: Optomec, Inc).

3.3 Electric Discharge Machining (EDM) and Polishing

The LENS^{TM} deposited material is removed from the substrate using a Mitsubishi FX 10 wire EDM. During the process and electric field is created between the 0.15mm diameter brass wire and the specimen submerged in a dielectric field (31). The

temperature of both the specimen and wire increases leading to a small reduction in material of both wire and specimen.

The specimen is separated from substrate and is hen cut again. Since the sample being deposited is of cylindrical shape having a curved outer surface. The cylinder is cut into two halves shown in Fig. 3.5. One half is left as “as deposited” while the other half is cut again vertically into another two halves, shown in Fig. 3.5, to provide two separate samples for both heat treatments.

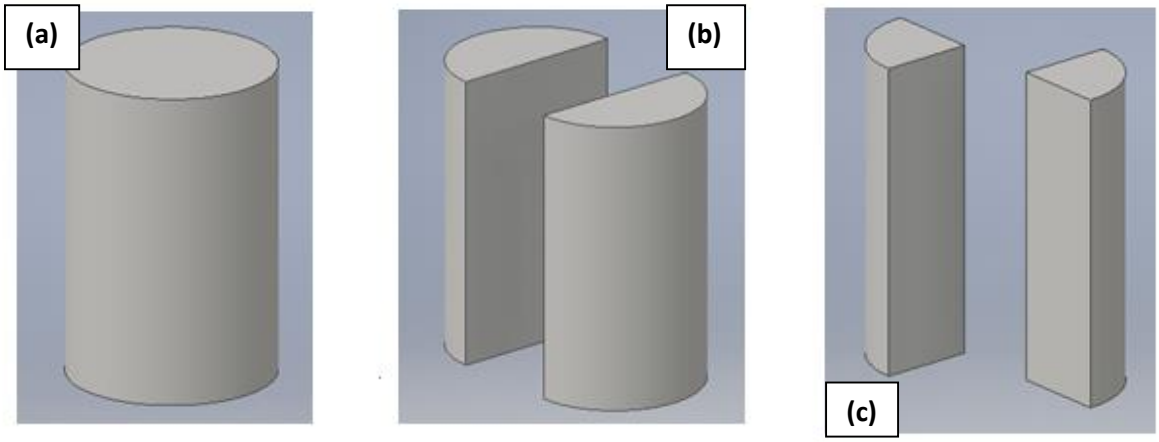

Fig 3.5: Schematic representation of (a) As deposited, (b) Vertical sectioning using EDM, (c)Vertical sectioning of the sectioned half

The total number of specimens studied for this thesis is listed in Table 3.3.

#	SPECIMEN	STATUS
1	Ti-xCr (1/2 cylinder)	As Deposited
2	Ti-xCr (1/4 cylinder)	Heat treated and furnace cooled
3	Ti-xCr (1/4 cylinder)	Heat treated and air cooled

Table 3.3: Summary of specimen and condition.

Cutting of the sample using EDM makes the sample harder to hold during polishing due to reduced surface area to hold the specimen. The samples were mounted using the mounting press manufactured by Buehler. The mounting press had one and half inch diameter stubs to heat and compress the powder from both top and bottom. This resulted in the final sample having suitable dimensions large enough be held by hand during mechanical polishing, shown in Fig. 3.6.

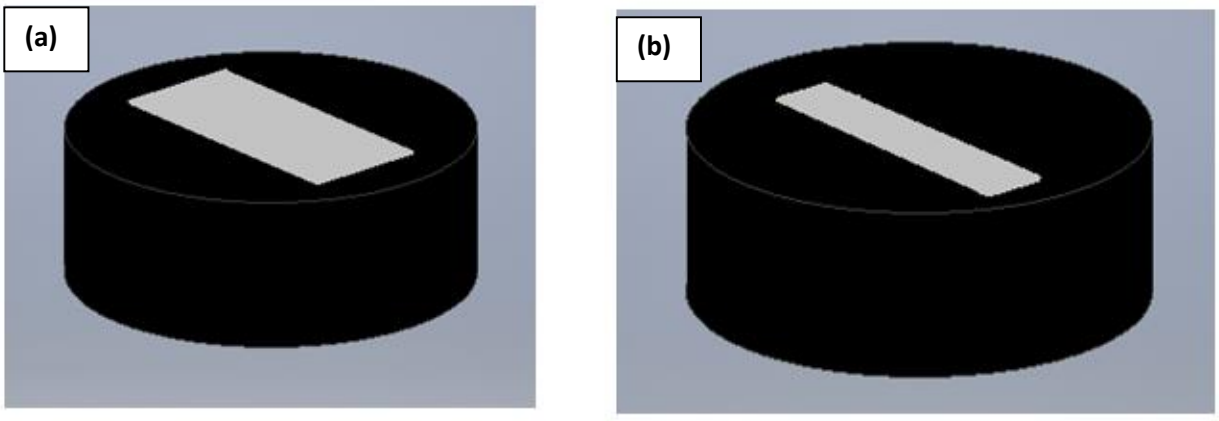

Fig 3.6: Schematic representation of (a) as deposited sample in mold and (b) sample to be heat treated in mold

Polishing is done on the material to remove scratches from the surface. For any characterization study a scratch free surface is a primary necessity. Polishing of the samples is done using a polishing machine and SiC papers of grades 120, 200, 400, 600, 800 and 1200. Polishing is performed on each of the lower grade papers for about 3-5 minutes in both horizontal and vertical directions. Care should be taken when polishing at lower grades (120-600) to prevent over polishing and slanting of sample. Polishing at finer grades (800-1200) is done for longer period of 8-10 minutes. Once the coarse and fine polishing is completed the surface will be absent of any scratches. An ultra-fine finishing is done on a silica cloth surface with the help of colloidal silica suspension of

0.04 microns. The final polishing is carried out for 30-40 minutes until a mirror polished surface is obtained. At this stage there will be no scratches on the sample surface.

After the ultra-fine polishing, the specimen is then placed in a sonicator for ultra-sonic cleaning. The specimen is first washed with a water jet of deionized water and then placed in liquid ethanol solution in the sonicator for 20-30 minutes. This is done to remove impurities left behind on surface after the polishing. The specimen is taken out, and a final wash with deionized water and ethanol jet. The surface is then dried with Nitrogen gas and is ready to be used for heating or characterization testing.

3.4 Heat Treatment

The ¼ cylinders were additionally subjected to heat treatments above the β transus temperature for the same time of 30 minutes and temperature of 1000°C. One of the heat treated samples was air cooled while the other was furnace cooled. The particular choice of cooling was selected based on the general cooling processes adopted in industries.

Heat treatment is carried out in a tube furnace with an Ar gas supply at one end shown in Fig 3.7a. The samples were wrapped in Ti foil (99.7% pure) and Ar gas is flown continuously. This circumvents oxidation of the alloy. Fig. 3.7b shows the heat treatment schedule.

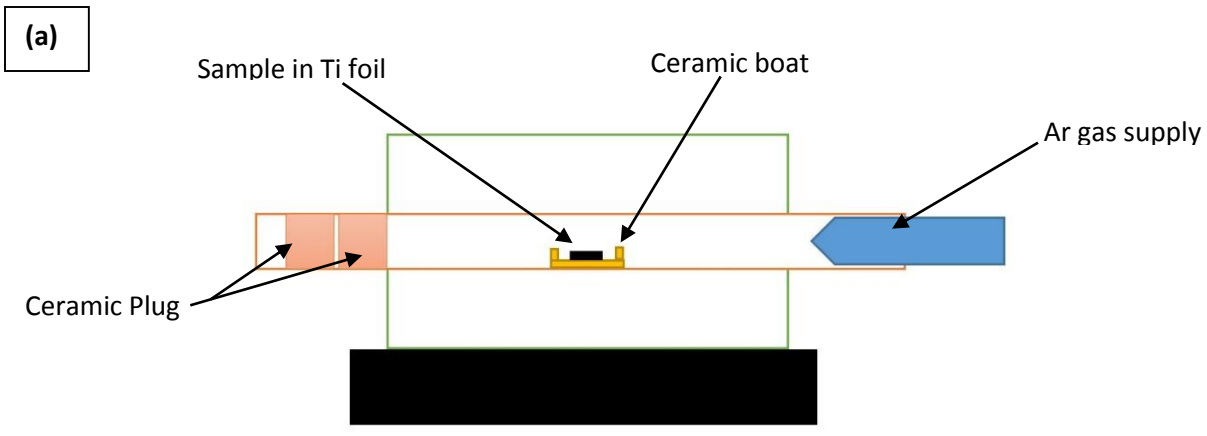

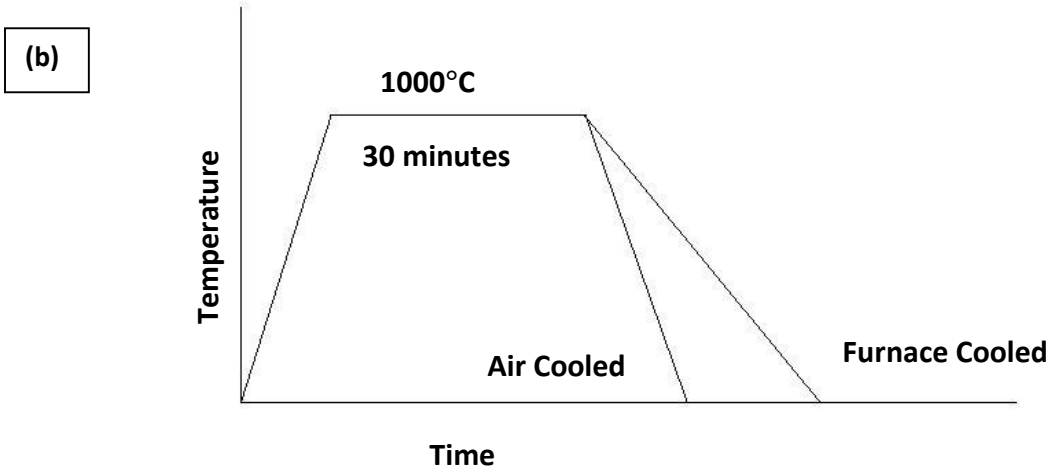

Fig 3.7: Schematic of (a) Heat Treatment Furnace and (b) heating schedule.

3.5 Vickers Micro-Hardness Testing

Vickers hardness (VH) testing (Wilsons hardness machine) was conducted on the LENS^{TM} deposited Ti-xCr graded materials to determine the hardness as a function of varying composition.. The hardness measurements are taken for the compositional gradient range of Ti-10Cr to Ti-30Cr. The testing is carried out at room temperature with a normal load of 500g with a holding time for 10 seconds at 0.5HV. The tests are conduct so as to define a linear profile from Ti-10Cr to Ti-30Cr, shown in Fig. 3.8.

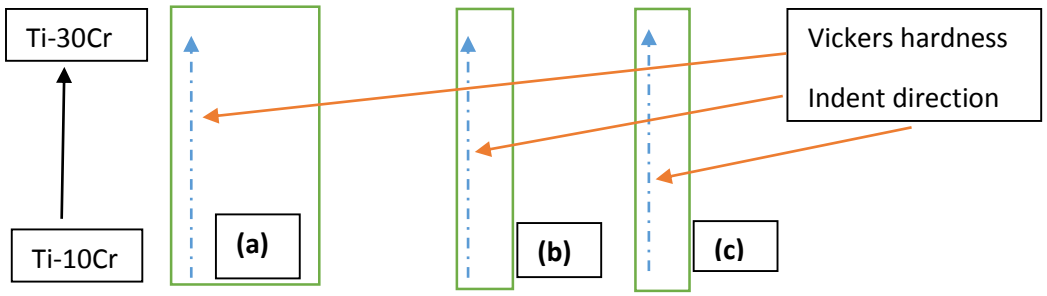

Fig 3.8: Schematic representation of Vickers hardness test direction along (a) as Deposited and (b, c) heat treated cylindrical samples.

Procuring hardness measurement as a linear profile in such a pattern enables the change in hardness along the compositional gradient and to be determined along with its relationship to the as-deposited and heat treated microstructures.

The hardness measurements are taken at 50-55 different locations along a linear profile with a distance of 500 μm between each square pyramidal indent. The Vickers hardness number (VH) can also be obtained by the expression.

$$HV = F/A \approx 1.8544 F/d^2$$

Where F is the load applied in Kgf, A is the area in mm^2 and d the average length of the diagonal left by the indenter in millimeters.

3.6 Scanning Electron Microscopy (SEM)

SEM was used in the study helps to determine the microstructure, composition of the sample using EDS at different regions in addition to acquiring EBSD maps of the LENS^{TM} deposited alloys.

An FEI nova Nano SEM 230 SEM was used that is equipped with a field emission gun (FEG) source, Everhardt Thornley detector (ETD) for detection of back scattered electrons (BSE), Secondary Electrons (SE). These tools help us with imaging and compositional quantification of the Ti-Cr graded regions viewed on the sample surface. The purpose of SEM imaging (SE and BSE) and EDS composition analysis was to capture the comparison of different regions along the gradients, determine the change in morphology and composition of each phase, and thus determine a relationship between the microstructure and hardness for as-deposited and heat treated samples.

3.7 X-Ray Diffraction (XRD)

A Rigaku Ultima III x-ray diffractometer was employed to determine crystallographic phases on five to six different regions of the as deposited sample and heat treated samples. Cu Kα incident X-rays were generated at source of 40kV and 44mA with a wavelength of 1.54Å. The XRD parameters were a sample step size of 0.01, scan speed of 1.0 per min and 2Θ values between 20° and 90°.

The data provided by XRD scans are plotted as intensity as a function of diffraction angle 2Θ. The plotted data is then analyzed with Jade v9.0 software.

3.8 Scanning Electron Microscope - Electron Back Scattered Diffraction (EBSD)

EBSD also known as Orientation Imaging Microscopy (OIM) is used for the measurement of crystallographic orientation of polycrystalline and singe crystals. One of the major advantages of using this diffraction scan is the revealing of crystallographic orientation, phases fractions, and grain orientation relationships of selected regions. EBSD was performed in the FEI nova Nano SEM 230 by using an EBSD detector.

For EBSD acquisition, the sample is tilted 70° from its initial horizontal position to prevent excess scattering and reduce the travel distance of the electrons to the detector, shown in Fig. 3.9. Each point of the diffraction pattern is collected and the orientation of the collected bands are determined by the geometry of the bands. These bands that are observed are known as Kikuchi bands. Points are stored in TSL OIM software that provides the necessary tools to analyze the data. EBSD scanning relies on the selection of phases provided from an intensive list from a comprehensive database. During the scan of individual points the software tries to determine the relative phase corresponding to the Kikuchi bands of the diffraction pattern. These candidate or relative phases are

already present in the software or could be made with the help of crystallographic information of the predicted phase. A grain boundary with misorientaion less than 15° is a low angle grain boundary while greater than 15° is considered to be a high angle grain boundary. The tolerance angle to measure the misoriented grain boundary is usually set as a high angle grain boundary misorientation to prevent false boundaries and misorientations.

The other advantages of EBSD include analyzing different crystal structures that possess the same chemical composition for bulk samples, lesser sample preparation time in comparison to TEM, and a wider area can be analyzed by this method. A limitation of EBSD is to index two constituent phases having similar crystal structures, however it can be overcome by combining it with EDS. The other limitations are inability to scan samples with excessive plastic strain and only crystalline samples can be scanned.

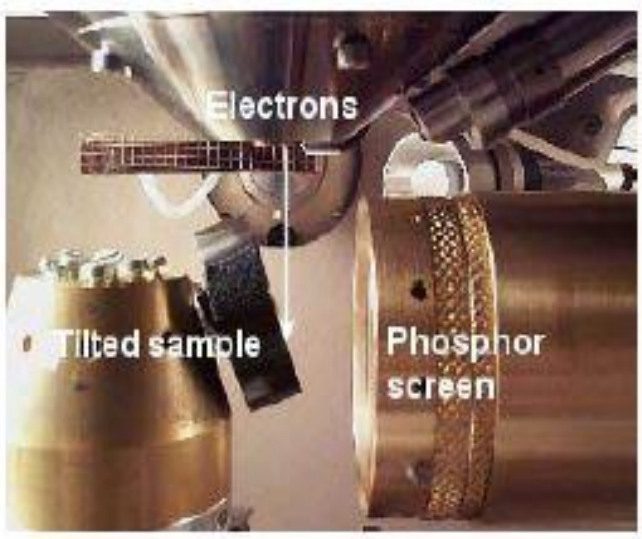

Fig 3.9: SEM-EBSD Experimental Set Up (Courtesy: Oxford Instruments)

The steps involved for carrying out the EBSD region scans are as follows.

a) The region of interest on the sample is determined. The size of the scan is selected solely on the basis of the sample feature size. For small features, the area analyzed was smaller than compared to regions where only single phases exist.
b) An EDS scan is conducted before the tilting to determine the composition of the region in focus.
c) The peaks from EDS are identified and assigned by the software.
d) After the EDS is completed, the sample is tilted 70 degrees from the horizontal to reduce scattering of electrons to the detector.
e) A fast scan is performed at a low magnification to acquire a background pattern of differently oriented grains.
f) In spot mode, beam position is fixed on a grain. This will create a “RAW” pattern with a weak contrast.
g) The contrast is increased greatly by dividing, removal or other manipulation of the background.
h) On the scanned surface, Kikuchi Bands of the region are observed.
i) The Houghs transform of the corresponding pattern is calculated with the help of the Kikuchi bands. The height and width of the peak is relative to the intensity and width of the band.
j) The information of the phases to be indexed is loaded from the database.
k) The distances between the poles are fixed and calibrated with respect to the screen position and working distance.
l) Indexing is done as a final step before the analysis begins.

m) Once the scan is completed, the file is opened in TSL, and the required information of the crystal structure, misorientation angle, phase fraction, pole figure (PF), and inverse pole figure (IPF) are obtained.

3.9 Dual Beam Focused Ion Beam SEM (FIB/SEM)

FIB cross-sectioning in the SEM is a method used to image the subsurface of the materials microstructure. The following are the steps when making a FIB lift out.

1. Deposition of Pt layer on top of the region to be analyzed. The Pt layer acts as a protective coating and mitigates the effects of ion beam milling/damage into the volume of the sample to be analyzed.
2. Milling trenches of rectangular shapes to required depth across the volume required to be analyzed.
3. Undercut milling patterns are provided to ensure that the resultant block to be analyzed is supported by two beams connected to the bulk of the sample.
4. Using the Omniprobe needle to remove the volume of interest from the bulk of the sample and mount it on separate Cu post via Pt deposition or weld.
5. Initial, Middle and Final polishing of the volume to be analyzed by ion milling at various voltages and amps.

Once final polishing is completed, the volume to be analyzed is electron transparent. Electron transparency of the material is the most important criteria of the sample to be viewed for subsequent TEM analysis.

3.10 Transmission Electron Microscopy (TEM)

Characterization of material microstructure at high spatial resolution is carried out by the use of FEI Tecnai F20 field emission gun (FEG) TEM. The operating voltage is 200keV. High energy electrons of small wavelengths approximated to 0.025Å is passed through a thin electron transparent sample so as to analyze and image the microstructure of the sample at a high spatial resolution of around 50-100 nanometer scale length. Using small wavelengths of energy for electrons enables the determination of material defects and interfaces present in the material.

CHAPTER 4

INFLUENCE OF Cr CONCENTRATION ON MICROSTRUCTURAL PHASE EVOLUTION AND ITS EFFECT ON HARDNESS IN AS DEPOSITED Ti-xCr ALLOYS

4.1 Introduction

The effect of compositional variation of Cr concentration on as deposited Ti-xCr (Ti-xCr: 10≤x≤30wt %) LENS^{TM} processed sample is assessed, by means of XRD, SEM imaging, EBSD scans and micro-hardness measurements. The data obtained from the experiments is studied and correlated to provide a sufficient conclusion on the microstructure and mechanical property change of the compositionally graded as deposited alloy.

4.2 Microstructural Evolution Studied by SEM

The microstructural and compositional evolution of as deposited Ti-10Cr to Ti-30Cr graded alloy were studied by BSE imaging and EDS, respectively. Fig. 4.1 shows a schematic of the analysis regions along which BSE imaging and EDS scans were conducted on the graded alloy. Secondary electron imaging did not provide much useful information, hence BSE imaging was chosen as the characterization technique. Fig 4.2 (a)-(g) and Fig. 4.3 (a)-(e) show representative BSE image comparisons for low and high wt% Cr contents, respectively, along the length of the different regions of the alloy. Fig. 4.4 (a)-(l) summarizes the entire compositional range at a higher BSE image magnification. The expected product phases of the microstructure based on Ti-Cr phase diagram in Fig. 2.2 and a similar LENS^{TM} processed alloy are α-Ti, β-Ti, and $TiCr_2$ (11,

41). The images in Figs. 4.2-4.4 have the corresponding Cr wt% values that were determined by EDS acquired along each region multiple times. The compositional changes along the length of the sample are summarized in table 4.1. The height occupied by each region is approximated to be 1.25mm. While there is a trend of increasing Cr content along the length of the alloy, there is some statistical variation in sub-regions. Thus, it is not a uniformly compositionally graded alloy due to the variation in heat transfer during LENS^{TM} processing.

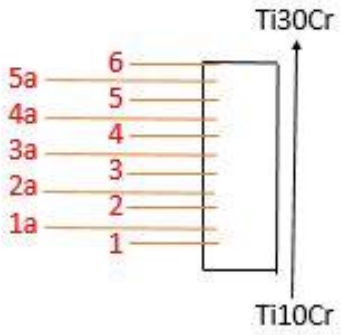

Fig 4.1: Schematic representation of Regions and Sub-regions for acquiring BSE images and EDS scans.

From Fig 4.2 (a)-(g), it is evident that the β phase is the matrix, and the α phase precipitate is a product of the eutectoid reaction at Ti~13 wt% Cr.

$$\beta \rightarrow \alpha + TiCr_2$$

The presence of α phase in hypo-eutectoid regions from Region 1 (Ti-7.7Cr) to Region 4a (Ti-13.5Cr) is observed. However the distribution is inconsistent and not homogeneous.

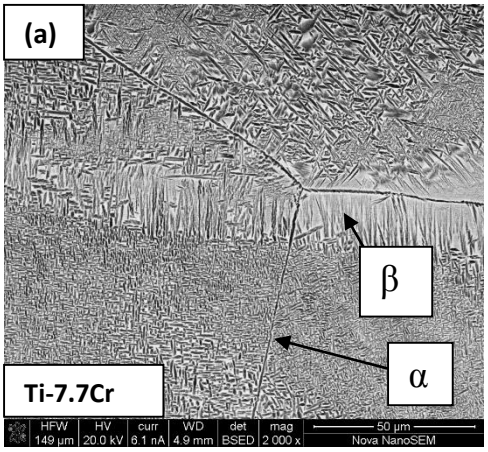
(a)
β
α
Ti-7.7Cr
HFW 149 µm | HV 20.0 kV | curr 6.1 nA | WD 4.9 mm | det BSED | mag 2 000 x | 50 µm | Nova NanoSEM

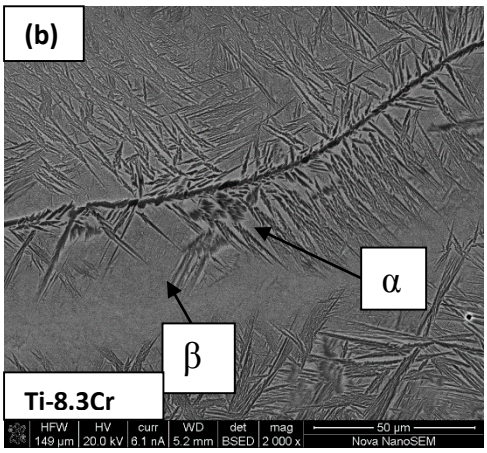
(b)
α
β
Ti-8.3Cr
HFW 149 µm | HV 20.0 kV | curr 6.1 nA | WD 5.2 mm | det BSED | mag 2 000 x | 50 µm | Nova NanoSEM

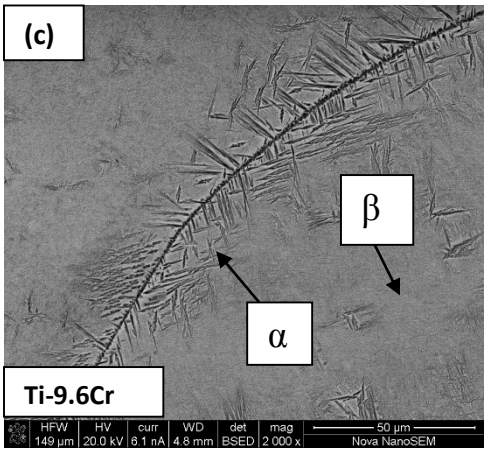
(c)
β
α
Ti-9.6Cr
HFW 149 µm | HV 20.0 kV | curr 6.1 nA | WD 4.8 mm | det BSED | mag 2 000 x | 50 µm | Nova NanoSEM

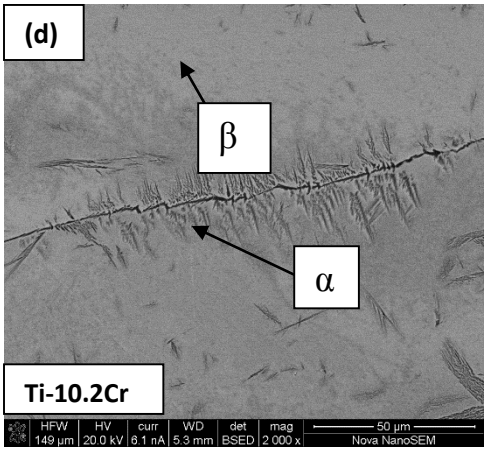
(d)
β
α
Ti-10.2Cr
HFW 149 µm | HV 20.0 kV | curr 6.1 nA | WD 5.3 mm | det BSED | mag 2 000 x | 50 µm | Nova NanoSEM

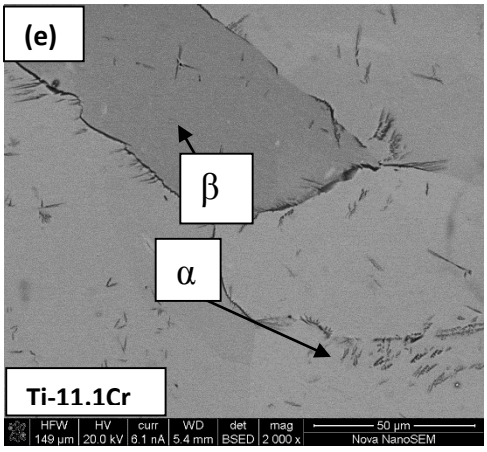
(e)
β
α
Ti-11.1Cr
HFW 149 µm | HV 20.0 kV | curr 6.1 nA | WD 5.4 mm | det BSED | mag 2 000 x | 50 µm | Nova NanoSEM

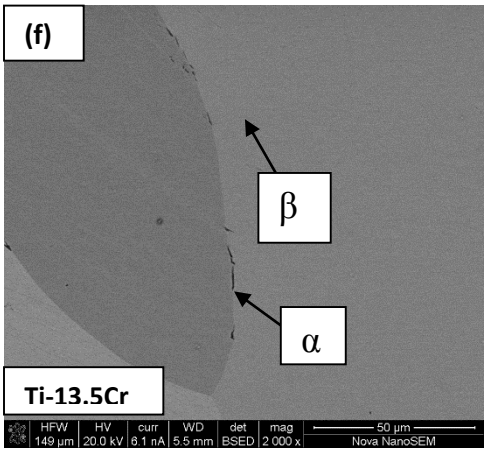
(f)
β
α
Ti-13.5Cr
HFW 149 µm | HV 20.0 kV | curr 6.1 nA | WD 5.5 mm | det BSED | mag 2 000 x | 50 µm | Nova NanoSEM

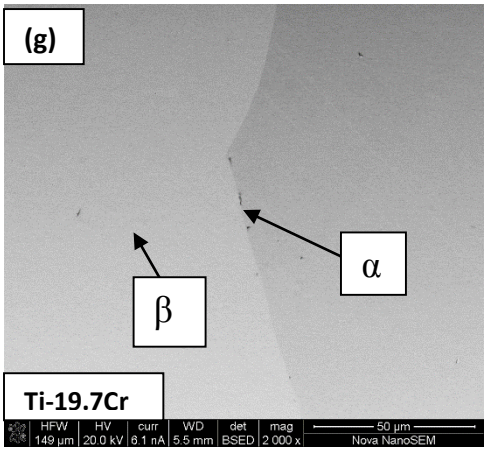

Fig 4.2: (a)-(g) BSE images showing microstructural changes for low Cr (7-20) wt% alloys.

REGION	COMPOSISTION (wt%)	REGION	COMPOSISTION (wt%)	REGION	COMPOSISTION (wt%)
1	Ti-7.7Cr	3	Ti-9.9Cr	5	Ti-31.2Cr
1a	Ti-9.6Cr	3a	Ti-10.2Cr	5a	Ti-25.5 Cr
2	Ti-8.3Cr	4	Ti-11.0Cr	6	Ti-20.8Cr
					Ti-29.6Cr
2a	Ti-8.3Cr	4a	Ti-11.1Cr,		
			Ti-13.5Cr		
			Ti-19.7Cr		
			Ti-20.5Cr		
			Ti-23.5Cr		

Table 4.1: EDS determined compositions of the various regions and sub-regions.

Absence of heat treatment coupled with irregular reheating at particular regions during processing via LENS^{TM} is responsible for the inconsistency in the α phase distribution. The α phase reduces with increasing Cr content along the length of the

sample. Chromium, being a β stabilizing element in the alloy system, suppresses the formation of the α phase. The α phase becomes negligible above 13 wt% Cr.

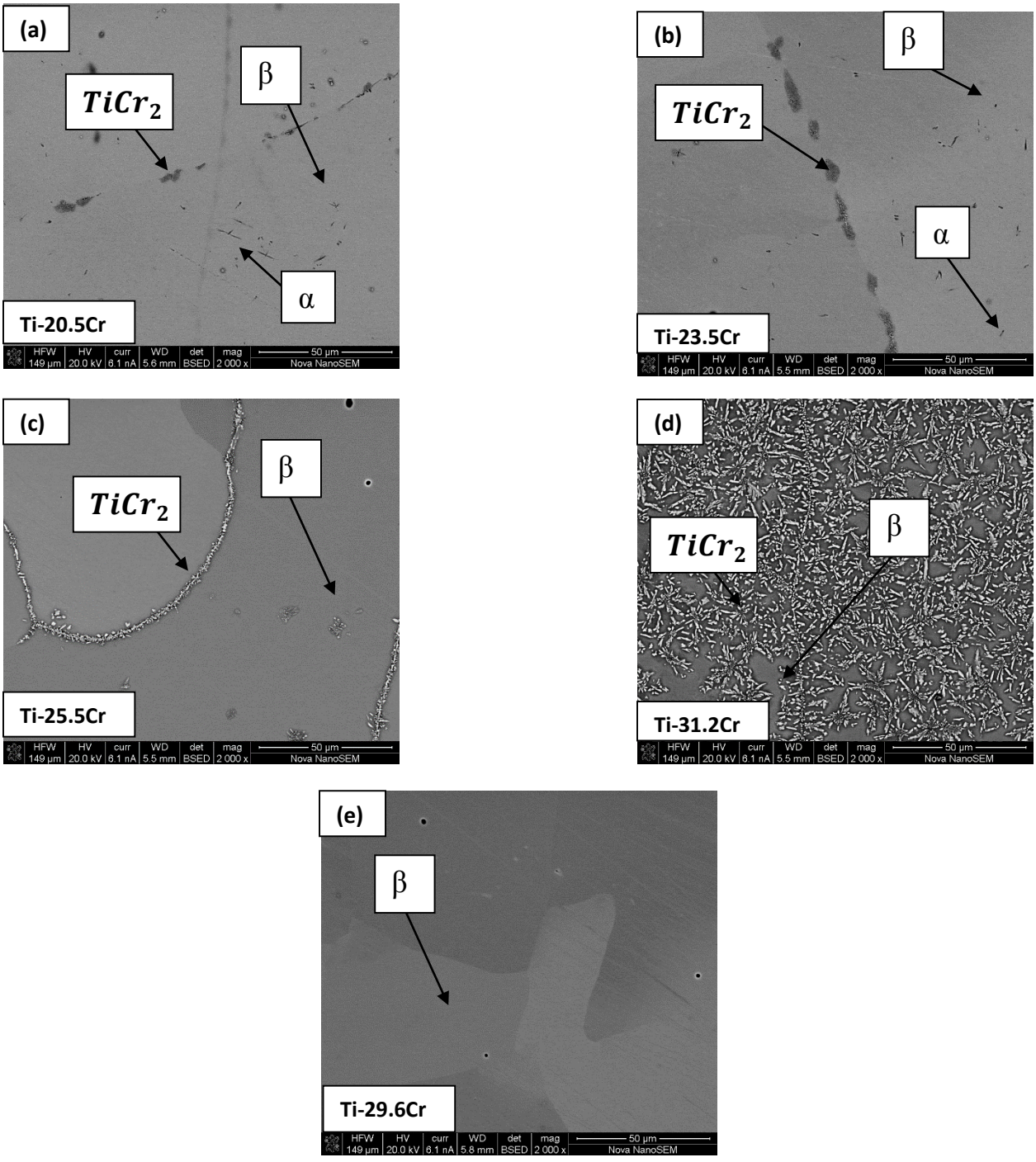

Fig 4.3: (a)-(e) BSE images showing microstructural changes at high Cr (20-30) wt%.

The initial formation of intermetallic $TiCr_2$ (Laves phase C15) occurs at grain boundaries within the β matrix at hyper eutectoid regions such as Ti-20.5Cr, as seen in Fig 4.3(a). $TiCr_2$ content continues to increases with increasing Cr content. In region 6 (Ti-29.6Cr), although similar in composition to Region 5 (Ti-31.2Cr), there is limited to no presence of the $TiCr_2$ phase. It is either present on a few boundaries or entirely absent. The intermetallic phase formation being a sluggish process is responsible for this condition in Region 6. However, selective undercooling in Region 5 during LENS™ operation is the cause for large scale deposition of the $TiCr_2$ phase.

When Region 6 is deposited, the upper most layer, the heat generated from the laser is transferred inwards providing a higher temperature for the lower regions. This keeps the lower regions at elevated temperatures for a longer period of time (reheating effect), and hence facilitates the decomposition of the β phase to $TiCr_2$ in Region 5 and regions below.

A summary of SEM BSE images taken at higher magnification for the entire compositional range along the different regions is shown in Fig 4.4 (a)-(l).

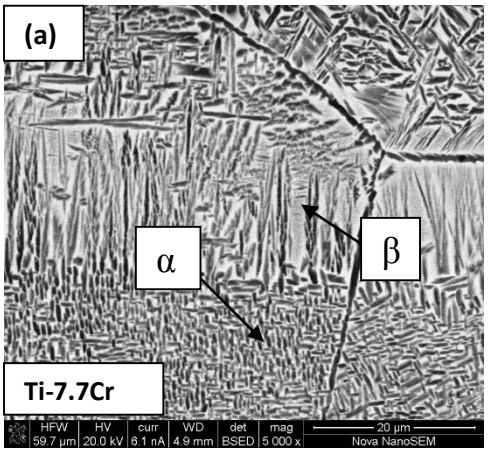

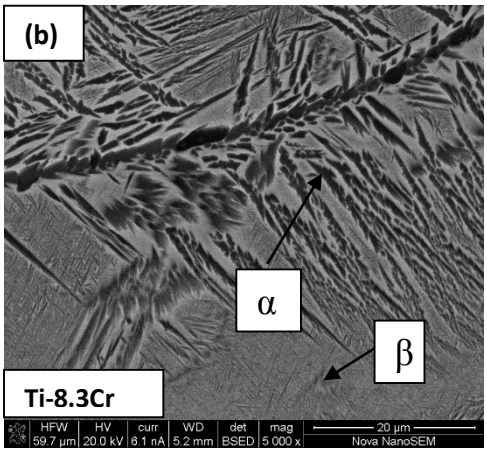

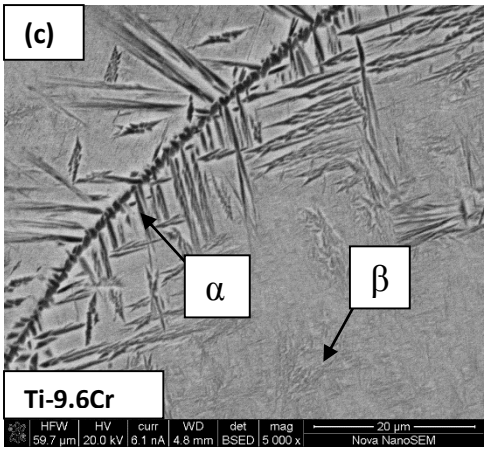
(c)
α
β
Ti-9.6Cr
HFW 59.7 µm | HV 20.0 kV | curr 6.1 nA | WD 4.8 mm | det BSED | mag 5 000 x | 20 µm | Nova NanoSEM

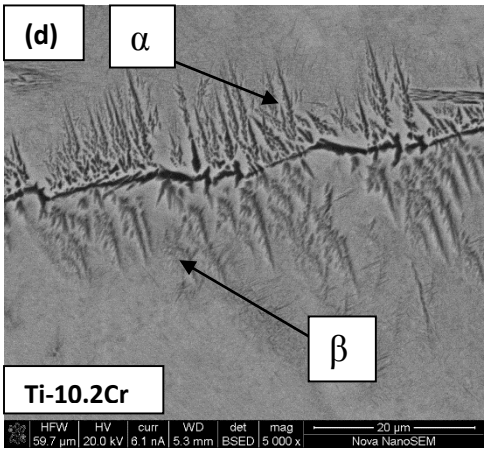
(d)
α
β
Ti-10.2Cr
HFW 59.7 µm | HV 20.0 kV | curr 6.1 nA | WD 5.3 mm | det BSED | mag 5 000 x | 20 µm | Nova NanoSEM

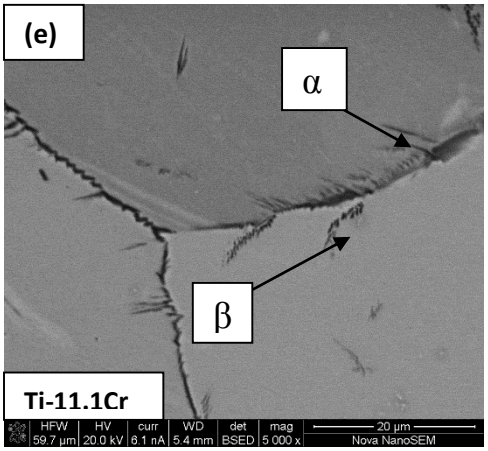
(e)
α
β
Ti-11.1Cr
HFW 59.7 µm | HV 20.0 kV | curr 6.1 nA | WD 5.4 mm | det BSED | mag 5 000 x | 20 µm | Nova NanoSEM

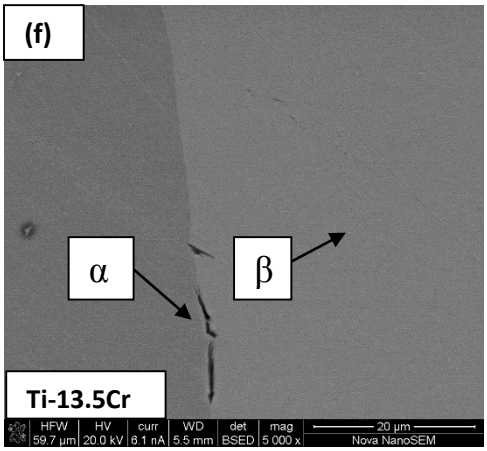
(f)
α
β
Ti-13.5Cr
HFW 59.7 µm | HV 20.0 kV | curr 6.1 nA | WD 5.5 mm | det BSED | mag 5 000 x | 20 µm | Nova NanoSEM

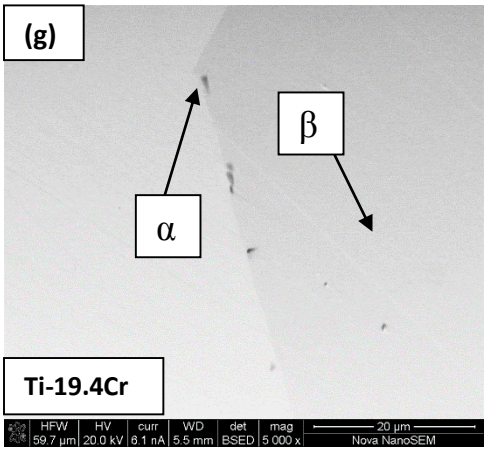
(g)
α
β
Ti-19.4Cr
HFW 59.7 µm | HV 20.0 kV | curr 6.1 nA | WD 5.5 mm | det BSED | mag 5 000 x | 20 µm | Nova NanoSEM

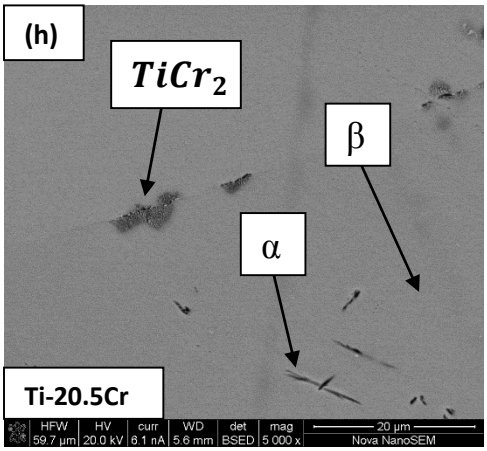
(h)
$TiCr_2$
β
α
Ti-20.5Cr
HFW 59.7 µm | HV 20.0 kV | curr 6.1 nA | WD 5.6 mm | det BSED | mag 5 000 x | 20 µm | Nova NanoSEM

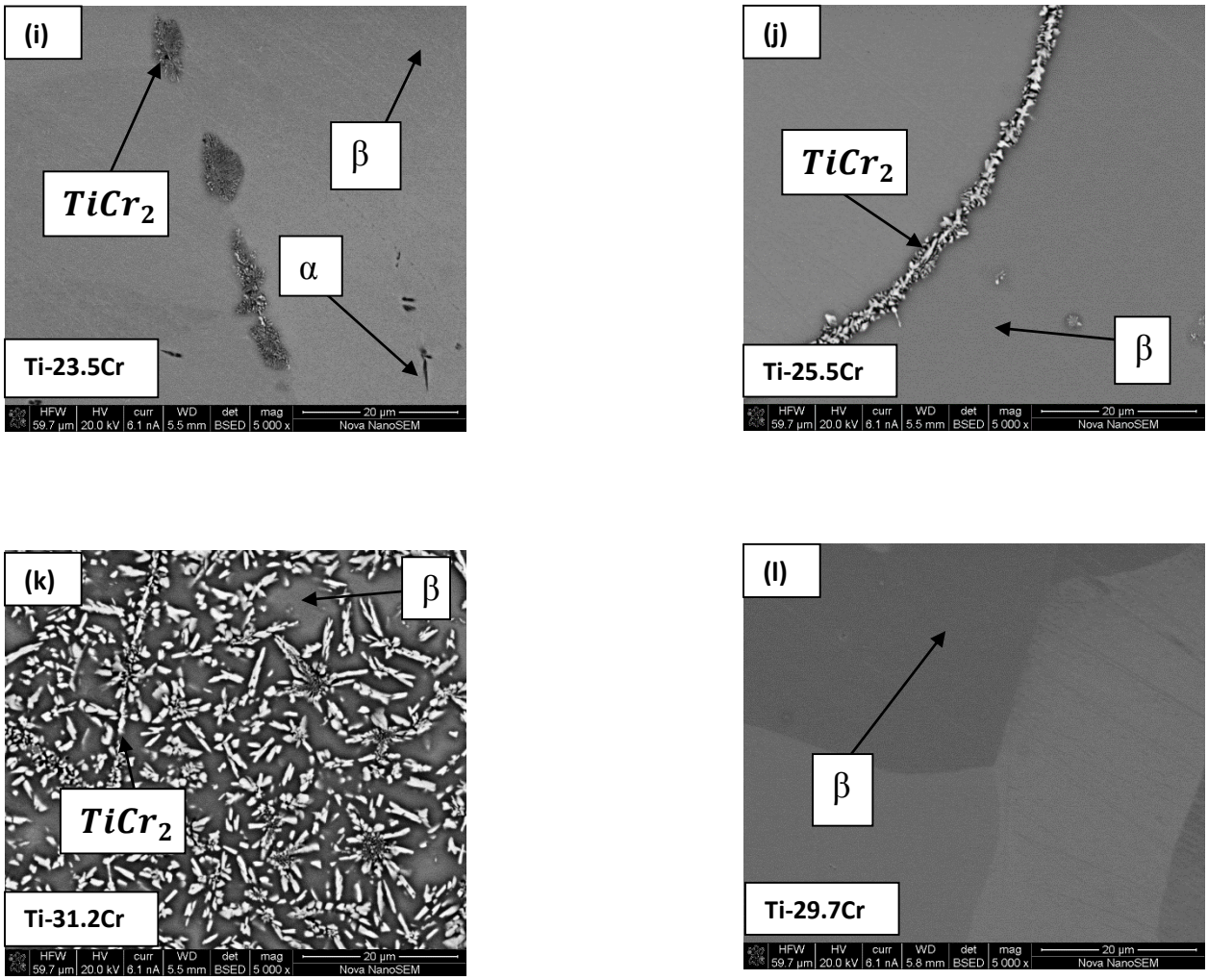

Fig 4.4: (a)-(l) Summary of higher magnification BSE images along entire Cr compositional range.

4.3 X-Ray Diffraction (XRD)

XRD of the graded alloy was conducted along 7 different regions shown schematically in Fig. 4.5. The regions were selected on basis of their compositional gradient and change in microstructure. A slit size of H2 was done for 6 scans to provide a more concise scan than a broad one at a particular region.

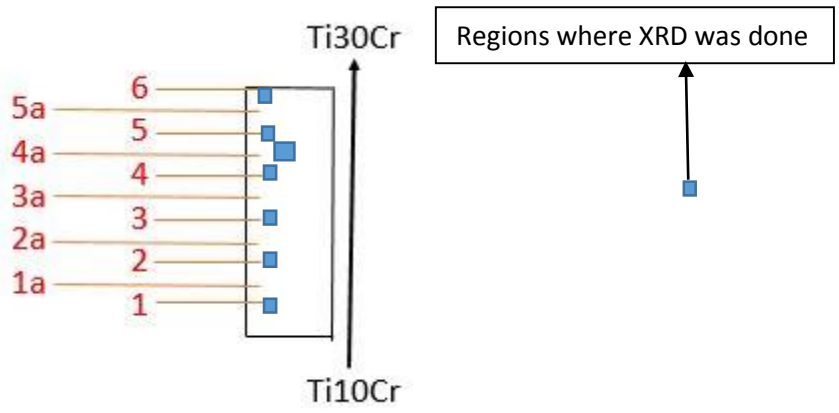

Fig 4.5: Schematic Representation of the Regions and Sub-regions for acquiring XRD scans.

The various XRD scans obtained for different regions with respect to increasing Cr content are shown in Fig 4.6 (a)-(d) and Fig 4.7 (a)-(c) for low and higher wt% Cr contents, respectively. In Fig 4.6 (a)-(d), the XRD scans of Region 1 Ti-(7.7-8.3)Cr, Region 2 Ti-(8.3-9.9)Cr, Region 3 Ti-(9.9-11.0)Cr, and Region 4 Ti-(11.0-13.5)Cr, being hypo-eutectoid regions show the presence of the primary indexed phases of α-Ti (HCP) and β-Ti (BCC).

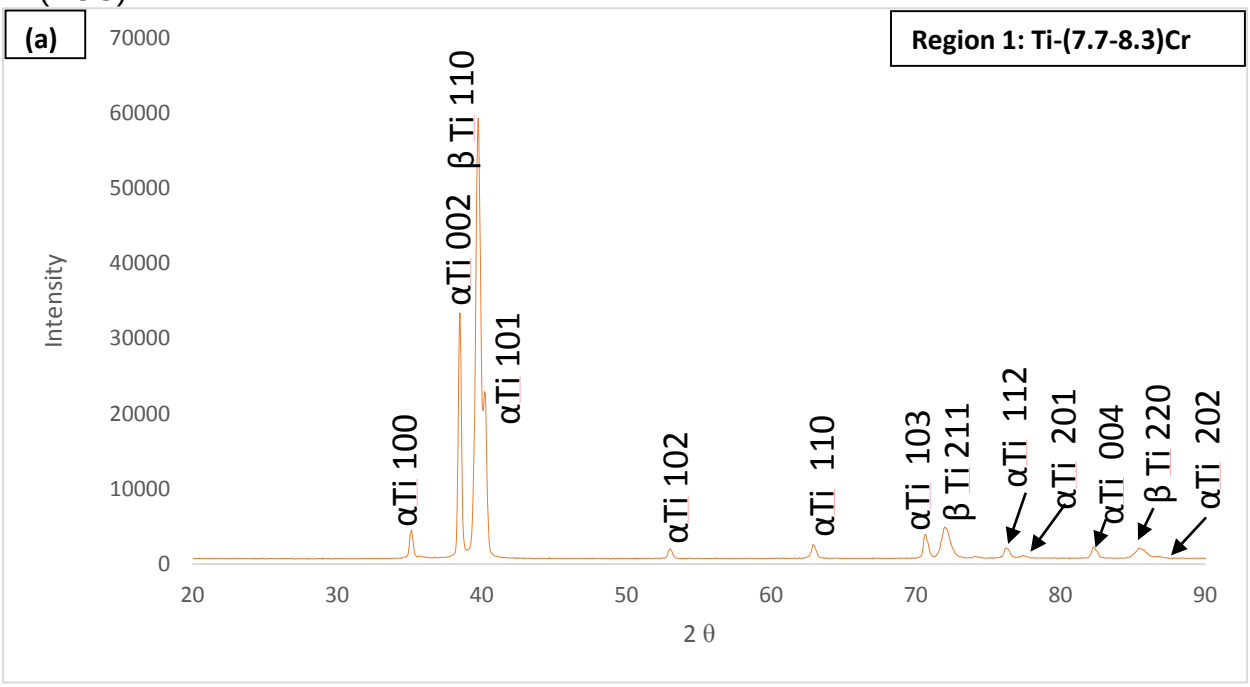

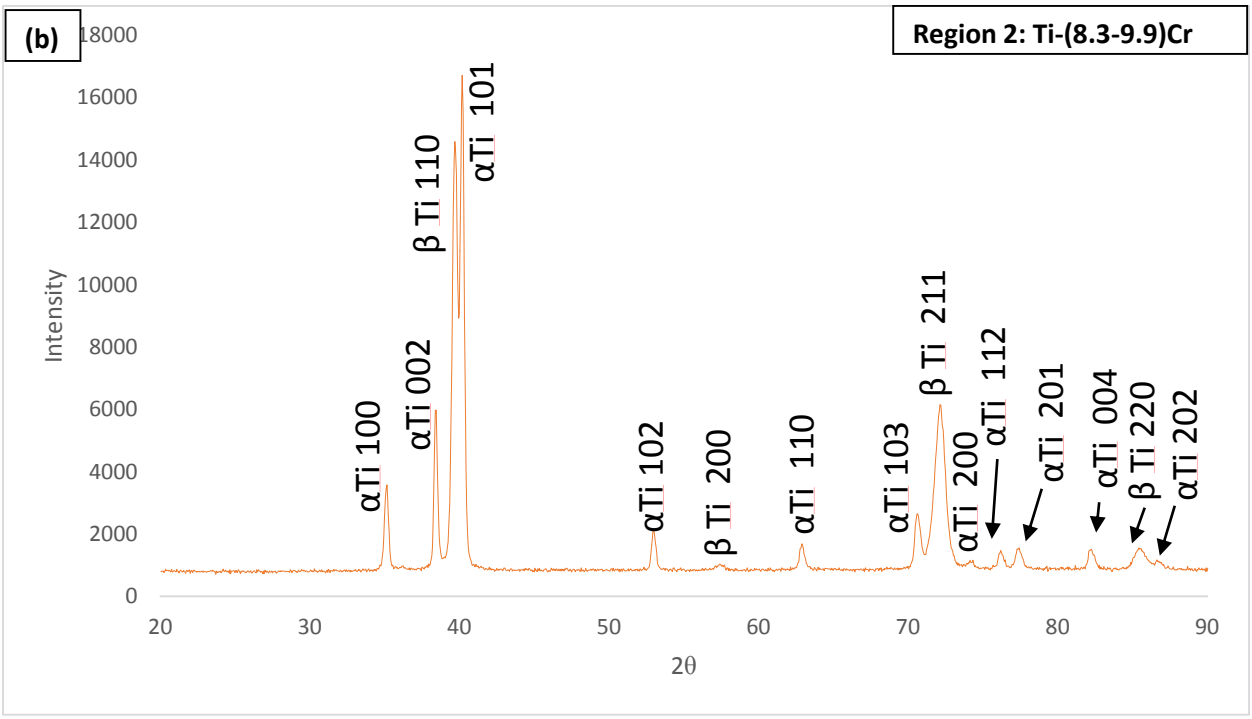
(b)
Region 2: Ti-(8.3-9.9)Cr
Intensity
2θ
αTi 100
αTi 002
β Ti 110
αTi 101
αTi 102
β Ti 200
αTi 110
αTi 103
β Ti 211
αTi 200
αTi 112
αTi 201
αTi 004
β Ti 220
αTi 202

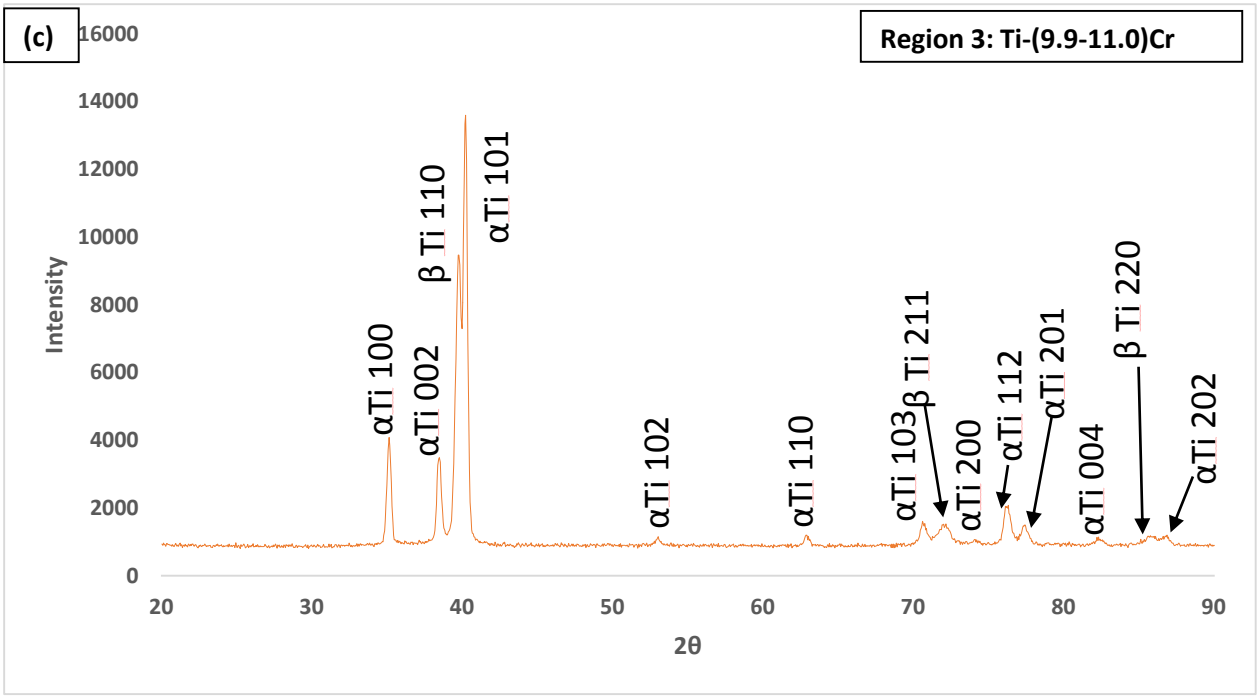
(c)
Region 3: Ti-(9.9-11.0)Cr
Intensity
2θ
αTi 100
αTi 002
β Ti 110
αTi 101
αTi 102
αTi 110
αTi 103
β Ti 211
αTi 200
αTi 112
αTi 201
αTi 004
β Ti 220
αTi 202

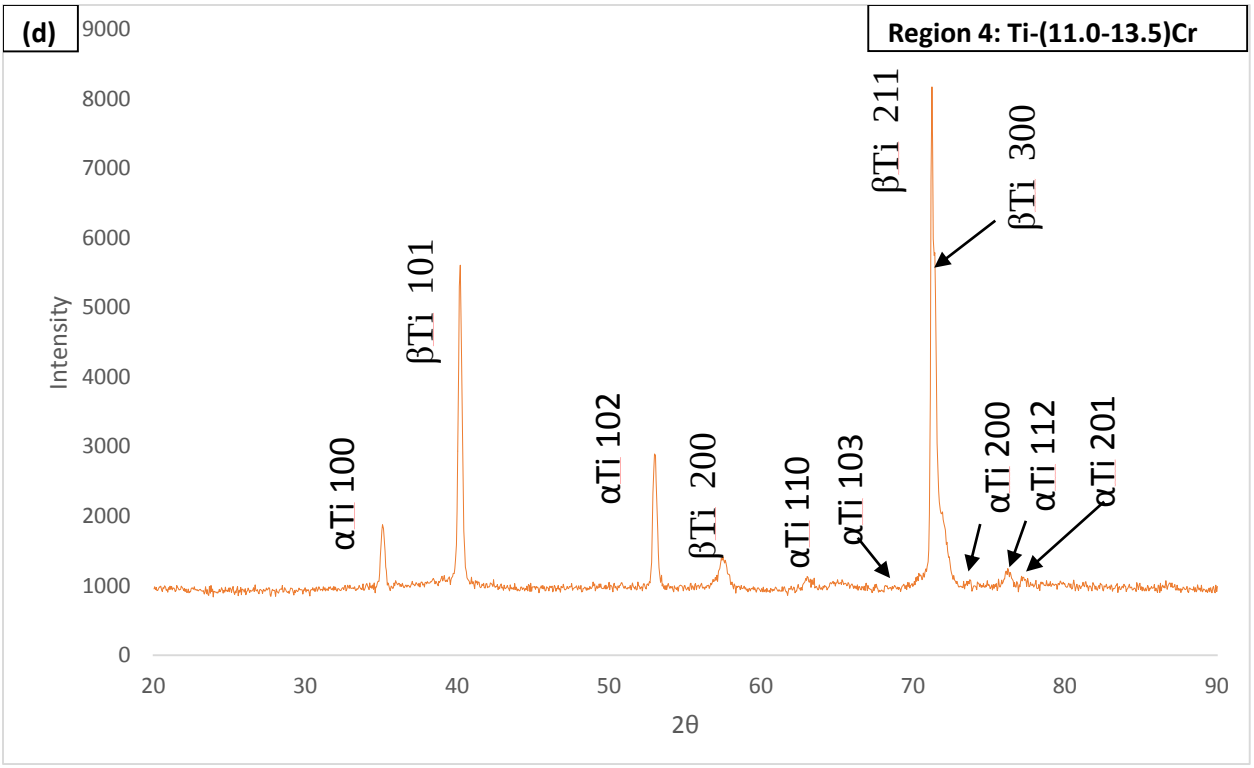

Fig 4.6: XRD scans of low Cr wt% Regions (a) Ti-(7.7-8.3)Cr, (b) Ti-(8.3-9.9)Cr, (c) Ti-(9.9-11.0)Cr, (d) Ti-(11.0-13.5)Cr.

Since chromium is a β stabilizer, there is an increase of β-Ti with increasing Cr wt% along the length of the graded alloy. Rhis leads to an increase in the intensity and number of β peaks indexed while there is a reduction in th indexed α peaks. In addition, there are β peak shifts likely due to the β stabilizing Cr alloying element, texturing between the multiple phases, and reheating effects from LENS^{TM} deposition. Stresses induced during EDM may also play a factor for the peak shift. Peak shifts were also observed in Ti-Cr alloy study by Hsueh-Chuan Hsu et al (26).

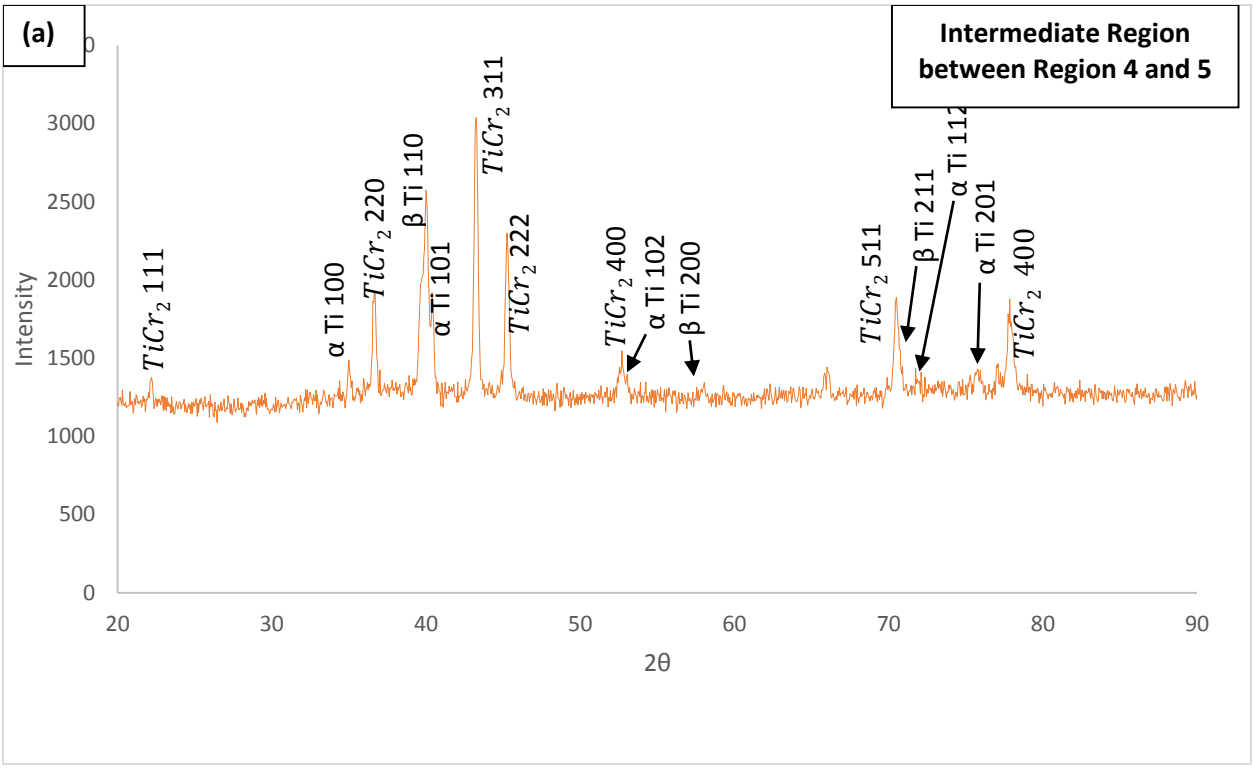
(a)
Intermediate Region between Region 4 and 5
Intensity
2θ
$TiCr_2$ 111
α Ti 100
$TiCr_2$ 220
β Ti 110
α Ti 101
$TiCr_2$ 311
$TiCr_2$ 222
$TiCr_2$ 400
α Ti 102
β Ti 200
$TiCr_2$ 511
β Ti 211
α Ti 201
$TiCr_2$ 400

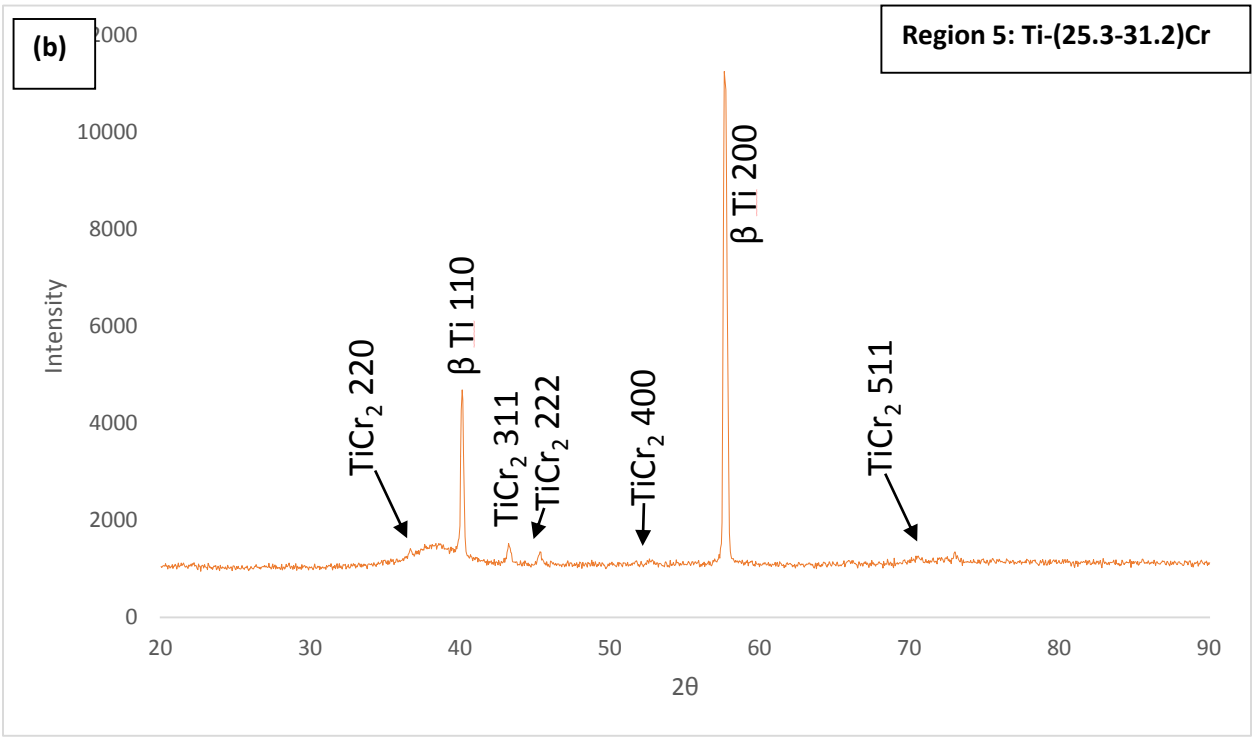
(b)
Region 5: Ti-(25.3-31.2)Cr
Intensity
2θ
$TiCr_2$ 220
β Ti 110
$TiCr_2$ 311
$TiCr_2$ 222
$TiCr_2$ 400
β Ti 200
$TiCr_2$ 511

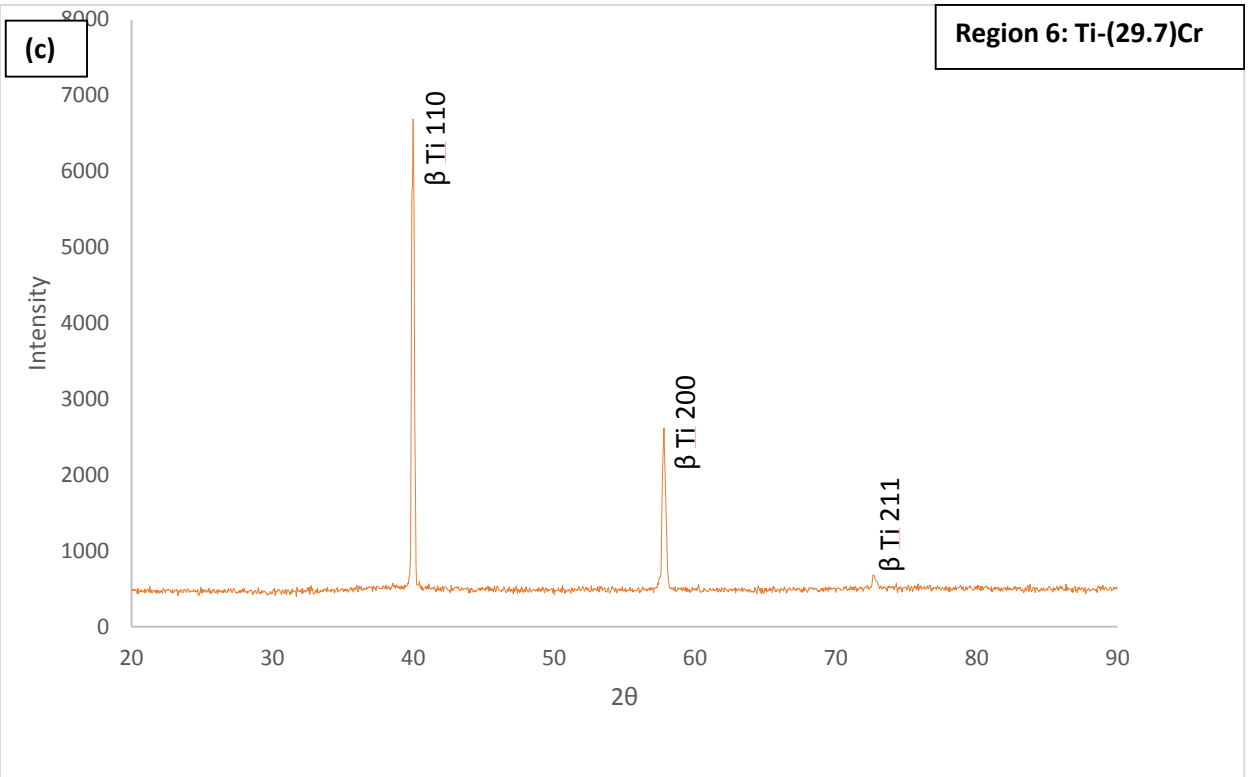

Fig 4.7: XRD scans of Higher Cr wt% Regions (a) Intermediate region between Ti-(11.0-13.5)Cr and Ti-(25.5-31.2)Cr, (b) Ti-(25.5-31.2)Cr, (c) Ti-(29.7)Cr

Fig 4.7 shows XRD scans on hyper eutectoid regions where higher Cr wt% regions are present. Fig. 4.7 (a) and (b) show the presence of $TiCr_2$ phase and β phase at the intermediate region between regions 4 and 5 and Region 5, respectively. The $TiCr_2$ phase was indexed to C15 Laves phase (space group Fd-3m). The XRD scans shown in Fig. 4.7 (b) and (c) are of particular interest since both regions have similar compositions but different crystal structures. Region 6 (upper layer) exhibits only the β phase while Region 5 (lower layer) shows the β and $TiCr_2$ phases. This corroborates the BSE images shown earlier where the reheating effects of lower layers of the sample for longer period of time during LENS™ deposition facilitates the nucleation of $TiCr_2$ intermetallic phase at lower regions than at the top of the sample.

The XRD scan in Fig 4.7 (a) showing presence of α phase along with $TiCr_2$ and β phases is also verified by previously shown SEM BSE imaging.

Fig 4.8 XRD scans summarize the phase changes of along the length of the graded sample. The lattice parameters of β and $TiCr_2$ phases versus the lattice parameters calculated theoretically at different regions are listed in table 4.1.

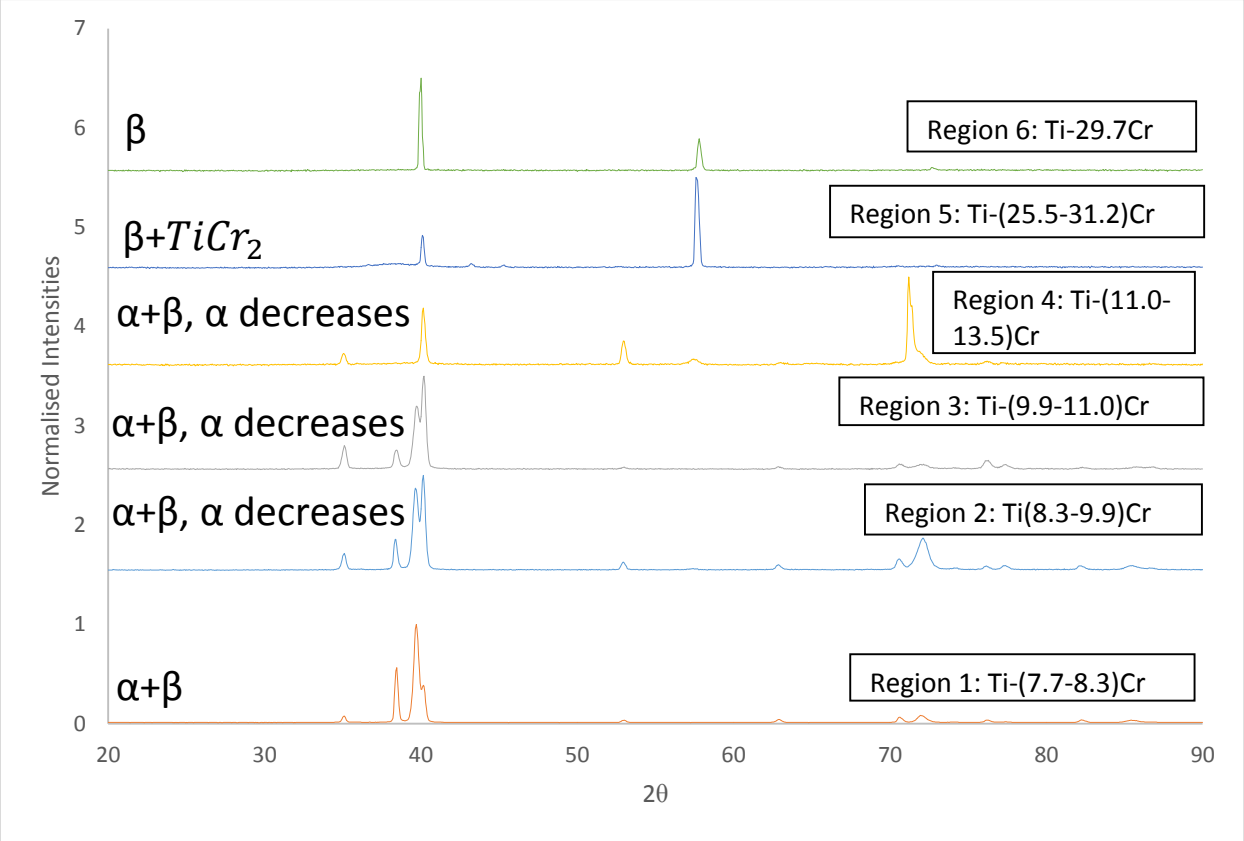

Fig 4.8: XRD scan summary along the regions of the graded alloy.

In summary, from Region 1: Ti-(7.7-8.3)Cr to Region 4: Ti-(11.0-13.5)Cr there is an increase in the β phase with respect to α phase. Region 5: Ti-(25.5-31.2)Cr shows the presence of $TiCr_2$ and β phase while in Region 6: Ti-29.7Cr, there is only the β phase. An intermediate region between regions 4 and 5 shows α, β and $TiCr_2$ phases. These indexed phases agree with those observed in the SEM BSE images

Region	Composition	Calculated lattice constant (a) in Å		PDF lattice constant (a) in Å (Vegards law)	
		β phase	$TiCr_2$ phase	β phase	$TiCr_2$ phase
1	Ti-(7.7-8.3)Cr	3.21	-	3.20	-
2	Ti-(8.3-9.9)Cr	3.21	-	3.20	-
3	Ti-(9.9-11.0)Cr	3.20	-	3.19	-
4	Ti-(11.0-13.5)Cr	3.23	-	3.22	-
5	Ti-(25.5-31.2)Cr	3.18	6.97	3.18	6.94
6	Ti-29.7Cr	3.20	-	3.18	-

Table 4.2: Lattice Parameters of β and $TiCr_2$ Phases along the graded regions.

4.4 Electron Backscatter Diffraction (EBSD)

EBSD is carried out to identify phase fractions and grain crystallographic orientations of α, β and $TiCr_2$ phases along the graded alloy. These EBSD scans provided a clearer understanding of the microstructural evolution when correlated to the XRD scans and SEM images of the various regions. The crystallographic phases and orientations of the regions of the as deposited alloy scanned are Region 1: Ti-7.7Cr, Region 2: Ti-9.6Cr, Region 4: Ti-19.7Cr, Region 5: Ti-31.2Cr and Region 6: Ti-29.6Cr.

4.4.1 Region 1: Ti-7.7Cr

The EBSD scan in Region 1 was acquired at a 60x60 microns area with a conference index (CI) of 0.21.

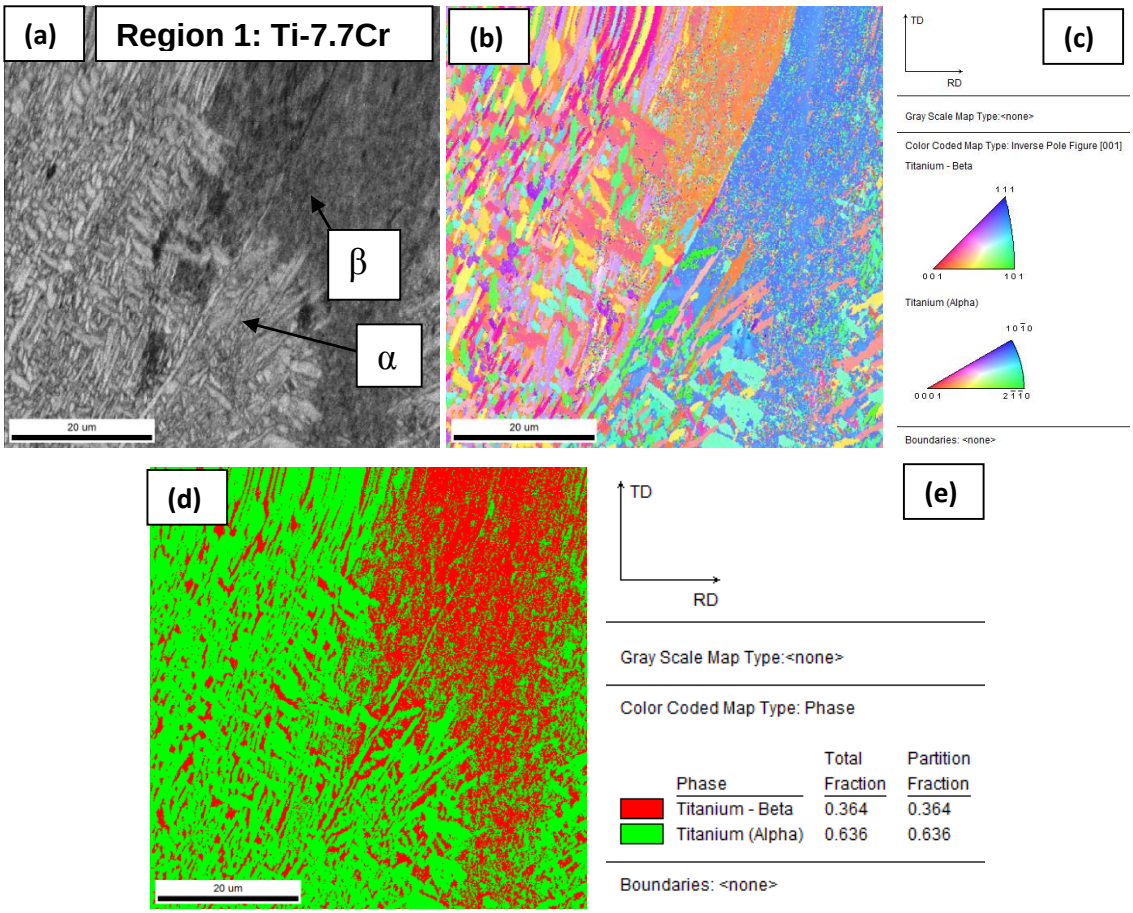

Fig 4.9: SEM-EBSD of Region 1 (a) SE image, (b) IPF, (c) ST, (d) Phase fraction map, and (e) Color code of phases in map,

Fig. 4.9 (a) shows the SEM SE image of the area scanned. Fig. 4.9 (b) provides the different crystallographic orientation of the phases in different colors, known as an inverse pole figure (IPF) map. Fig. 4.9 (c) indicates the stereographic triangle (ST) and direction of orientation for cubic β and hexagonal α, while Figs. 4.9 (d) and (e) indicate the phase fraction and color code, respectively, of the α and β phase map.

The total phase fraction from the phase map was determined to be 0.636 and 0.364 for α-Ti and β-Ti, respectively. The approximately 2:1 ratio of α-Ti to β-Ti agrees with BSE images and XRD results shown previously. In order to determine the orientation of the α-

Ti and β-Ti phases of Region 1, a separate study on these phases was done individually as detailed below.

4.4.1.1 α-Ti phase

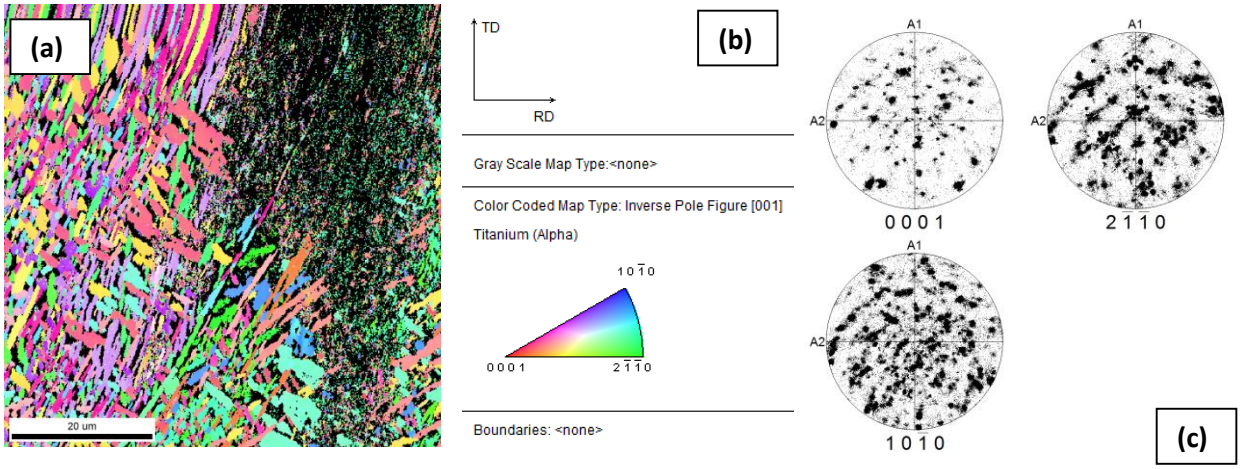

Fig 4.10: α-Ti Phase (a) IPF, (b) ST, (c) PF.

The IPF, ST, and pole figure (PF) configuration are shown in Figs. 4.10: (a), (b), and (c), respectively, for the α-Ti phase. Fig. 4.10 (c) shows the pole figure information of α-Ti for the (0001), (2-1-10) and (10-10) poles.

The PFs indicate that the grains composed of the α phase are randomly oriented suggesting that there is no crystallographic texturing of grains during processing.

4.4.1.2 β-Ti phase

Figs. 4.11 (a) and (b) show the IPF of β Ti and its ST. As this Region under the EBSD scans only two large β grains, the preferred orientation of the β phase cannot be determined. However, texturing of the β (110) grains is bound to be present based on the XRD scan shown in Fig. 4.6(a).

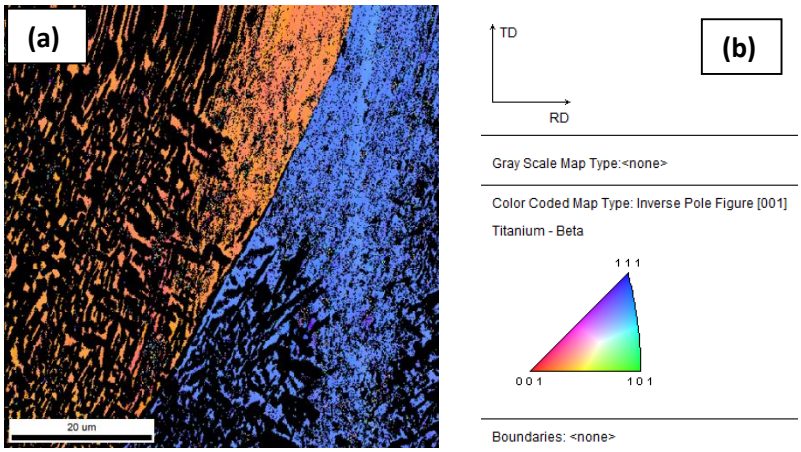

Figure 4.11: β-Ti Phase (a) IPF and (b) ST.

4.4.2 Region 2: Ti-9.6Cr

The EBSD scan in Region 2 was acquired at a 300x300 microns area with a CI of 0.21. Fig. 4.12 (a) shows the SEM image of the area scanned. Fig. 4.12 (b) shows the crystallographic orientation of the phases in different colors. Fig. 4.12 (c) indicates the ST and direction of orientation for β and α phases, while Figs 4.12 (d) and (e) indicate the phase fraction and color code, respectively, of the α and β phase map.

The total phase fraction from the phase map was determined to be 0.371 and 0.629 for α-Ti and β-Ti, respectively. The approximately 1:2 ratio of α-Ti to β-Ti agrees with BSE images and XRD scan results shown previously in a similar composition region.

A clear decrease in α phase fraction is observed with increasing Cr content compared to Region 1. Determination of the orientation of the α and β phases of Region 2was done separately as detailed below.

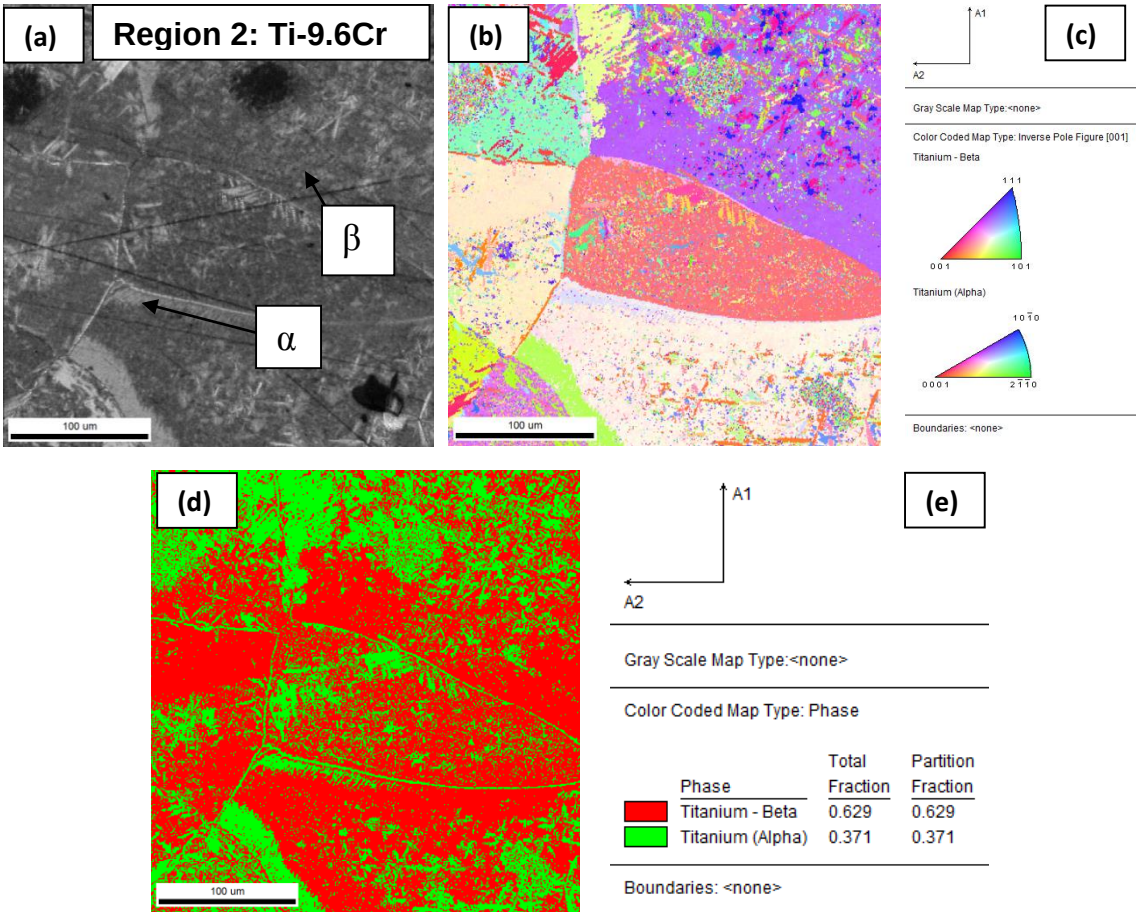

Figure 4.12: SEM-EBSD of Region 2 (a) SE image, (b) IPF, (c) ST, (d) Phase fraction map, and (e) Color code of phases in map.

4.4.2.1 α-Ti phase

The IPF, ST, and PFs are shown in Figs. 4.13 (a), (b), and (c), respectively, for the α-Ti phase. Fig 4.13 (c) shows the pole figure information for the α-Ti (0001), (2-1-10) and (10-10) poles. The PFs show that most of the grains in the [10-10] and [2-1-10] directions are spread randomly suggesting that there is no preferred direction of orientation. Absence of any mechanical testing or heat treatments also play a role for lack of orientation.

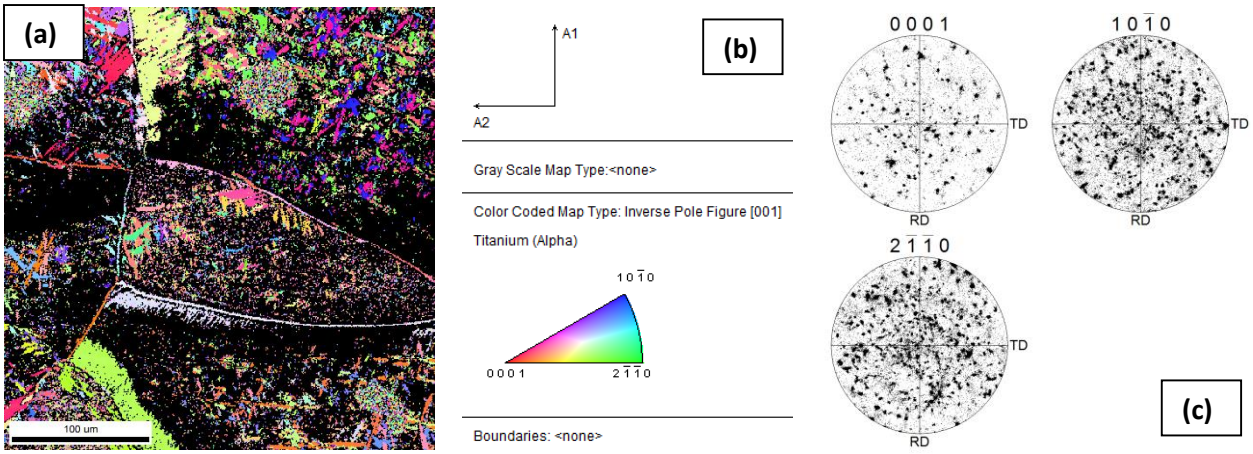

Fig 4.13: α Phase (a) IPF, (b) ST, and (c) PF.

4.4.2.2 β-Ti Phase

Figs. 4.14 (a) and (b) show the IPF of β Ti and its ST. Since only 7 large β grains are being scanned, the preferred orientation of the β phase cannot be determined.

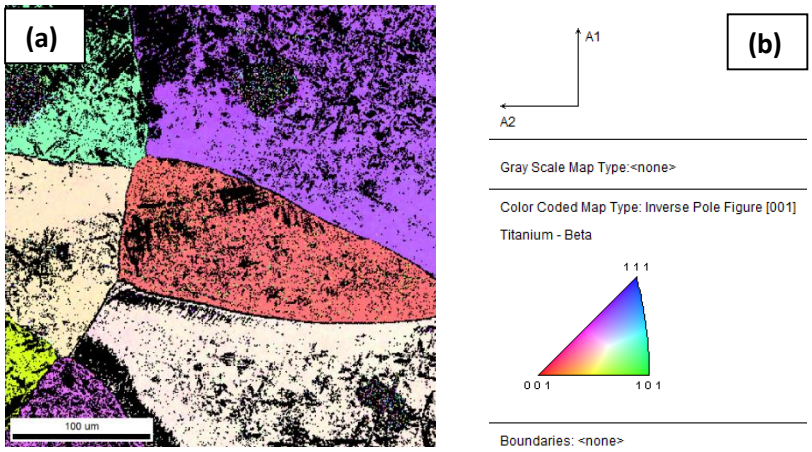

Fig 4.14: β Phase (a) IPF and (b) ST.

4.4.3 Region 4: Ti-19.7Cr

The EBSD scan for region 4 was acquired at a 1250x1250 microns area with a CI of 0.71. A larger area was scanned to encompass more of the grains since they were

expected to be in β phase with a small fraction of α phase grains at the boundaries based on the previously discussed SEM BSE images and XRD scans.

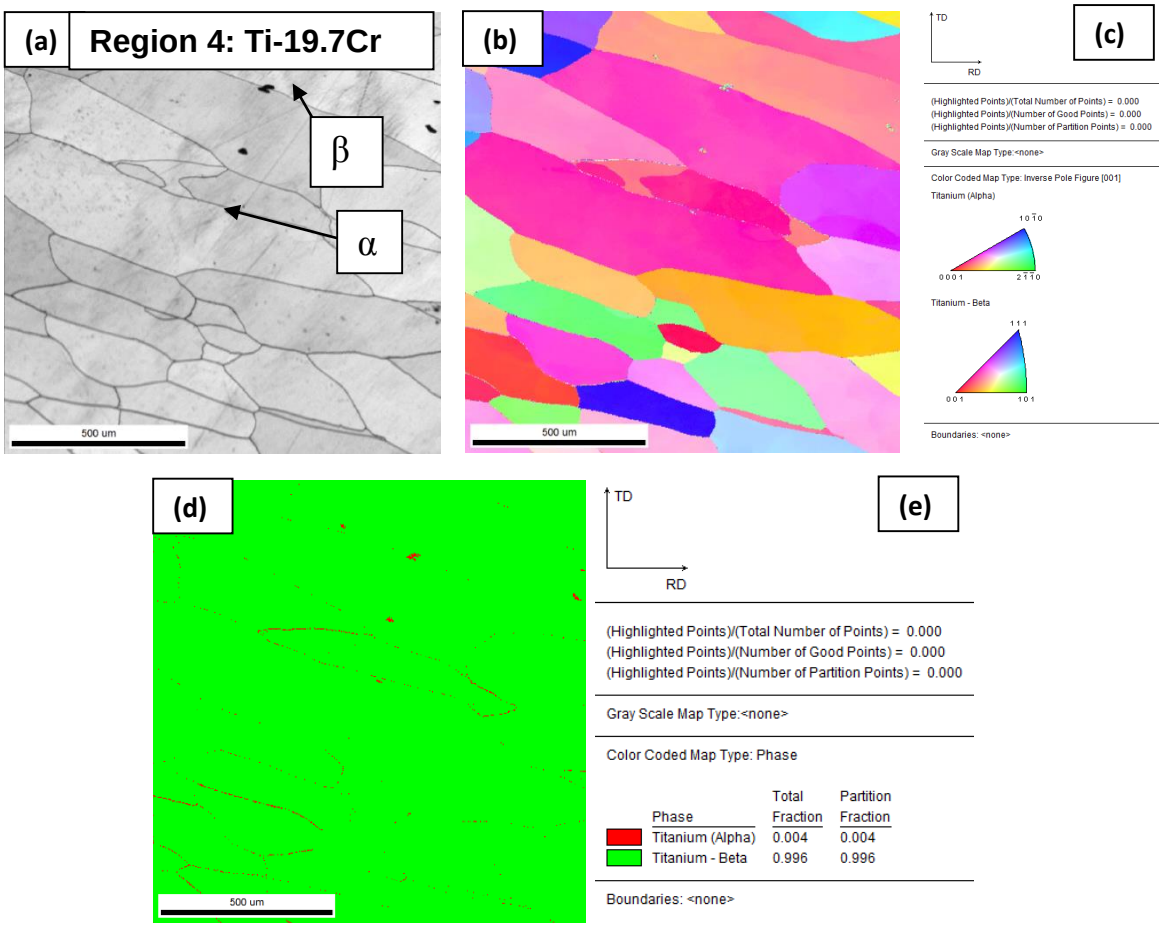

Figure 4.15: SEM-EBSD of Region 4 (a) SE image, (b) IPF, (c) ST, (d) Phase fraction map, and (e) Color code of phases in map.

Fig 4.15 (a) shows the SEM image of the area scanned. Fig 4.15 (b) shows the different crystallographic orientation of the phases in different colors. Fig 4.15 (c) indicates the ST and direction of orientation, while Figs. 4.15 (d) and (e) indicate the phase fraction and color code of the phase map, respectively, for α and β phases.

The total phase fraction from the phase map was determined to be 0.004 and 0.996 for α-Ti and β-Ti, respectively. The dominance of β-Ti phases agrees with BSE images

and XRD scan results shown previously in a similar composition region. Determination of the orientation of the α and β phases of Region 4was done as two separate studies as detailed below.

4.4.3.1 α-Ti phase

The IPF, and ST are shown in Figs. 4.16 (a) and (b), respectively. A minor amount of α-Ti phase is present at the grain boundaries with no crystallographic texturing..

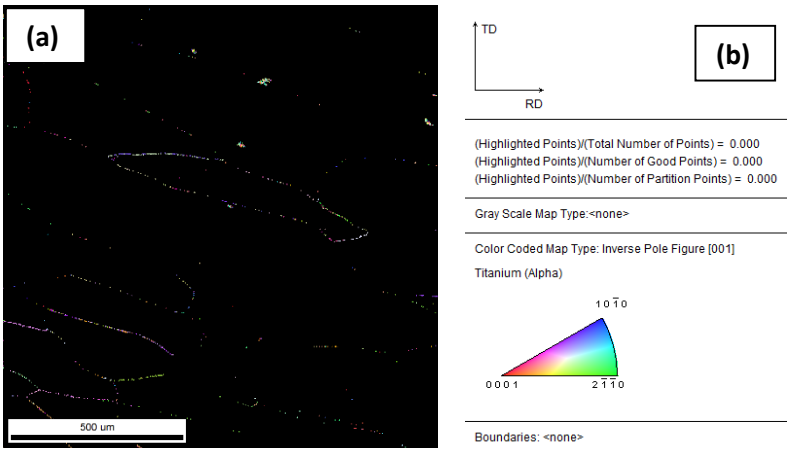

Fig 4.16: α Phase (a) IPFand (b) ST.

4.4.3.2 β-Ti Phase

The IPF, ST, and PF configuration are shown in Figs. 4.17: (a), (b), and (c), respectively, for the β-Ti phase. Fig 4.17 (c) & 4.17(d) show the texture plot and texture range, respectively, of β-Ti at (101), (111) and (001) poles. β phase is observed to have a slightly more preferred orientation or clustering in the [001] direction. Partial clustering at the region scanned indicates the presence of minor texturing of the β phase. However since only a small region is analyzed, it is rather difficult to make a conclusion on the entire sample on basis of the analysis done.

The grain size of the β phase shown in Fig. 4.17(a) is relatively large for the as deposited samples without any mechanical deformation or heat treatment.

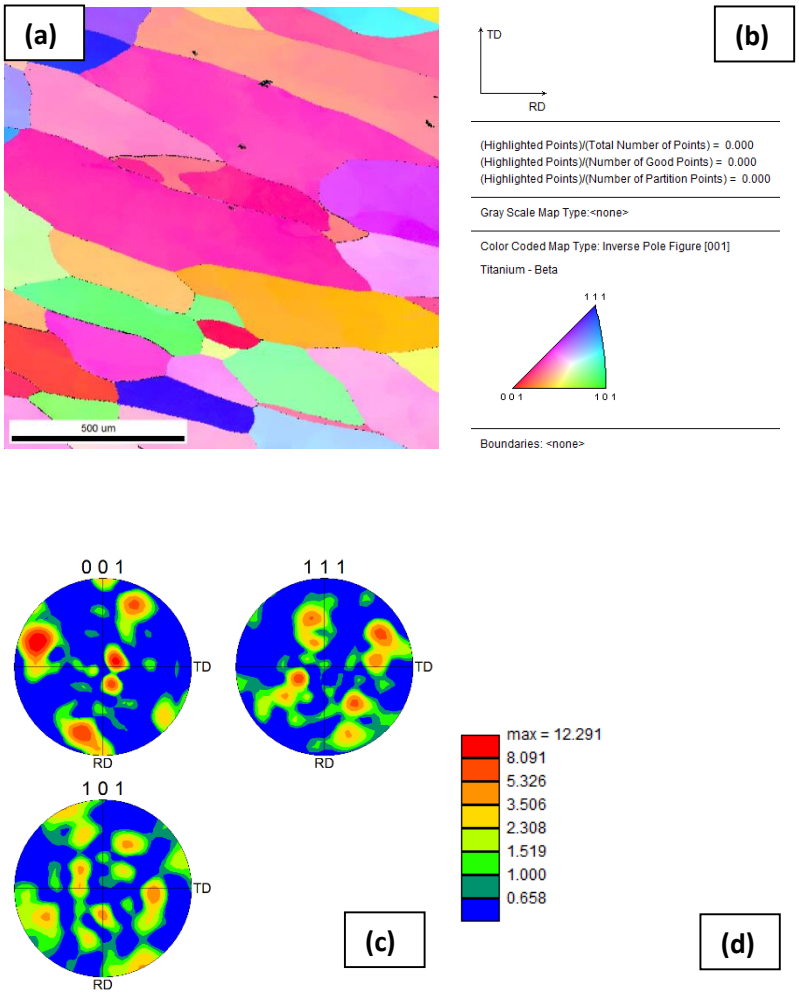

Fig 4.17: β-Ti Phase (a) IPF, (b) ST, (C) Texture plot, (d) Texture range.

4.4.4 Region 5: Ti-31.2Cr

Two EBSD scans were acquired on this particular region due to the interest in studying the $TiCr_2$ intermetallic Laves C15 phase. Unlike the previous lower Cr wt% compositions, there is β phase and $TiCr_2$ intermetallic phase. The BCC (β-Ti) and C15

structure with an FCC lattice ($TiCr_2$) are clearly identified and studied by the two separate scans.

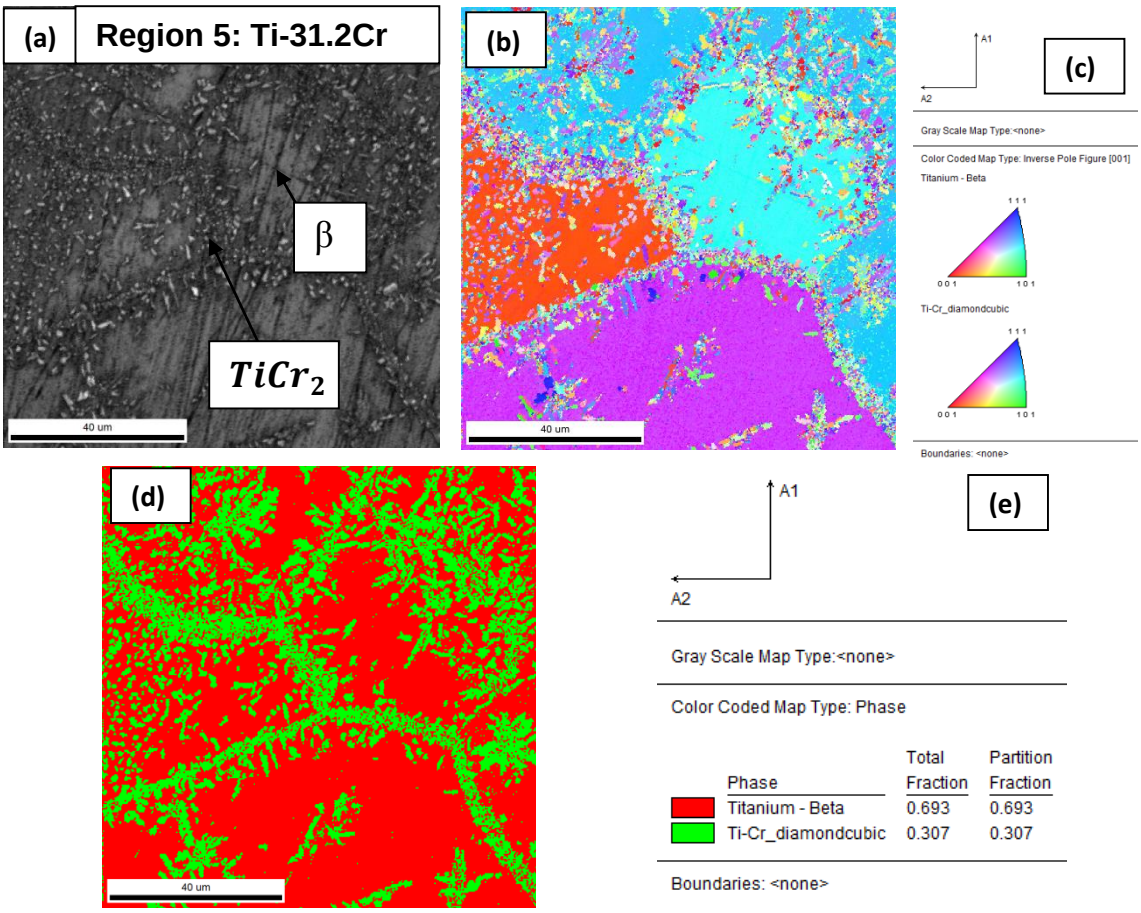

Fig 4.18: SEM-EBSD scan one of Region 5 (a) SE image, (b) IPF, (c) ST, (d) Phase fraction map, and (e) Color code of phases in map.

EBSD Scan 1 is shown in Fig. 4.18 with and an overall scan region of 100x100 microns area with a CI of 0.16. Fig 4.18 (a) shows the SEM image of the area scanned. Fig 4.18 (b) shows the different crystallographic orientation of the phases in different colors and Fig 4.18 (c) indicates the ST and direction of orientation. Figs. 4.18 (d) and (e) indicate the β and $TiCr_2$ phase fractions and color code of the phase map from the EBSD scan.

The total phase fraction from the phase map was determined to be 0.693 and 0.307 for β-Ti and $TiCr_2$, respectively. The phase fraction is expected to be low for the $TiCr_2$ phase, since the formation has been reported to be sluggish in comparison to other phases. The approximately 2:1 ratio of β-Ti to $TiCr_2$ agrees with BSE image in Fig. 4.4(k) and the XRD scan in Fig. 4.7(b) shown previously for this compositional region. Determination of the orientation of the β and $TiCr_2$ phases of Region 5 was done separately as detailed below.

4.4.4.1 β-Ti Phase

The IPF and ST are shown in Figs. 4.19: (a) and (b), respectively, for the β-Ti phase. As the EBSD scan Region is relatively small with only three relatively large β grains, the preferred orientation of the β phase cannot be determined.

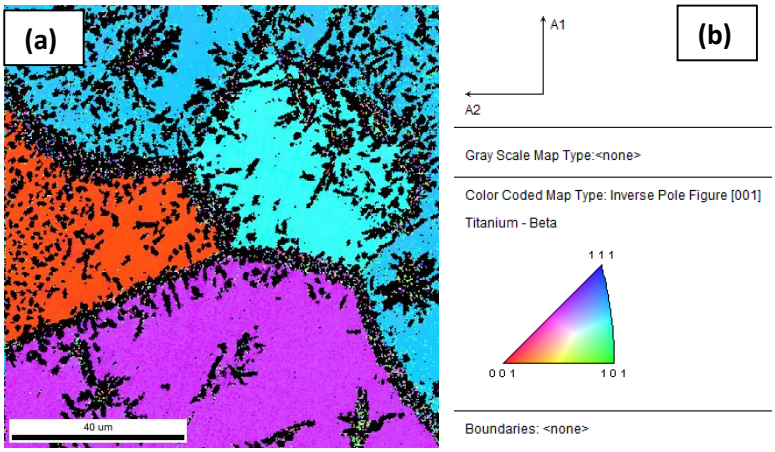

Fig 4.19: β-Ti Phase (a) IPF and (b) ST.

4.4.4.2 $TiCr_2$ phase

The IPF, ST, and PF configuration are shown in Figs. 4.20: (a), (b), (c), respectively, for the $TiCr_2$ phase. Fig 4.20 (c) shows the pole figure information of $TiCr_2$

at (101), (001) and (111) cubic poles. As was the case with the α-Ti and β-Ti grains, the $TiCr_2$ grains are also randomly orientated. The grain distribution of the pole figures also indicates that $TiCr_2$ phase nucleates in the β matrix phase and are mostly present at the β grain boundaries.

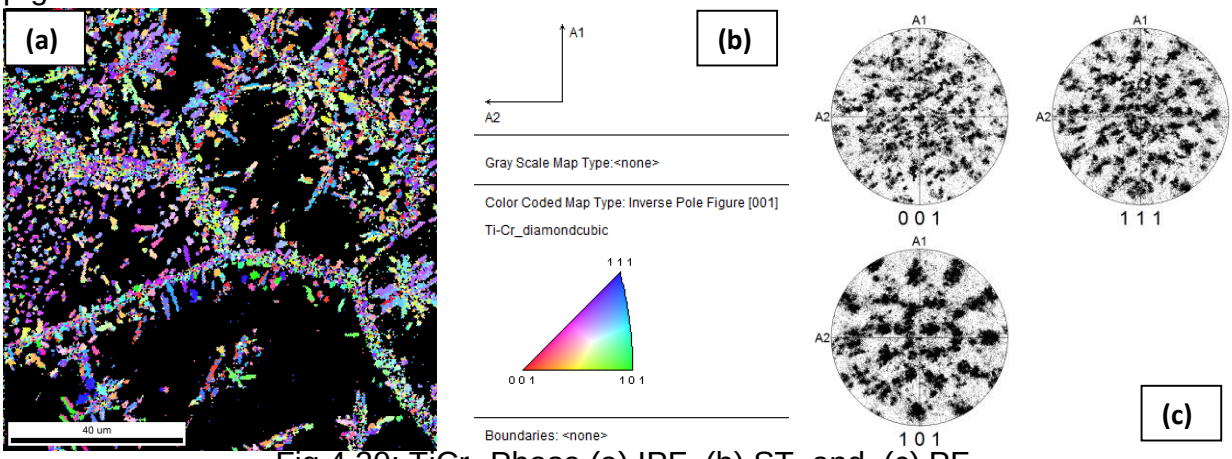

Fig 4.20: $TiCr_2$ Phase (a) IPF, (b) ST, and, (c) PF.

EBSD Scan 2 is shown in Fig. 4.21 with and an overall scan region of 120x120 microns area with a CI of 0.24. Fig. 4.21 (a) shows the SEM image of the area scanned. Fig. 4.21 (b) shows the different crystallographic orientation of the phases in different colors and Fig 4.21 (c) indicates the ST and direction of orientation. Figs. 4.21 (d) and (e) indicate the β and $TiCr_2$ phase fractions and color code of the phase map from the EBSD scan.

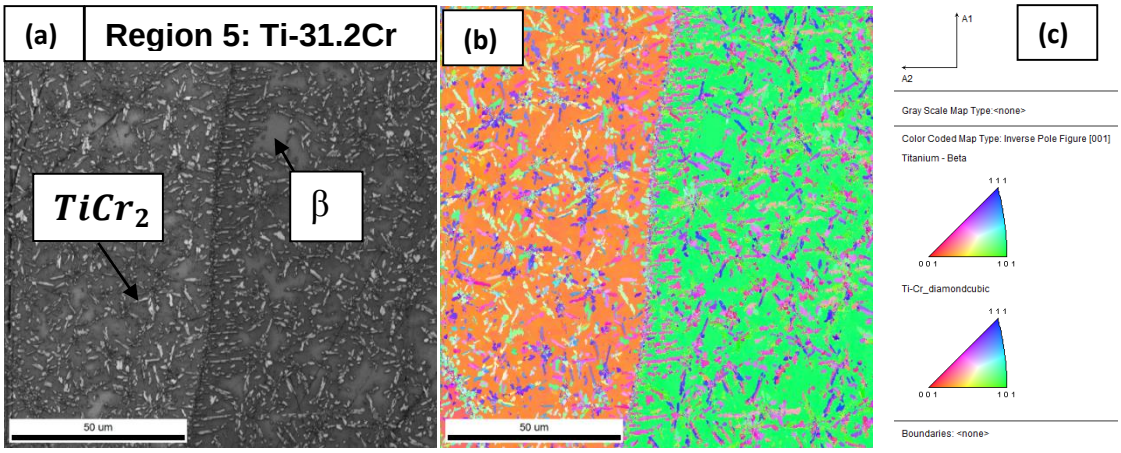

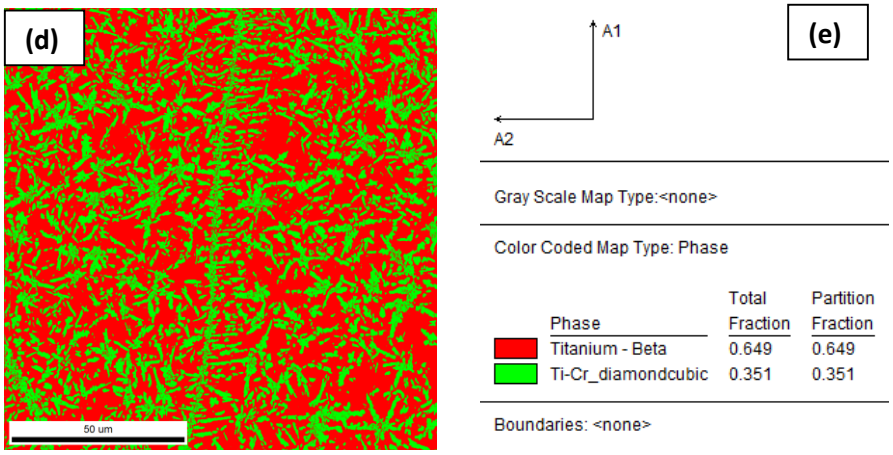

Fig 4.21: SEM-EBSD scan two of Region 5 (a) SE image, (b) IPF, (c) ST, (d) Phase fraction map, and (e) Color code of phases in map.

Similar to EBSD Scan 1 in the same region, the phase fraction of β phase is 0.649 while the $TiCr_2$phase is 0.351. Determination of the orientation of the β and $TiCr_2$ phases of Region 5 was done separately as detailed below.

4.4.4.3 β-Ti Phase

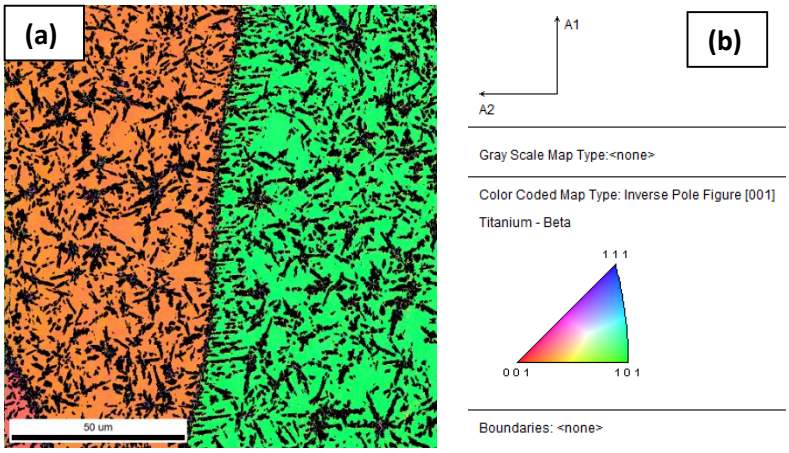

Fig 4.22: β Phase (a) IPF, (b) ST, (c) PF

The IPF and ST are shown in Figs. 4.22 (a) and (b), respectively, for the β-Ti phase. As was the case for the first scan, this region only encompasses two grain so the β-Ti grain orientation cannot be determined.

4.4.4.4 $TiCr_2$ phase

The IPF, ST, and PF configuration are shown in Figs. 4.23 (a), (b), and (c), respectively, for the $TiCr_2$ phase. Fig 4.23 (c) shows the pole figure information of $TiCr_2$ at (101), (110) and (111) cubic poles. Again, the majority of the grains in the crystallographic directions are randomly oriented. Both scans one and two corroborate the XRD phase results shown previously.

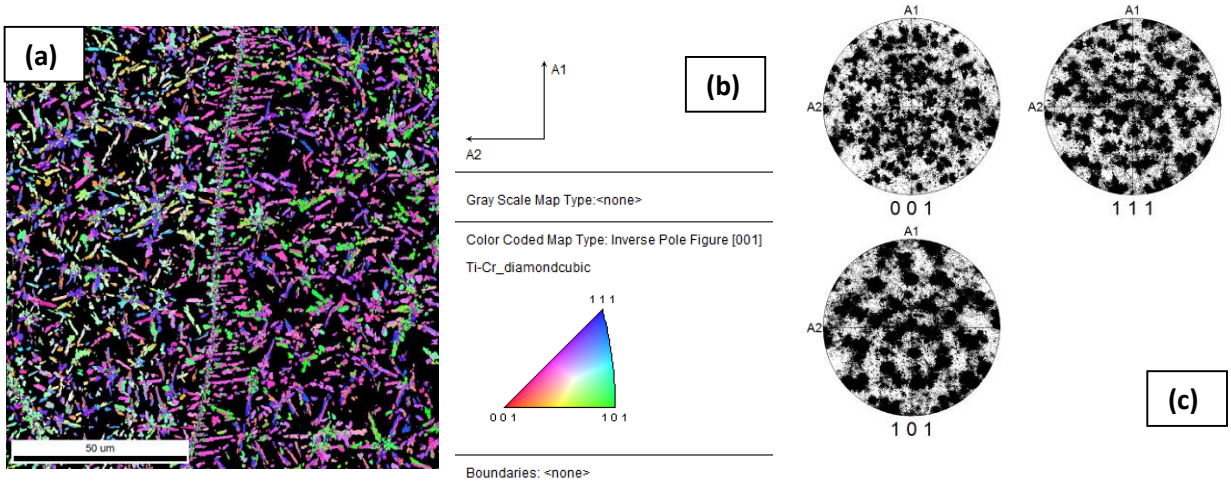

Fig 4.23: $TiCr_2$ Phase (a) IPF, (b) ST, and (c) PF.

4.4.5 Region 6: Ti-29.1Cr

Fig. 4.24 (a) shows the SEM image of the area scanned with β grains. Fig. 4.24 (b) shows the IPF map of the different crystallographic orientation of the β grains. Fig. 4.24 (c) is the ST and Fig. 4.24 (d) & (e) are the texture plots and texture range of the cubic poles. Region 6 is on the top of the deposited sample that received athermal heating

compared to the undercooled Region 5. Region 6 was scanned with an area of 500x500 microns and a CI of 0.35. A large area was scanned as only the β phase was observed in this top region, shown previously with BSE image in Fig. 4.4(l). As expected, only the β phase is present in Region 6 agreeing with the XRD scan shown previously in Fig. 4.7(c).

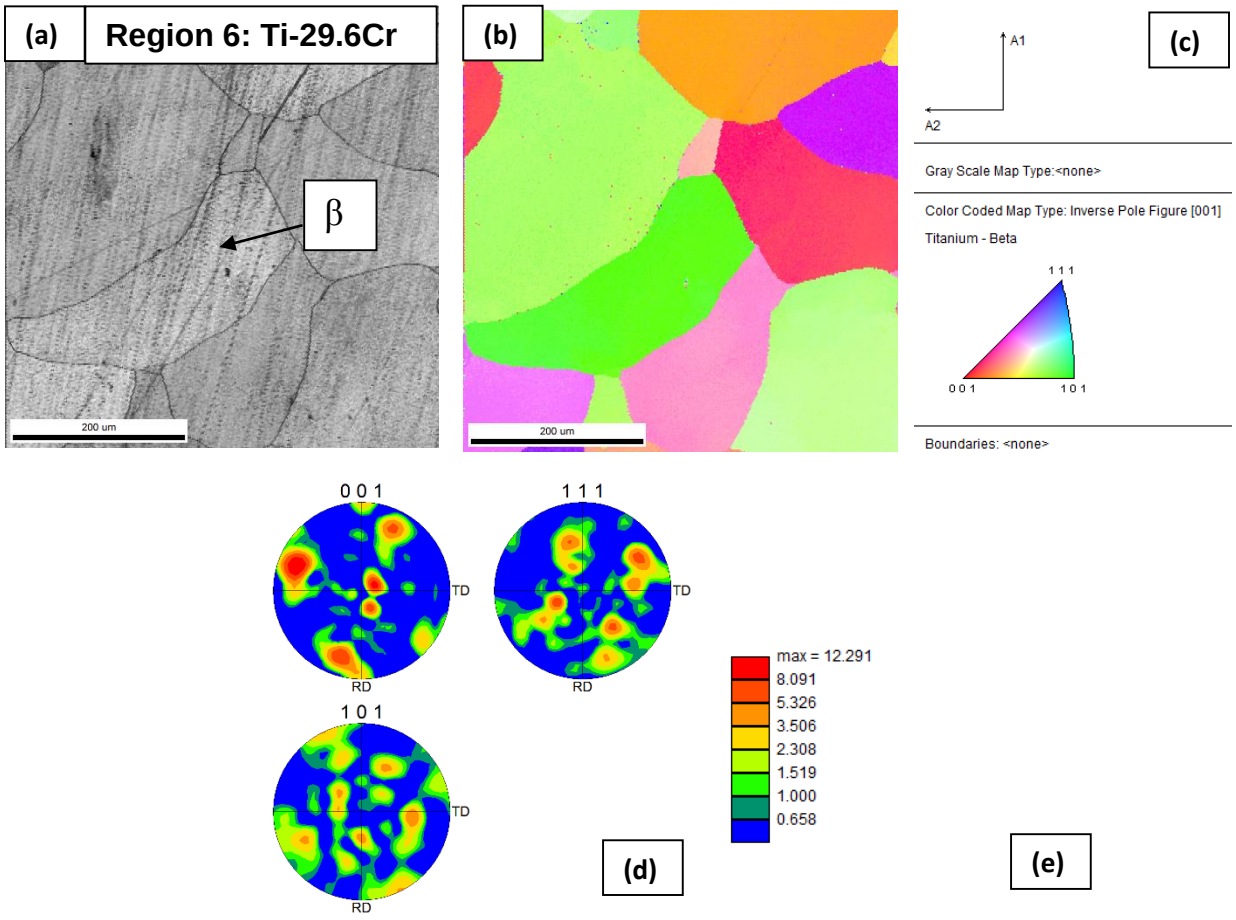

Fig 4.24: SEM-EBSD of Region 6 (a) SE image, (b) IPF map, (c) ST, (d) Texture plot, (e) Texture range

Presence of partial texturing along {001} pole is observed indicating partial clustering of grains in the [001] direction. Similar effects of partial texturing were also

observed by Banerjee et al (11). However a conclusion on the overall texturing of the solidified sample cannot be provide on basis of the small area scanned.

A summary of the IPF maps for all the entire compositional range is shown in Fig. 4.25: (a) – (e). The α phase is dominant at low Cr wt% content and continually decreases with an increase in Cr wt%. At higher compositions of Cr, the $TiCr_2$ phase is then formed. Regions 5 and 6 despite having similar Cr wt% compositions show different microstructures due to thermal gradient during solidification. Overall, the quantitative EBSD phase fraction results agree with the qualitative XRD results and no crystallographic texturing was observed for all compositional ranges.

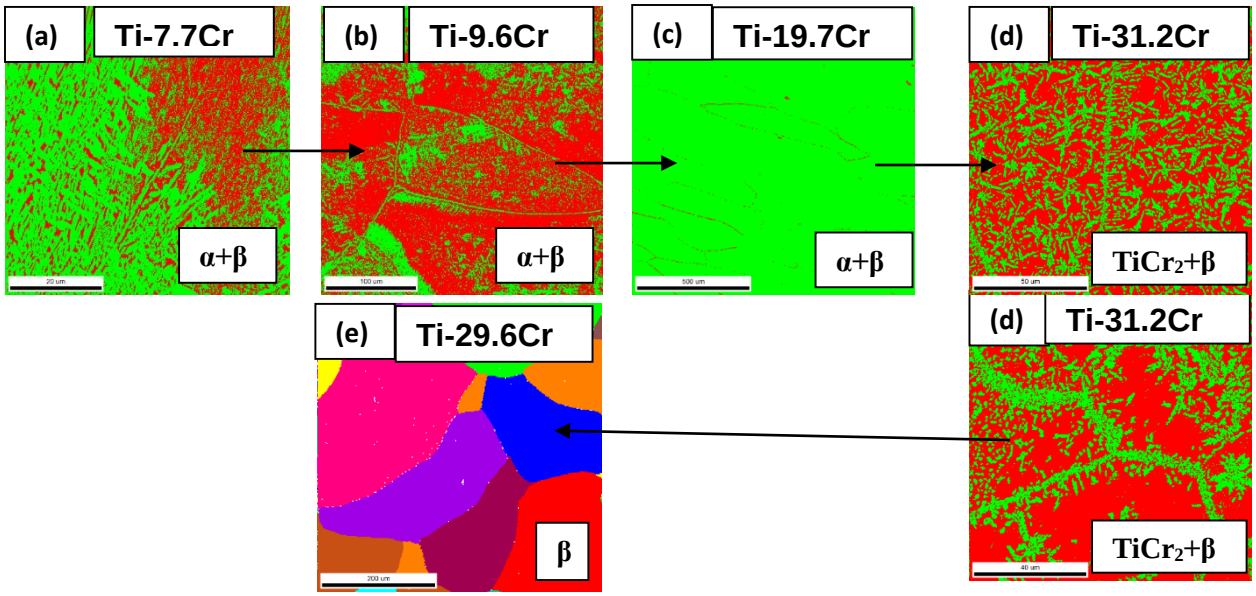

Fig. 4.25: (a)-(e) EBSD IPF maps summary of the microstructural evolution of α-Ti, β-Ti, and $TiCr_2$ phases as a function of increasing Cr wt%.

4.5 Micro-Hardness

Due to the microstructural phase evolution from Ti-10Cr to Ti-30Cr compositional range, there is a gradual change in micro-hardness. Vickers hardness measurements were made along the sample gradient with a spacing of 0.5 mm between indents with three measurements at each location or layer.

Fig. 4.26: (a) and (b) show the hardness values as a function of Cr wt% and distance along the sample, respectively. It is evident that the highest hardness is at Regions of (22-31) wt% Cr in the Ti-Cr alloy due to the presence of the harder $TiCr_2$ intermetallic phase. This phase accounted for an increase in ~100 HV. From Fig. 4.26 (a) we see at about 30 wt% Cr, there is increased and decreased hardness readings.

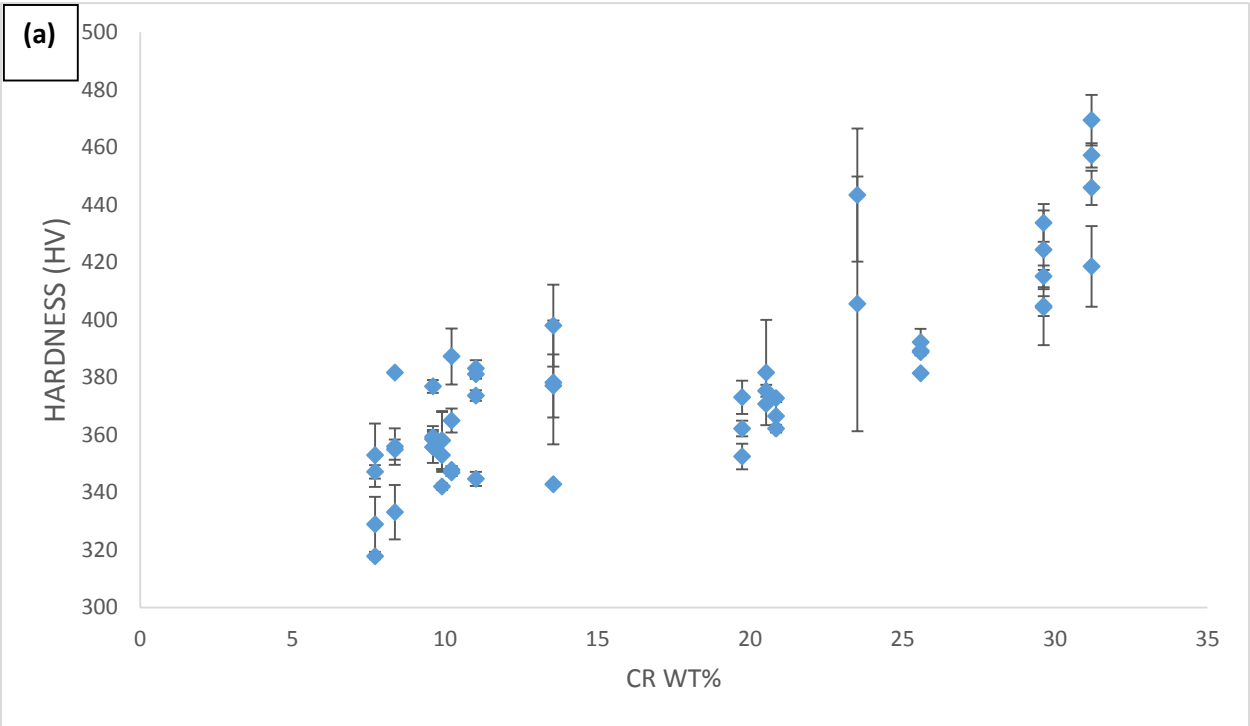

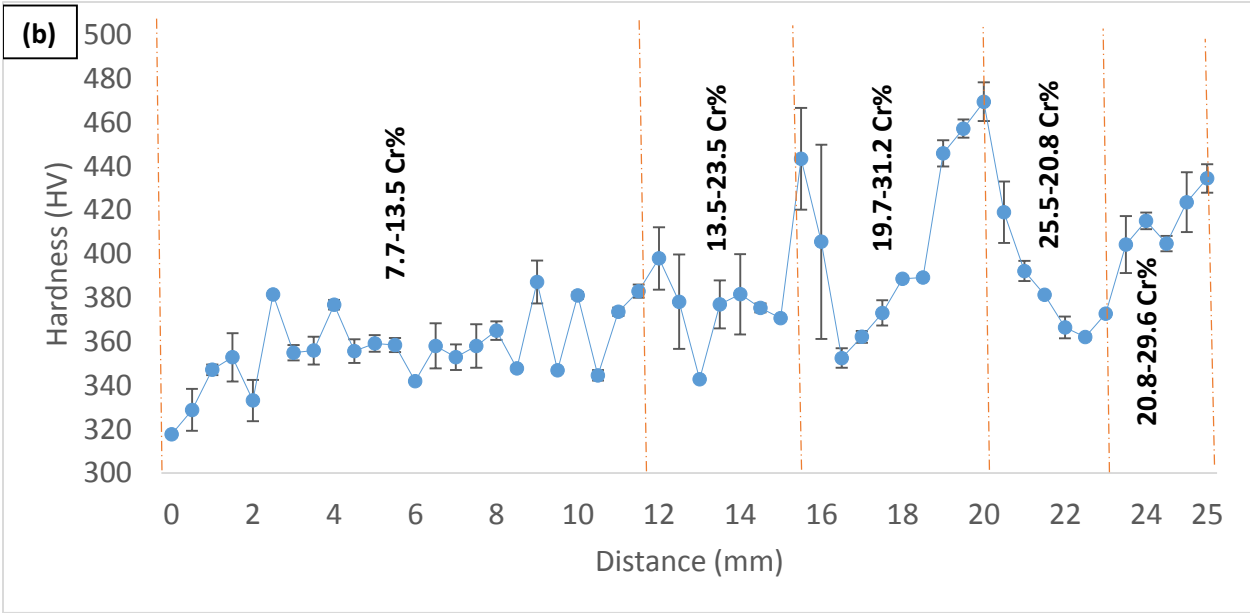

Fig 4.26: Vickers micro-hardness values as a function of (a) Cr wt% and (b) distance along the graded sample.

The increased hardness is the $TiCr_2$ present at the lower layers (Region 5) formed decomposition of β phase into $TiCr_2$ due to uneven reheating effect during the solidification of the alloy via LENS^{TM} processing which has been visualized in Fig 4.4 (k), while the decreased hardness is the dominant β phase in the upper layers (Region 6) with minimal or negligible presence of $TiCr_2$ intermetallic phase depicted in Fig 4.4 (l).

In summary, the as-deposited LENS^{TM} Ti-10Cr to Ti-30Cr compositionally graded alloy was characterized by SEM BSE imaging, XRD, EBSD and micro-hardness measurements to determine processing-structure-property relations. The α-Ti, β-Ti, and $TiCr_2$ phases were identified in varying phase fractions which was influential in determining the hardness values. These results for the as-deposited sample will serve as a baseline to compare to the air cooled and furnace cooled samples that will be presented next in chapters 5 and 6.

Chapter 5

INFLUENCE OF Cr CONCENTRATION ON MICROSTRUCTURAL PHASE EVOLUTION AND ITS EFFECTS ON HARDNESS IN HEAT TREATED AND FURNACE COOLED Ti-xCr ALLOYS

5.1 Introduction

The effect of compositional variation of Cr concentration on heat treated and furnace cooled (1000°C for 30 min) LENS^{TM} deposited Ti-xCr (Ti-xCr: 10≤x≤30wt %) is studied and discussed. The binary alloy is assessed, by means of XRD scans, SEM imaging, EBSD scans, TEM analysis on a few select regions, and Micro-Hardness measurements. The results obtained from the heat treated and furnace cooled alloy experiments are compared to as-deposited alloys presented in Chapter 4.

5.2 Microstructural Evolution Studied by SEM

The microstructural and compositional evolution of the furnace cooled Ti-10Cr to Ti-30Cr graded alloy were studied by BSE imaging and EDS, respectively. Fig. 5.1 shows a schematic of the analysis regions along which BSE imaging and EDS scans were conducted on the graded alloy. Fig 5.2 (a)-(g) and Fig. 5.3 (a)-(e) show representative BSE image comparisons for low and high wt% Cr contents, respectively, along the length of the different regions of the alloy. Fig. 5.4 (a)-(k) summarizes the entire compositional range at a higher BSE image magnification. The microstructural phases based on the phase diagram that are to be expected to be present are α-Ti, β-Ti, and $TiCr_2$. These phases are also seen in studies by Banerjee et al (11) and Samimi et al (41). The images

in Figs. 5.2-5.4 have the corresponding Cr wt% values that were determined by EDS acquired along each region for multiple scans. The compositional changes along the length of the sample are summarized in table 5.1. The height occupied by each region is approximated to be 1.25mm. While there is a trend of increasing Cr content along the length of the alloy, there is some statistical variation in sub-regions. Thus, it is not a uniformly compositionally graded alloy due to the variation in heat transfer during LENS™ processing.

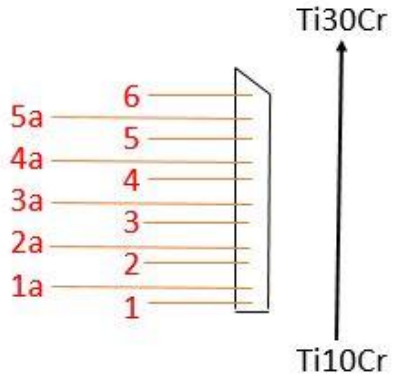

Fig 5.1: Schematic representation of Regions and Sub-regions for acquiring BSE images and EDS scans.

From Fig 5.2 (a)-(g), it is evident that the β phase is the matrix, and the α phase precipitate is a product of the eutectoid reaction. The presence of α phase at hypo eutectoid regions from Region 1: Ti-7.9Cr to Region 4a: Ti-15Cr is observed in large volume fractions. However unlike the “as deposited” sample, α phase has precipitated as dendritic structures homogenously throughout the sample at low Cr wt% regions. Heat treatment (undercooling), due to the slow furnace cooling, has facilitated an even distribution of the α phase within the β matrix.

The α phase content reduces with the increase in Cr content along the length of the sample. Chromium being a β stabilizing element in the alloy system suppresses the extensive formation of the α phase.

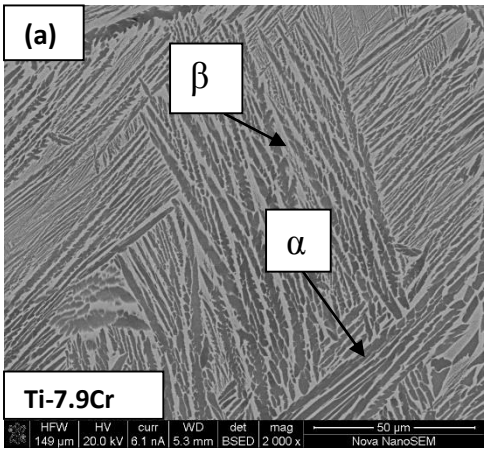

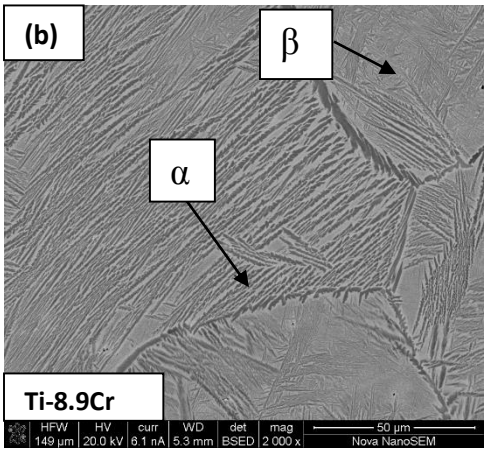

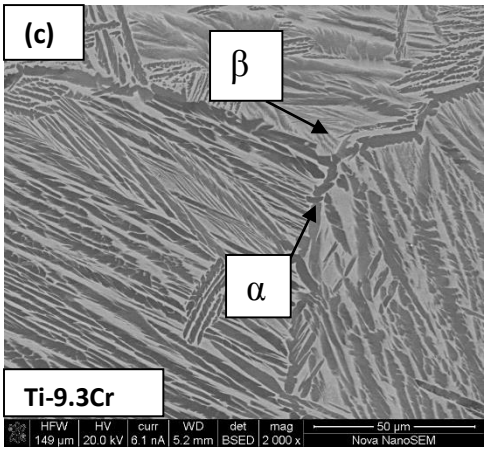

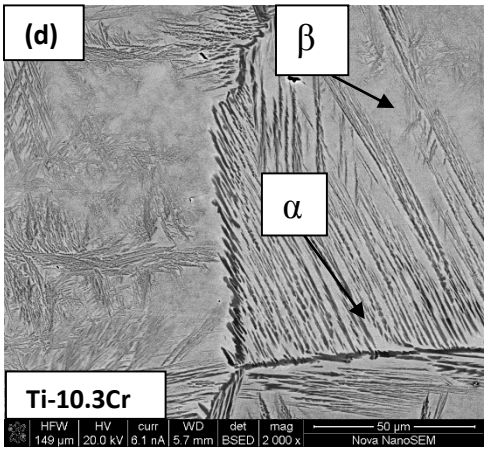

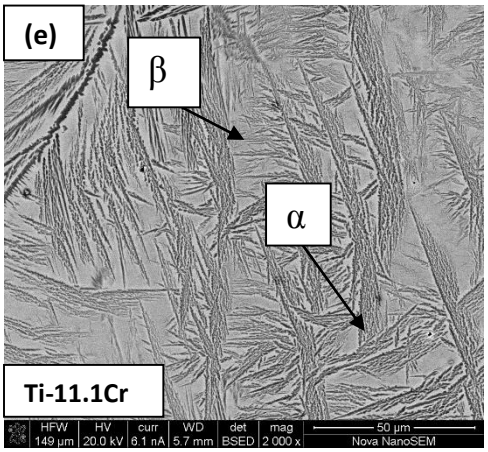

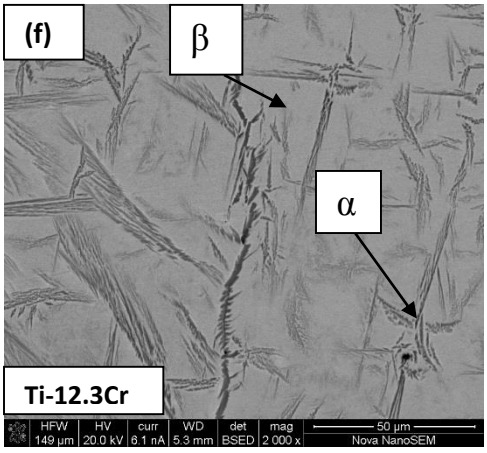

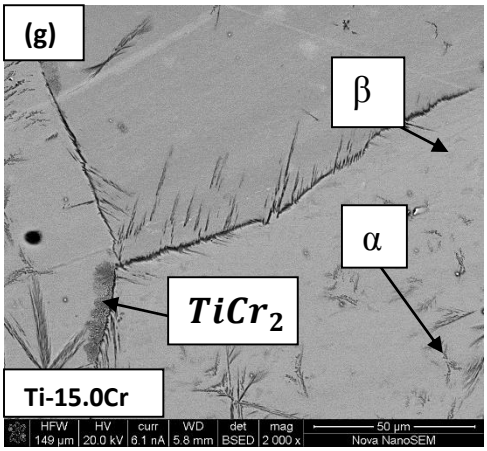

Fig 5.2: (a)-(g) BSE images showing microstructural changes for low Cr (7-15) wt% alloys.

REGION	COMPOSITION (wt%)	REGION	COMPOSITION (wt%)	REGION	COMPOSITION (wt%)
1	Ti-7.9Cr	3	Ti-10.3Cr	5	Ti-24.1Cr Ti-29.2Cr
1a	Ti-9.1Cr	3a	Ti-11.1Cr	5a	Ti-29.0 Cr Ti-22.4Cr
2	Ti-8.5Cr	4	Ti-11.7Cr	6	Ti-31.2Cr
2a	Ti-8.9Cr	4a	Ti-12.3Cr, Ti-15.0Cr Ti-17.9Cr Ti-20.9Cr		

Table 5.1: EDS determined compositions of the various regions and sub-regions.

Unlike the “as deposited” sample, the α phase has been observed throughout the alloys system at different compositions including regions of high Cr wt% in Fig. 5.3 where three phases co-exist. This occurrence is due to the undercooling at β-tranus temperature

followed by slow cooling, leading to the precipitation of α phase followed by the sluggish formation of $TiCr_2$ (Laves phase C15) intermetallic phase.

From Fig 2.2, the phase diagram indicates that the β phase undergoes a eutectoid reaction at ~13wt% Cr where it decomposes into α and $TiCr_2$ phases. The α phase reduces drastically in volume fraction as the chromium concentrations rise above 15 wt% Cr, a hyper eutectoid region. The initial intermetallic $TiCr_2$ formation at Ti-15.0Cr a hyper eutectoid region, shown in Fig 5.2: (g,) occurs at grain boundaries and continues to increase with increase in Cr content along with the depletion of the α phase. The presence of three phases is expected to create a region of high hardness.

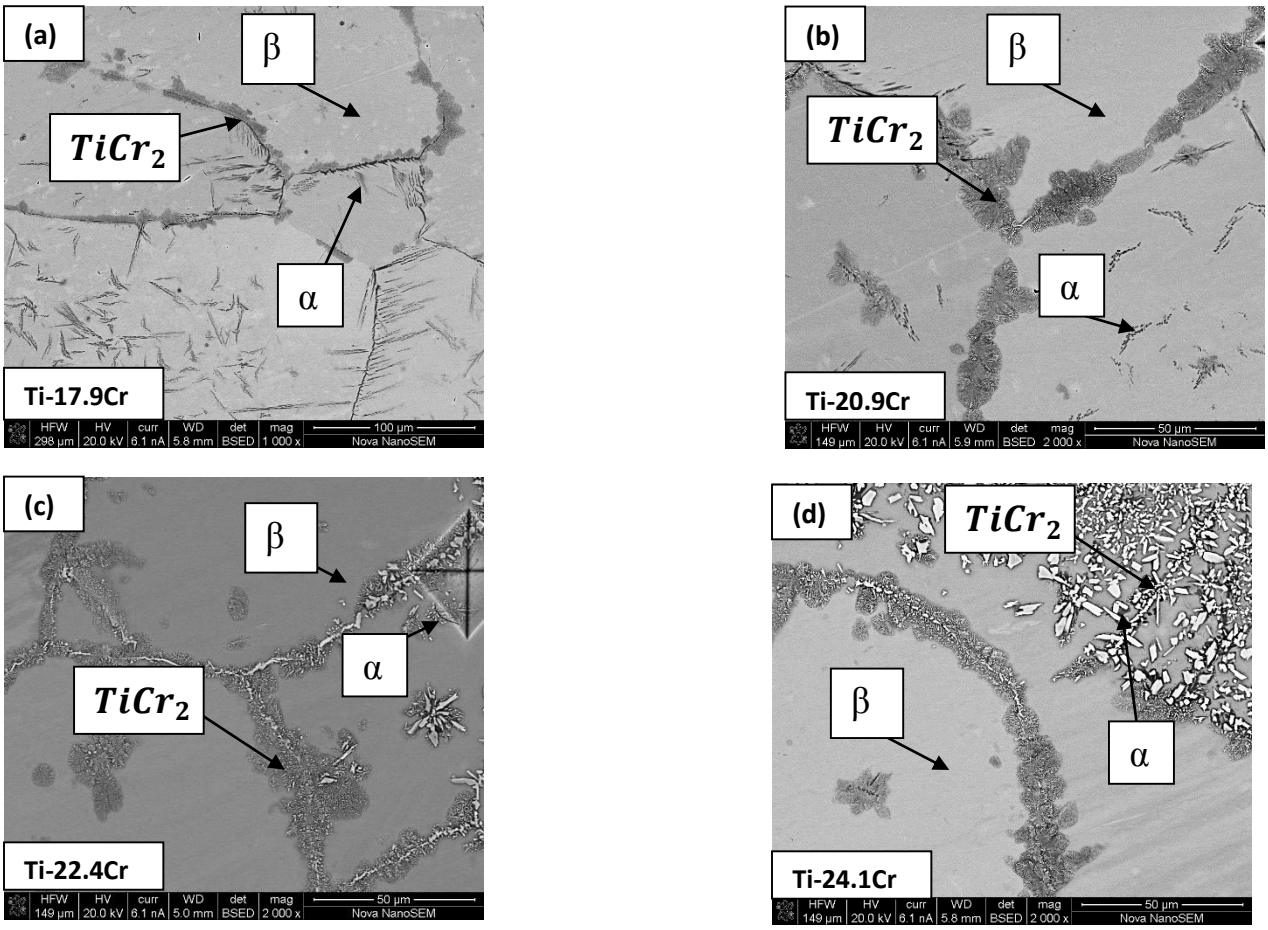

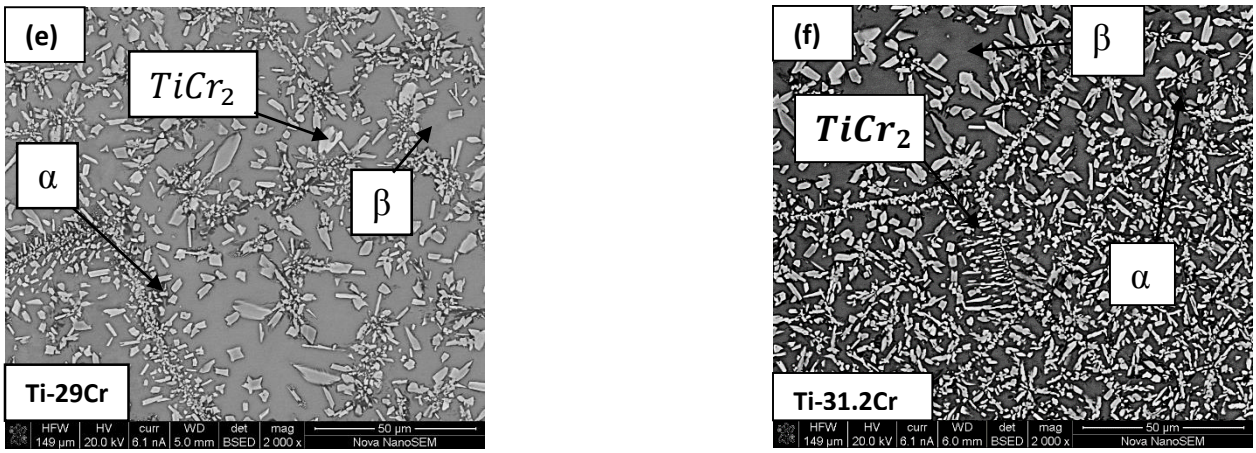

Fig 5.3: (a)-(f) BSE images showing microstructural changes at high Cr (17-30) wt%.

Although the formation of $TiCr_2$ has been recorded as a sluggish reaction, Region 6: Ti-31.2Cr similar in composition with Region 5: Ti-29.0Cr, shows a dominant presence of $TiCr_2$ phase in both regions, which is in contrast to the 'as deposited" alloy. The heat treatment of the alloy, followed by furnace cooling enables Region 5 (lower layer) and Region 6 (upper region) to be undercooled evenly. This facilitates the formation of the α phase followed by the sluggish $TiCr_2$ intermetallic phase which in turn depletes the already formed α phase.

A summary of SEM BSE images taken at higher magnification for the entire compositional range along the different regions is shown in Fig 5.4: (a)-(k).

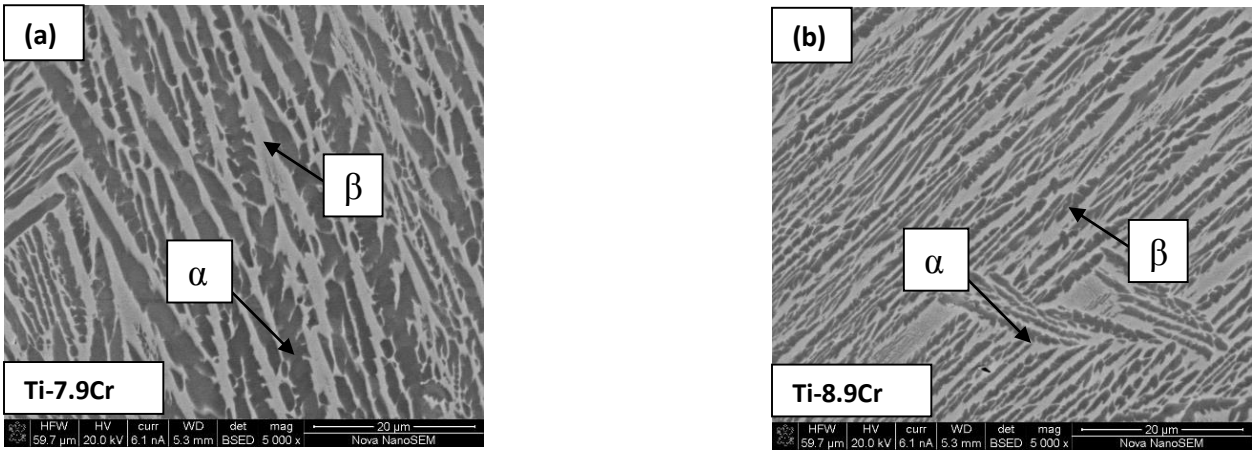

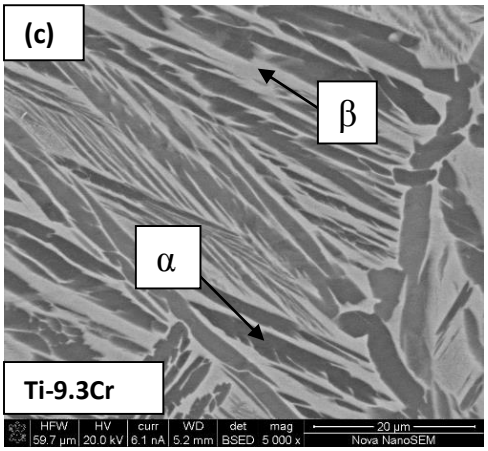
(c)
β
α
Ti-9.3Cr
HFW 59.7 µm | HV 20.0 kV | curr 6.1 nA | WD 5.2 mm | det BSED | mag 5 000 x | 20 µm | Nova NanoSEM

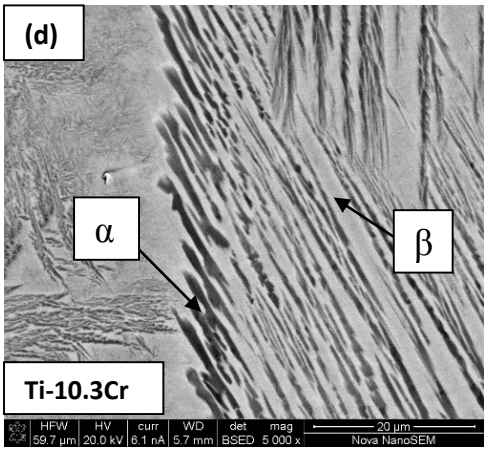
(d)
α
β
Ti-10.3Cr
HFW 59.7 µm | HV 20.0 kV | curr 6.1 nA | WD 5.7 mm | det BSED | mag 5 000 x | 20 µm | Nova NanoSEM

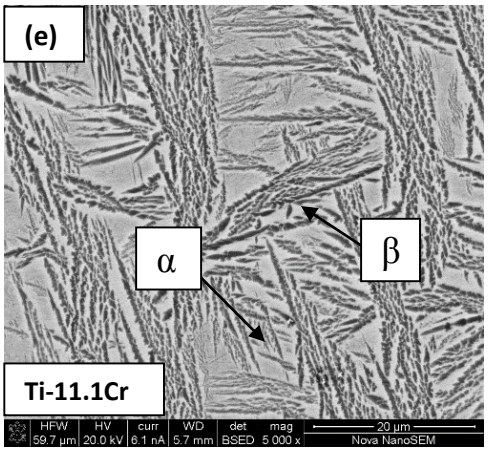
(e)
α
β
Ti-11.1Cr
HFW 59.7 µm | HV 20.0 kV | curr 6.1 nA | WD 5.7 mm | det BSED | mag 5 000 x | 20 µm | Nova NanoSEM

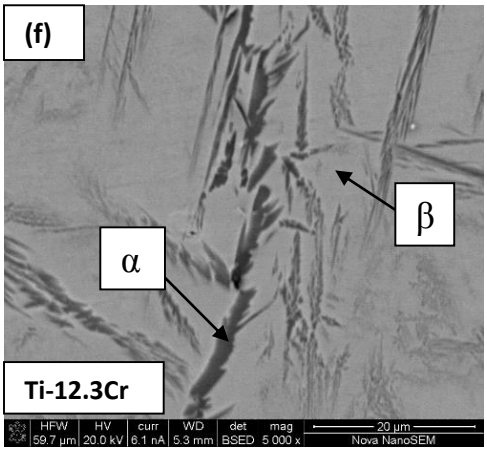
(f)
β
α
Ti-12.3Cr
HFW 59.7 µm | HV 20.0 kV | curr 6.1 nA | WD 5.3 mm | det BSED | mag 5 000 x | 20 µm | Nova NanoSEM

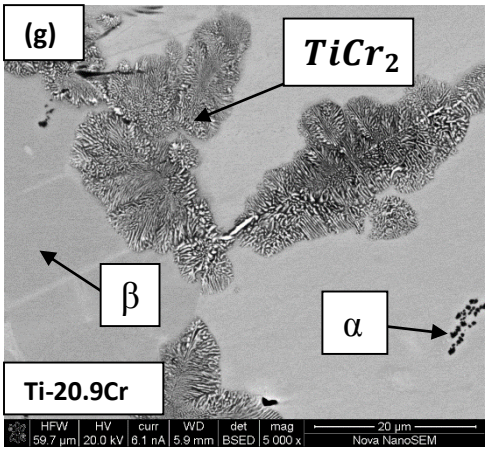
(g)
$TiCr_2$
β
α
Ti-20.9Cr
HFW 59.7 µm | HV 20.0 kV | curr 6.1 nA | WD 5.9 mm | det BSED | mag 5 000 x | 20 µm | Nova NanoSEM

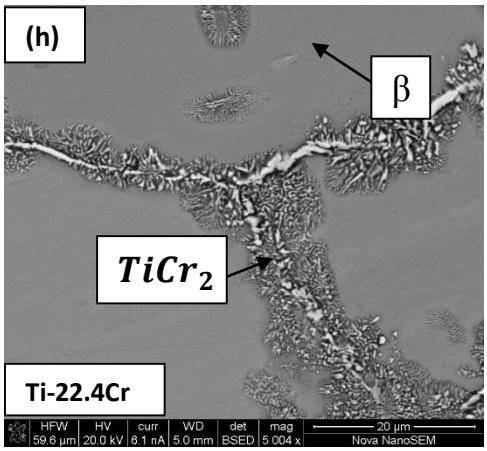
(h)
β
$TiCr_2$
Ti-22.4Cr
HFW 59.6 µm | HV 20.0 kV | curr 6.1 nA | WD 5.0 mm | det BSED | mag 5 004 x | 20 µm | Nova NanoSEM

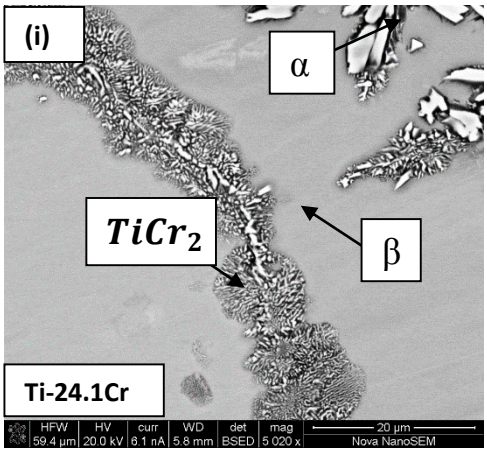

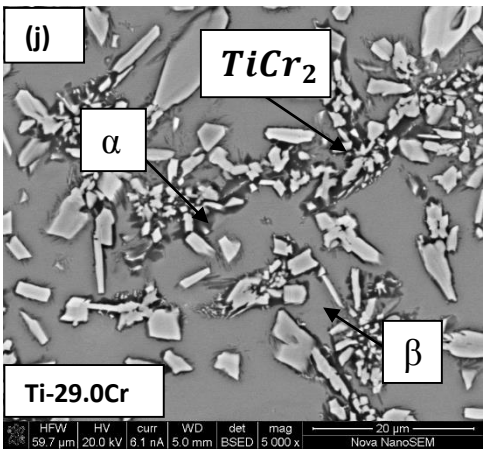

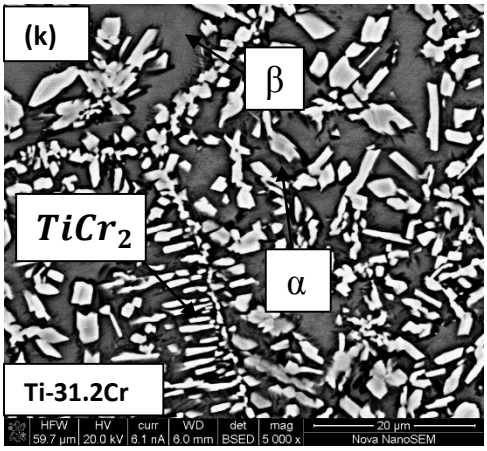

Fig 5.4: (a)-(k) Summary of higher magnification BSE images along entire Cr compositional range.

5.3 X-Ray Diffraction (XRD)

XRD of the graded alloy was conducted along 6 different regions shown schematically in Fig. 5.5. The regions were selected on basis of their compositional gradient and change in microstructure. A slit size of H2 was done for 6 scans to provide a more concise scan than a broad one at a particular region.

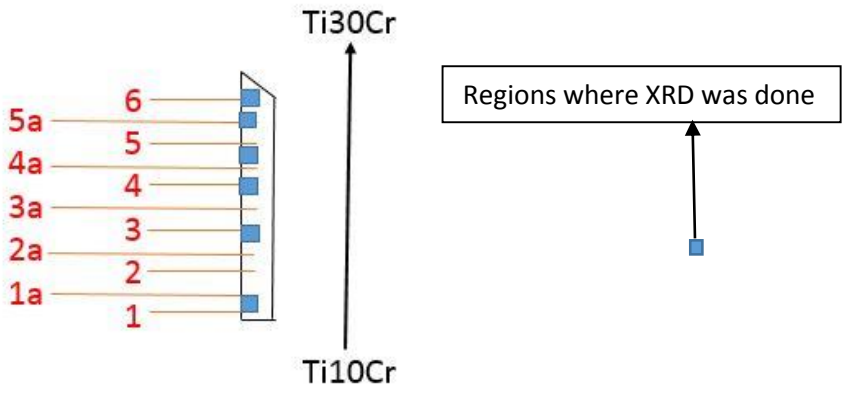

Fig 5.5: Schematic Representation of the Regions and Sub-regions for acquiring XRD scans

The various XRD scans obtained for different regions with respect to increasing Cr content are shown in Fig 5.6: (a)-(c) and Fig 5.7: (a)-(c) for low and higher wt% Cr contents, respectively. XRD scans of hypo eutectoid regions at Region 1: Ti-(7.9-8.5)Cr, Region 3: Ti-(10.3-11.7)Cr and Region 4: Ti-(11.7-12.3)Cr shows the presence of α-Ti (HCP) and β-Ti (BCC) shown in Fig 5.6: (a)-(c). Since chromium is a β stabilizer, there is an increase in the content of β-Ti with increasing Cr wt% along the length of the graded alloy. This leads to an increase in the intensity and number of β peaks indexed while there is a reduction in the indexed α peaks. The XRD results in Fig 5.6 (a)-(c) are similar to that observed in for “as deposited” samples in chapter 4 except the intensities of the α peaks have increased indicating an increase in phase content which agrees with above SEM images.

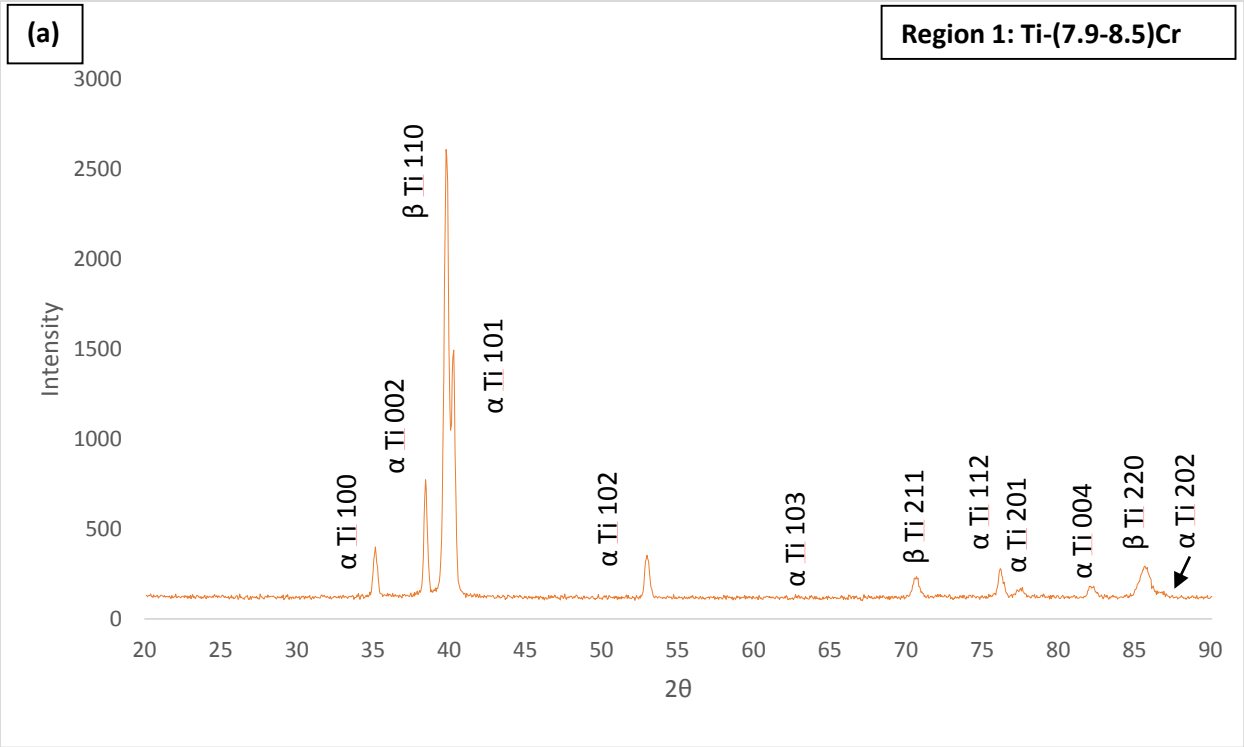
(a)
Region 1: Ti-(7.9-8.5)Cr
Intensity
2θ
α Ti 100
α Ti 002
β Ti 110
α Ti 101
α Ti 102
α Ti 103
β Ti 211
α Ti 112
α Ti 201
α Ti 004
β Ti 220
α Ti 202

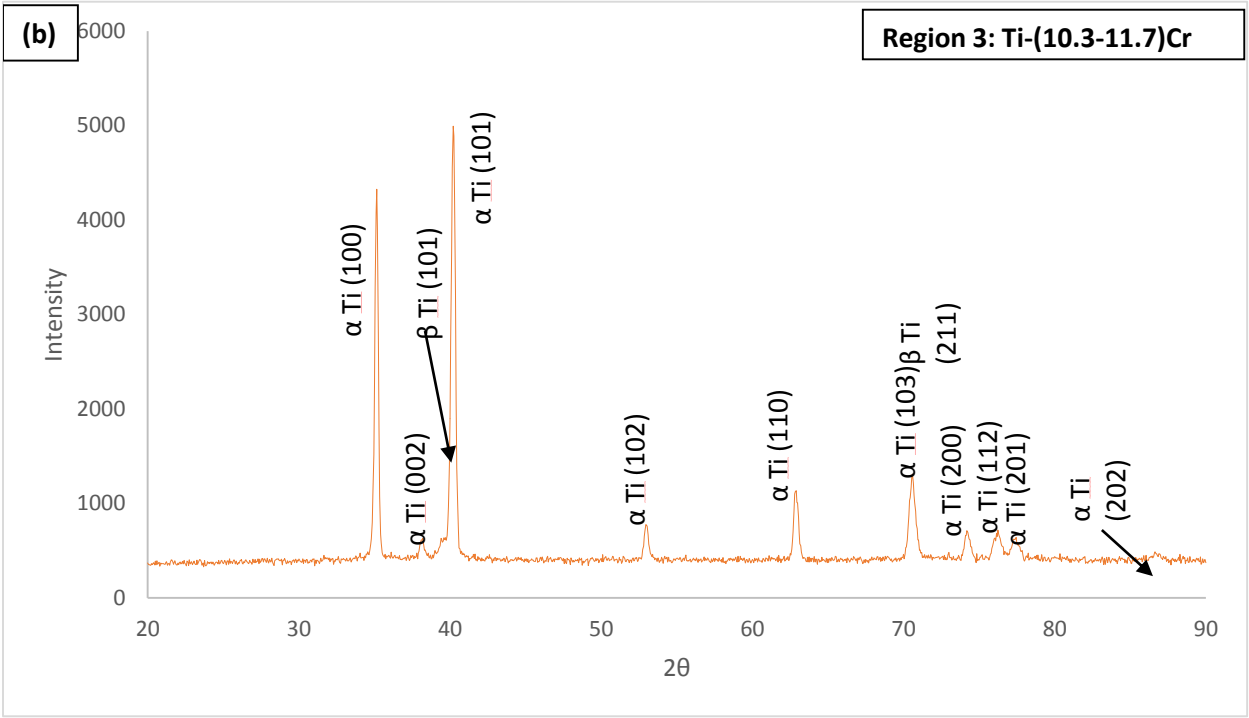
(b)
Region 3: Ti-(10.3-11.7)Cr
Intensity
2θ
α Ti (100)
β Ti (101)
α Ti (101)
α Ti (002)
α Ti (102)
α Ti (110)
α Ti (103)
β Ti (211)
α Ti (200)
α Ti (112)
α Ti (201)
α Ti (202)

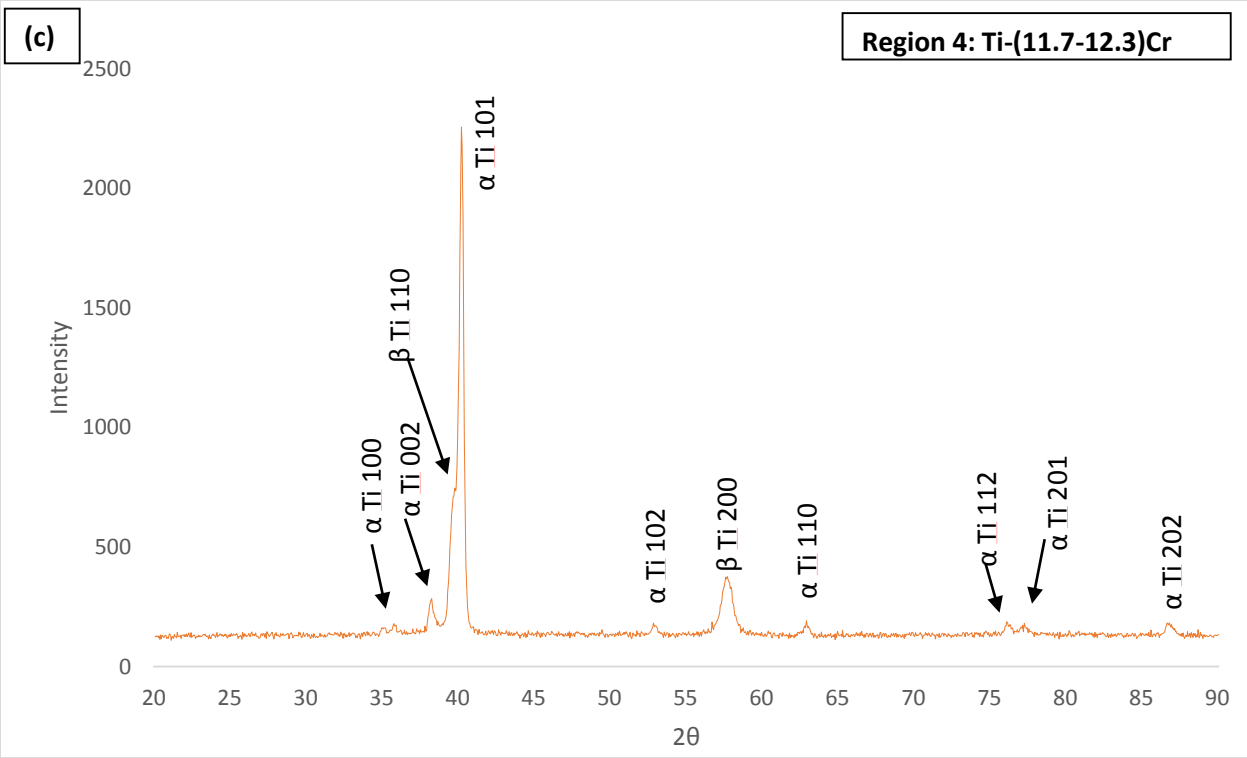

Fig 5.6: XRD scans of low Cr wt% Regions (a) Ti-(7.9-8.5)Cr, (b) Ti-(10.3-11.7)Cr, (c)Ti-(11.7-12.3)Cr

In addition, β peak shifts have been observed in the diffraction patterns from Fig 5.6 (a)-(c). The probable causes for the peak shifts are choice of β stabilizing Cr as an alloying element, heat treatment of the alloy, as well as stresses induced during EDM cutting of the sample. Peak shifts were also observed in Ti-Cr alloy study conducted by Hsueh-Chuan Hsu et al (26).

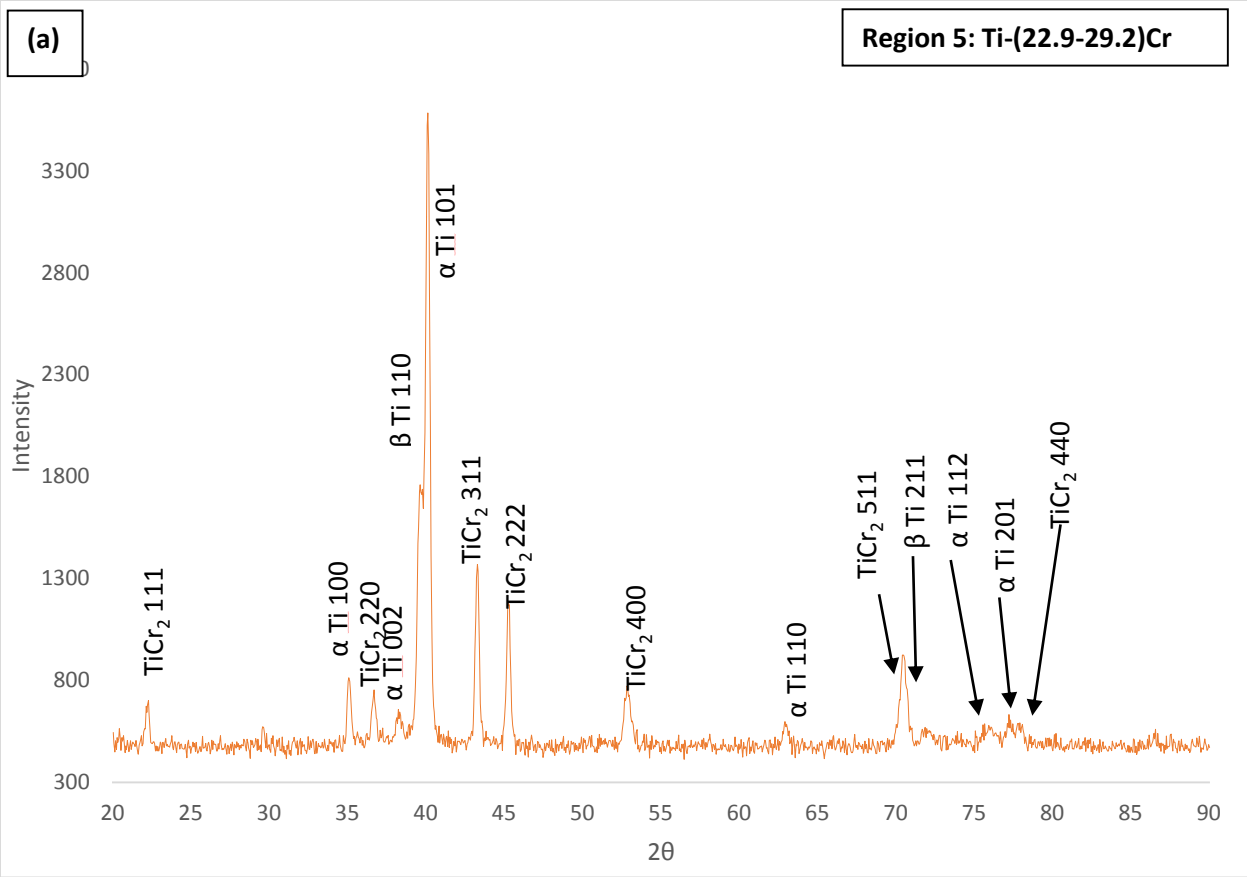
(a)
Region 5: Ti-(22.9-29.2)Cr
Intensity
2θ
TiCr2 111
α Ti 100
TiCr2 220
α Ti 002
β Ti 110
α Ti 101
TiCr2 311
TiCr2 222
TiCr2 400
α Ti 110
TiCr2 511
β Ti 211
α Ti 112
α Ti 201
TiCr2 440

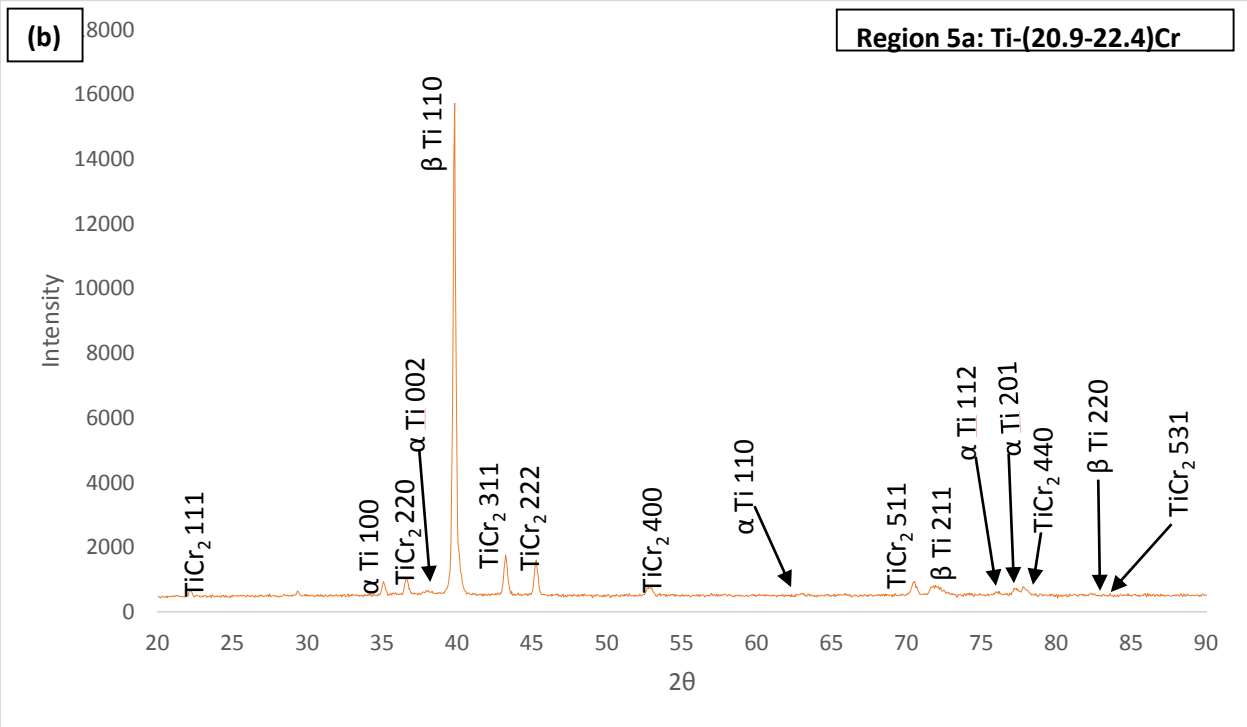
(b)
Region 5a: Ti-(20.9-22.4)Cr
Intensity
2θ
TiCr2 111
α Ti 100
TiCr2 220
α Ti 002
β Ti 110
TiCr2 311
TiCr2 222
TiCr2 400
α Ti 110
TiCr2 511
β Ti 211
α Ti 112
α Ti 201
TiCr2 440
β Ti 220
TiCr2 531

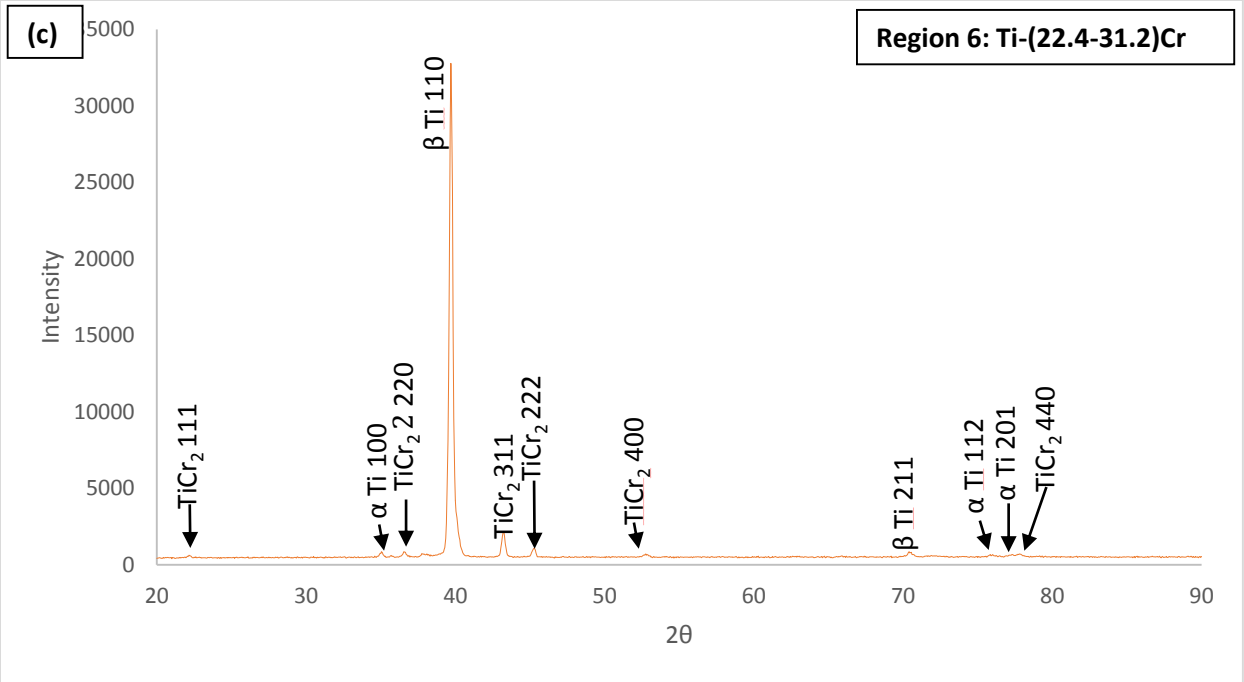

Fig 5.7: XRD scans of Higher Cr wt% Regions (a) Ti-(22.9-29.2)Cr, (b) Ti-(20.9-22.4)Cr, (c) Ti-(22.4-31.2)Cr

Fig 5.7 shows XRD scans on hyper eutectoid regions with higher Cr wt% regions. Fig. 5.7 (a), (b) and (c) show the presence of α phase, $TiCr_2$ phase and β phase. The $TiCr_2$ phase was indexed to C15 Laves phase. The XRD scans at these regions, unlike the "as deposited" alloy, show the coexistence of all three phases α, β and $TiCr_2$ with more presence of the α phase. This has led to a conclusion that α phase precipitates during the slow cooling initially followed by sluggish intermetallic $TiCr_2$ phase formation which in turns begins to deplete the α phase. Region 5: Ti-(22.9-29.2)Cr (lower layer) and Region 6: Ti-(22.4-31.2)Cr (upper layer) have similar composition and crystal structures unlike the "as deposited" alloy where different phases were observed. Heat treatment followed by slow cooling is responsible for the homogenous distribution of phases where as for the "as deposited" alloy selective undercooling due to LENS processing is responsible for uneven phase distribution.

Fig 5.8 XRD scans summarize the phase changes along the length of the graded sample. The lattice parameters of β and $TiCr_2$ phases versus the lattice parameters calculated theoretically based on Vegard's Law at different regions are listed in table 5.3.

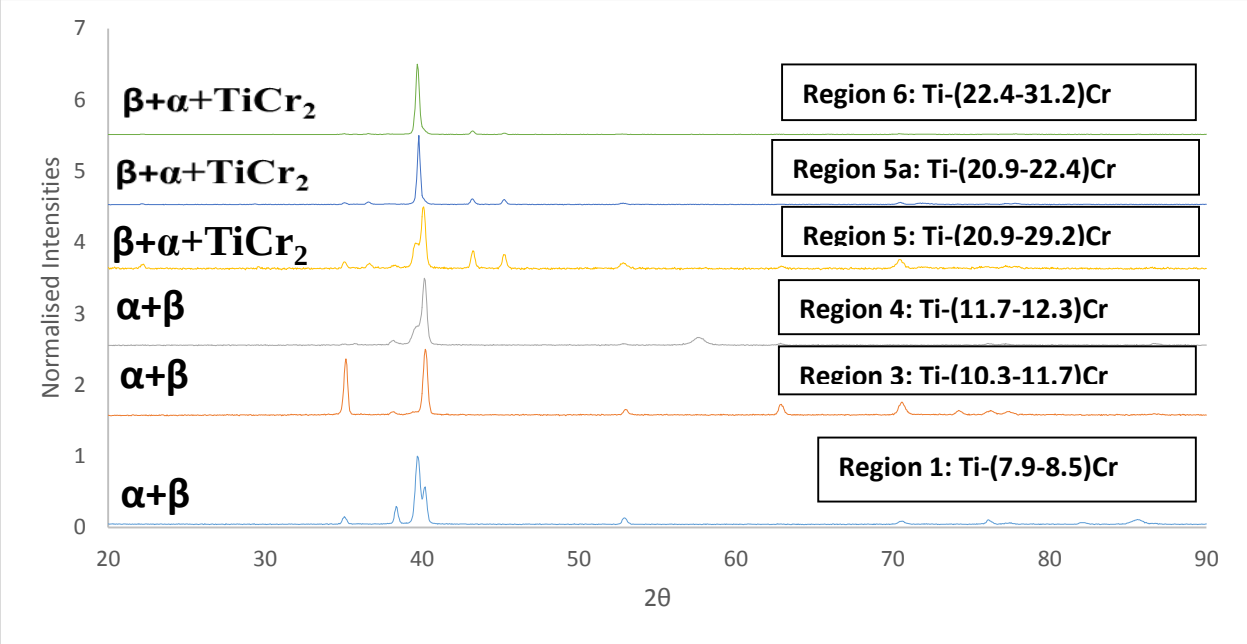

Fig 5.8: XRD scan summary along the regions of the graded alloy

Region	Composition	Calculated lattice constant (a) in Å		PDF lattice constant (a) in Å (Vegards law)	
		β phase	$TiCr_2$ phase	β phase	$TiCr_2$ phase
1	Ti-(7.9-8.5)Cr	3.23	-	3.22	-
3	Ti-(10.3-11.7)Cr	3.27	-	3.26	-
4	Ti-(11.7-12.3)Cr	3.21	-	3.20	-
5	Ti-(20.9-29.2)Cr	3.26	6.94	3.25	6.94
5a	Ti-(20.9-22.4)Cr	3.27	6.94	3.27	6.94
6	Ti-(22.4-31.2)Cr	3.27	6.95	3.27	6.94

Table 5.2: Lattice Parameters of β and $TiCr_2$ Phases along the graded regions.

In summary, from Region 1: Ti-(7.9-8.5)Cr to Region 4: Ti-(11.7-12.3)Cr there is an increase in the β phase with respect to α phase. Region 5: Ti-(20.9-29.2)Cr to Region 6: Ti-(22.4-31.2)Cr shows the presence of $TiCr_2$, α and β phase. These conclusions of the indexed phase agree with those observed in the SEM BSE images.

5.4 Electron Backscatter Diffraction (EBSD)

EBSD is carried out to identify phase fractions and grain crystallographic orientations of α, β and $TiCr_2$ phases along the graded alloy. The EBSD scans provided a clearer understanding of the microstructural evolution when correlated to the XRD scans and SEM images.

The crystallographic phases and orientations of the region of the furnace cooled alloy scanned is Region 5 with compositions near Ti-24.1Cr. Two scans, one at 300 microns scale bar and 25 microns scale bar are carried out in order to obtain a clear picture on the microstructural behavior of the alloy.

5.4.1 Region 5: Ti-24.1Cr (low magnification scan)

The first EBSD scan in Region 5 was acquired at 900x900 microns area with a conference index (CI) of 0.39. Fig 5.9 (a) shows the SEM SE image of the area scanned. Fig 5.9 (b) provides the different crystallographic orientation of the phases in different colors, known as an inverse pole figure (IPF) map. Fig. 5.9 (c) indicates the stereographic triangle (ST) and direction of orientation for cubic β, cubic $TiCr_2$ and hexagonal α, while Figs. 5.9 (d) and (e) indicate the phase fraction and color code, respectively, of the α β and $TiCr_2$ phase map. Fig 5.10 (a)-(e) represents magnification from 200 microns scale

to 20 microns scale of the region scanned for EBSD. A 20 microns scale bar image in Fig 5.10 (e) clearly depicts the coexistence of α-Ti, β-Ti and $TiCr_2$ phases.

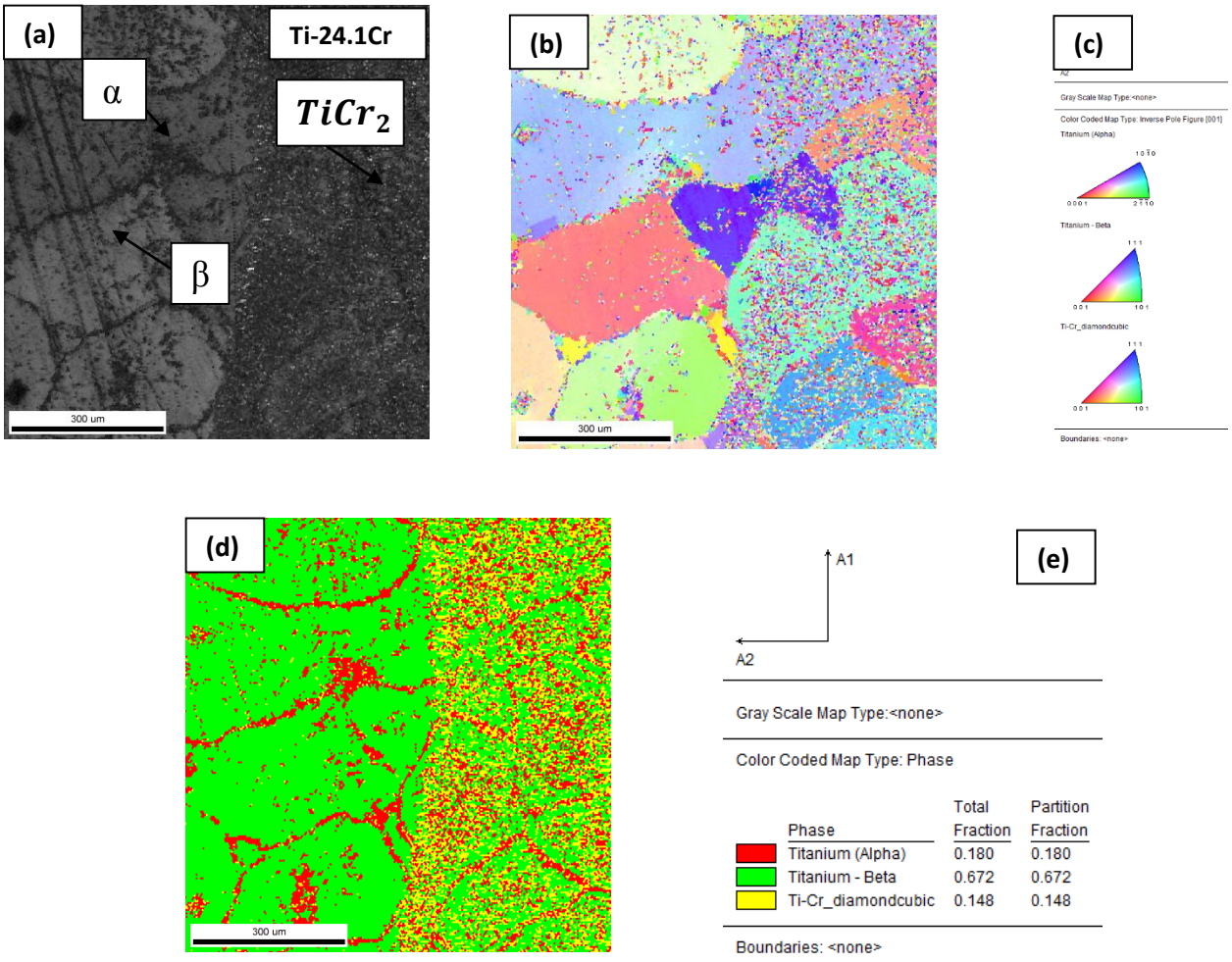

Fig 5.9: Low magnification SEM-EBSD of Region 5 (a) SE image, (b) IPF, (c) ST, (d) Phase fraction map, (e) Color code of phases in map

The total phase fraction from the phase map was determined to be 0.672, 0.180 and 0.148 for β-Ti, α-Ti and $TiCr_2$ intermetallic, respectively. The results agree with BSE images and XRD results shown previously. In order to determine the orientation of the α-Ti, β-Ti and $TiCr_2$ phases of Region 5, a separate study on three phases was done individually as detailed below.

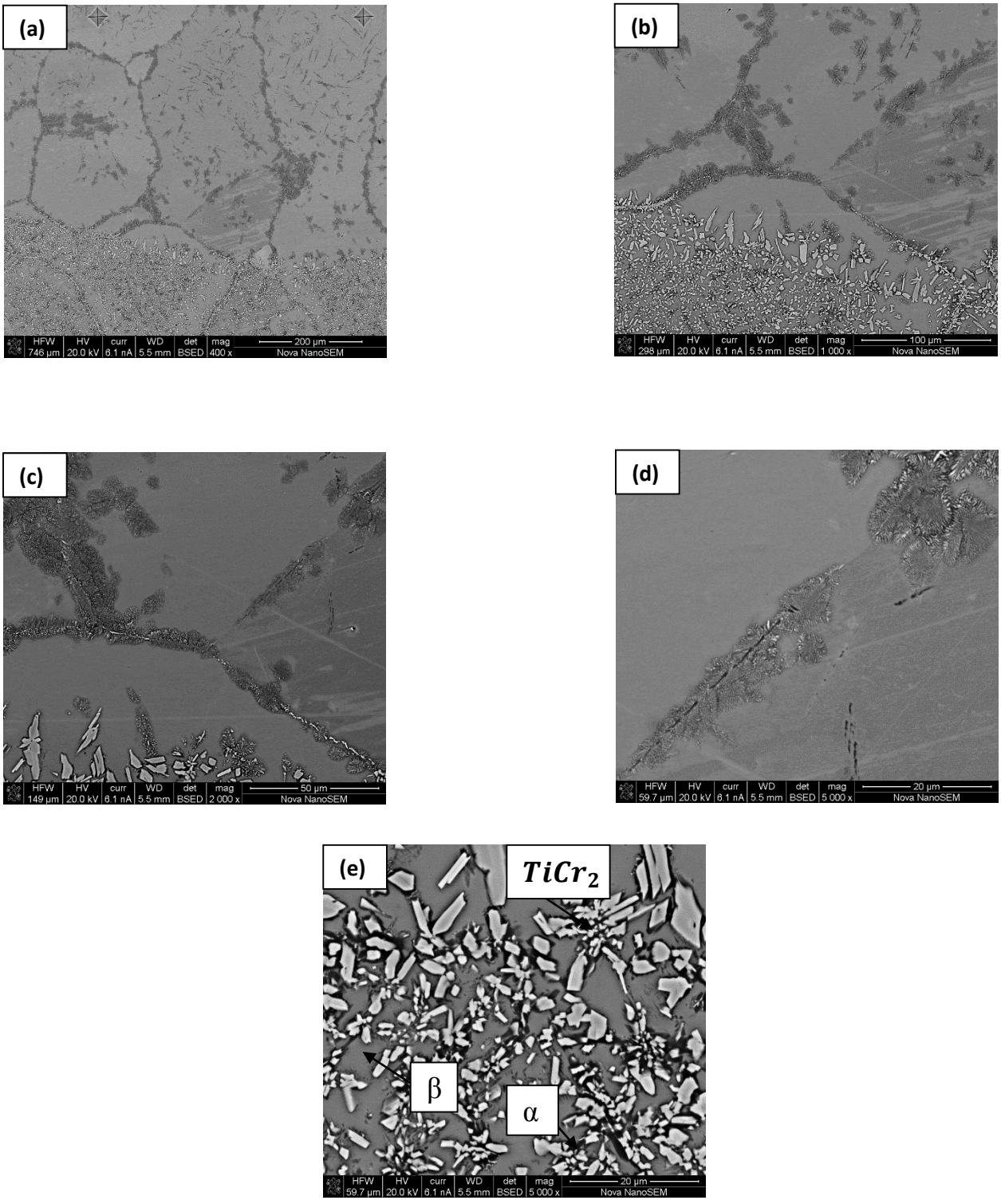

Fig 5.10: BSE images of Region 5 where EBSD scans were conducted

5.4.1.1 α-Ti phase

The IPF, ST, and pole figure (PF) configuration are shown in Fig 5.11: (a), (b), and (c), respectively, for the α-Ti phase.

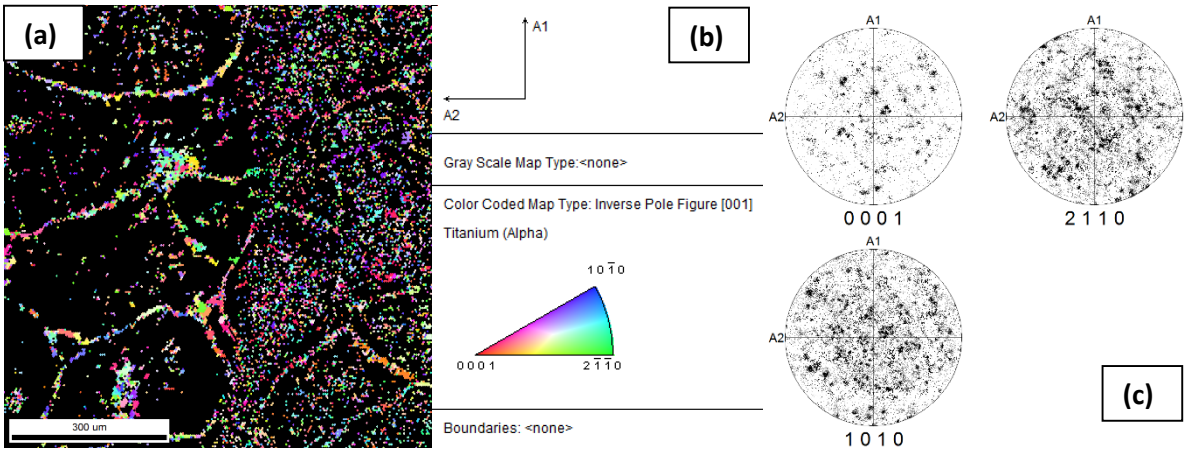

Fig 5.11: α-Ti Phase (a) IPF, (b) ST, and (c) PF.

It is clearly evident that α-Ti phase is randomly oriented suggesting that there is no crystallographic texturing of grains during processing and heat treatment.

5.4.1.2 β-Ti phase

The IPF, ST, and Pole figure configuration are shown in Fig 5.12: (a), (b), and (c), respectively, for the β-Ti phase. From the scan it is evident that the grain size of β-Ti phase is relatively large with no crystallographic preferred orientation. Therefore, as in the α-Ti phase above, there is no texturing due to processing and subsequent heat treatment.

Also, lack of mechanical deformation is responsible for lack of grain orientation and larger grain size.

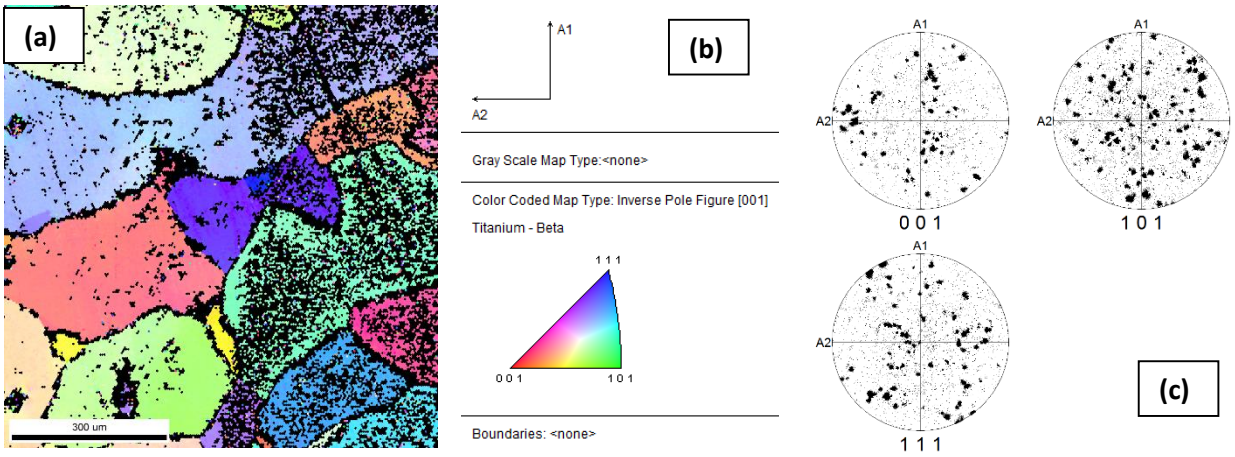

Figure 5.12: β-Ti Phase (a) IPF, (b) ST, and (c) PF

5.4.1.3 $TiCr_2$ Phase

The IPF, ST, and Pole figure configuration is as shown in Fig 5.13: (a), (b), and (c) respectively.

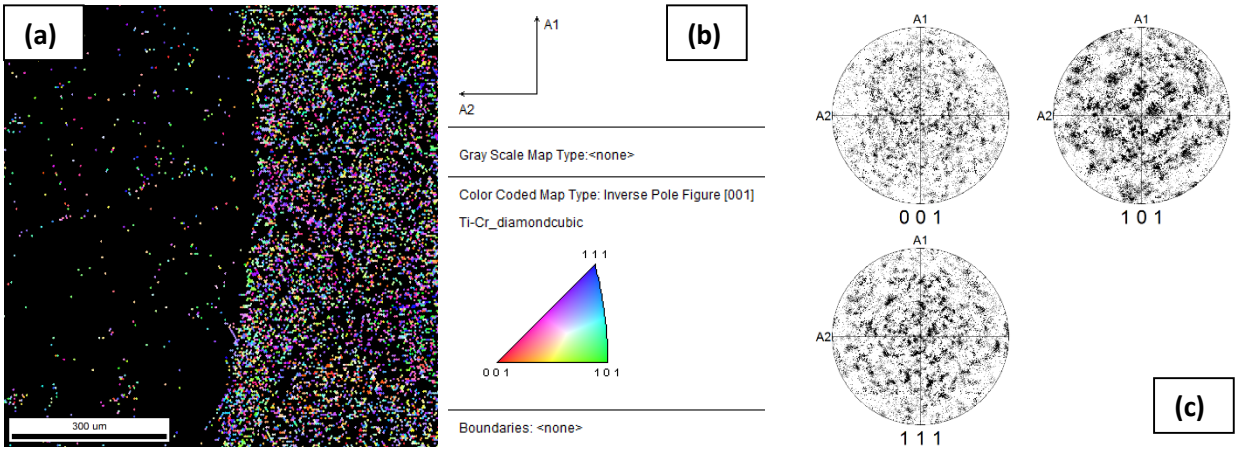

Fig 5.13: $TiCr_2$ Phase (a) IPF, (b) ST, (c) PF

As in the other phases, $TiCr_2$ exhibits no texturing. The formation of an intermetallic phase being a sluggish reaction is responsible for the low phase fraction of 0.148. Unlike

the scans from “as deposited” sample, the intermetallic phase has nucleated throughout the β phase and not just at the grain boundaries.

5.4.2 Region 5: Ti-24.1Cr (high magnification scan)

The second EBSD scan in Region 5 was acquired at 75x75 microns area with a conference index (CI) of 0.17.

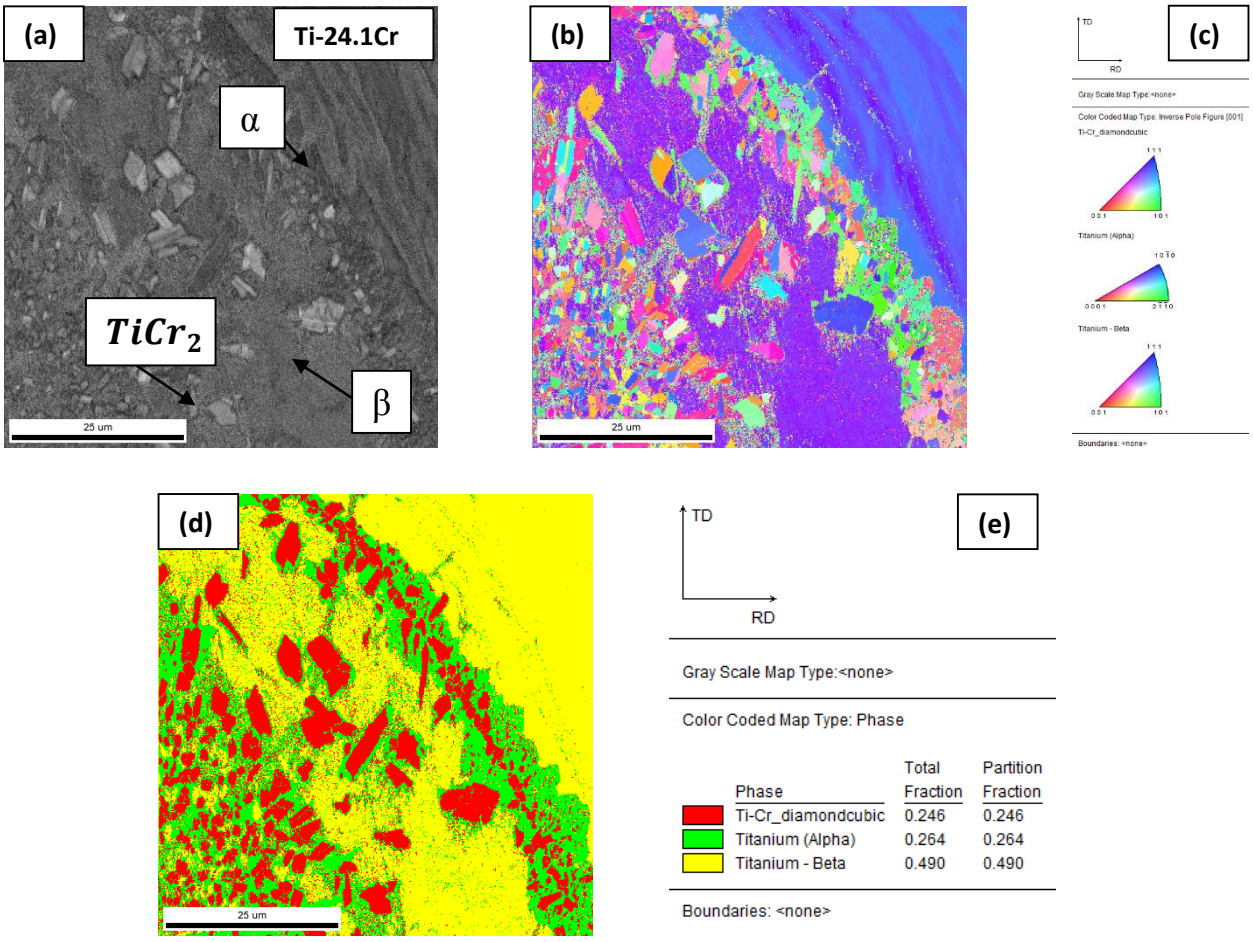

Fig 5.14: High magnification SEM-EBSD of Region 5 (a) SE image, (b) IPF, (c) ST, (d) Phase fraction map, (e) Color code of phases in map

Fig 5.14 (a) shows the SEM SE image of the area scanned. Fig 5.14 (b) provides the different crystallographic orientation of the phases in different colors, known as an

inverse pole figure (IPF) map. Fig. 5.14 (c) indicates the stereographic triangle (ST) and direction of orientation for cubic β, cubic $TiCr_2$ and hexagonal α, while Figs. 5.14 (d) and (e) indicate the phase fraction and color code, respectively, of the α, β, and $TiCr_2$ phase map.

The total phase fraction from this phase map was determined to be 0.490, 0.264 and 0.246 for β-Ti, α-Ti and $TiCr_2$, respectively. The results are in agreement with BSE images and XRD results shown previously. In order to determine the orientation of the α-Ti, β-Ti and $TiCr_2$ phases of Region 5, a separate study on three phases was done individually as detailed below. A high magnification EBSD is done to ensure $TiCr_2$ phase is surround by depleted α-Ti phase within the β-Ti matrix, since from the map it is evident that the $TiCr_2$ phase is surrounded by α-Ti

5.4.2.1 α-Ti phase

The IPF, ST, and pole figure (PF) configuration are shown in Fig 5.15: (a), (b), and (c), respectively. It is clearly evident that α-Ti phase is randomly oriented with a phase fraction of 0.264 which is similar to $TiCr_2$ phase fraction.

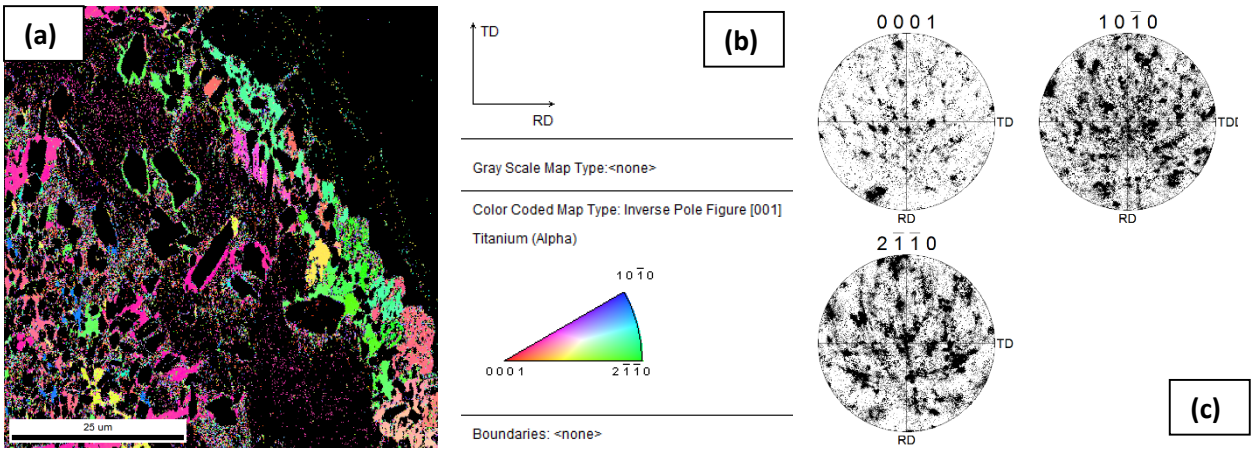

Fig 5.15: α-Ti Phase (a) IPF, (b) ST, and (c) PF.

Fig 5.15 (c) provides the pole figure information of α-Ti at (0001), (2-1-10) and (10-10) poles. The Pole figure indicate that the grains in the α phase are randomly orientated.

5.4.2.2 β-Ti phase

The IPF and ST are shown in Figs. 5.16 (a) and (b), respectively, for the β-Ti phase. The region under scan only encompasses two grain so the β-Ti grain orientation cannot be determined.

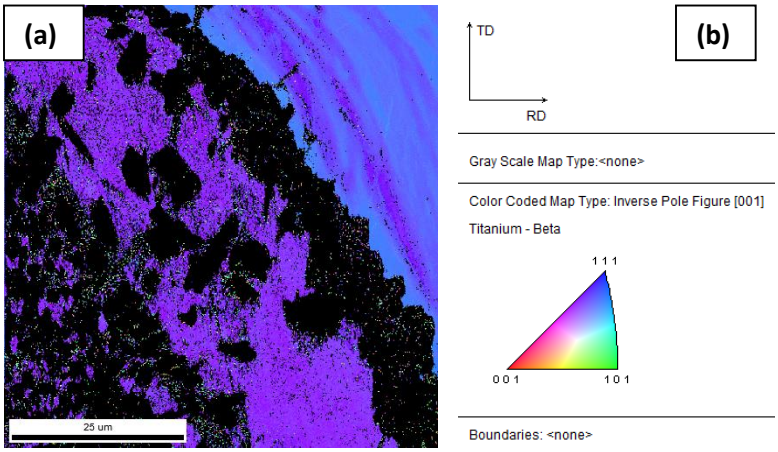

Figure 5.16: β-Ti Phase (a) IPF, and (b) ST

5.4.2.3 $TiCr_2$ Phase

Similar to the other phases, $TiCr_2$ is randomly oriented. The phase fraction of the $TiCr_2$ phase has been determined to be 0.246. The formation of an intermetallic phase being a sluggish reaction is responsible for the low phase fraction. It is evident that the volume fraction of $TiCr_2$ increases with the depletion of α-Ti phase.

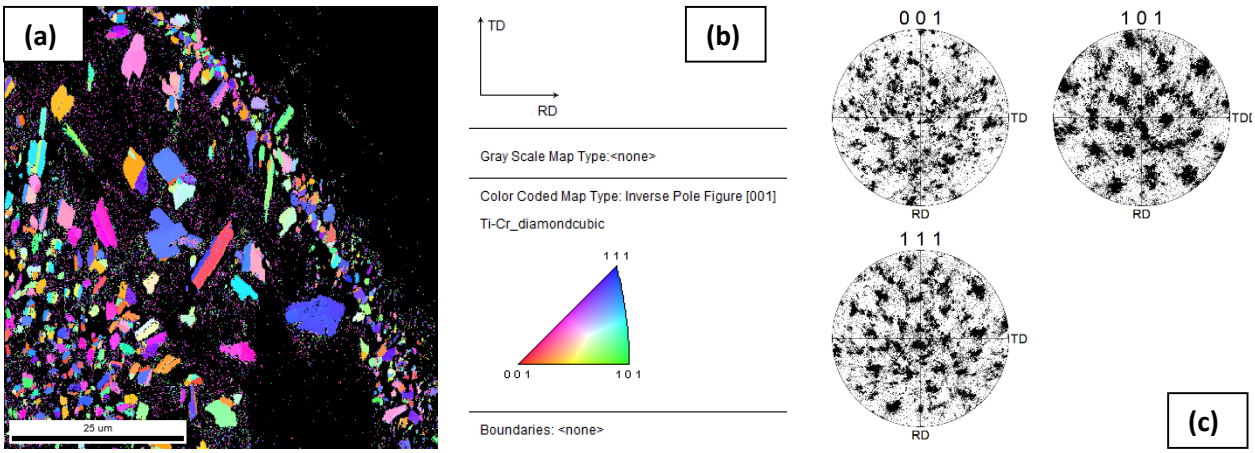

Fig 5.17: $TiCr_2$ Phase (a) IPF, (b) ST, (c) PF.

The IPF, ST, and Pole figure configuration is as shown in Fig 5.17: (a), (b), and (c), respectively indicate that there is no texturing with this phase.

5.5 Energy Dispersive Spectroscopy (EDS) maps

EDS mapping has been carried out on a 20 and 30 micron scale at the same region where EBSD scan was conducted above. Scan 1: Ti-23Cr shown in Fig 5.18 (a)-(c) has been carried out where formation of $TiCr_2$ intermetallic phase is less dominant. Fig 5.18 (a) is the BSE image of area scanned while Fig 5.18 (b) and (c) show the elemental mapping of Ti K and Cr K regions, respectively.

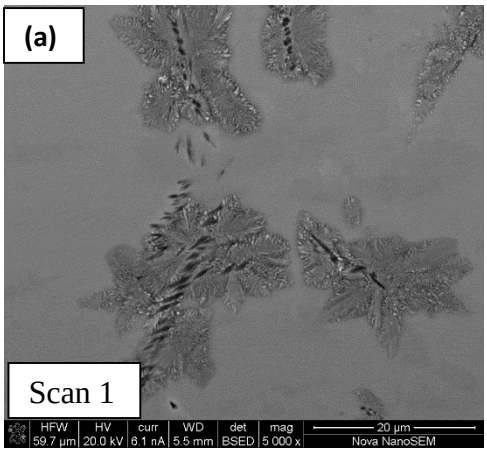

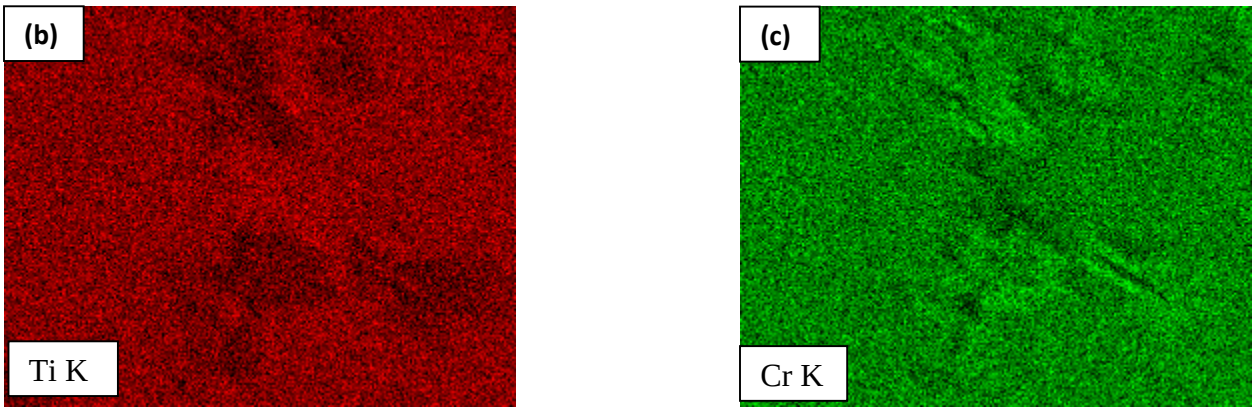

Fig 5.18: EDS map Scan 1: Ti-23Cr (a) BSE image, (b) Ti K map, and (c) Cr K map.

Scan 2: Ti-27.6Cr shown in Fig 5.19: (a) - (c) has been carried out at a grain boundary with extensive $TiCr_2$ phase formation. Both Scan 1 and Scan 2 prove that Ti and Cr are mixed homogeneously throughout the regions, however Ti K map in both scans provide a more dense coloration when compared to Cr mapping indicating that the Ti content at the region is greater than Cr. At the surface of the $TiCr_2$ intermetallic phase, the coloration of Ti is minimal in comparison to Cr indicating a higher presence of Cr. This can be linked to the structural formula of $TiCr_2$ where 1 Ti atom bonds with 2 Cr atoms, creating a greater presence of Cr at the intermetallic surface in comparison to Ti. A similar result has been obtained on an EDS line scan carried out during TEM analysis (presented below).

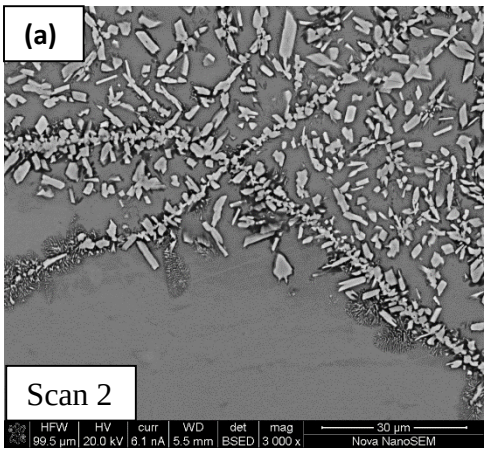

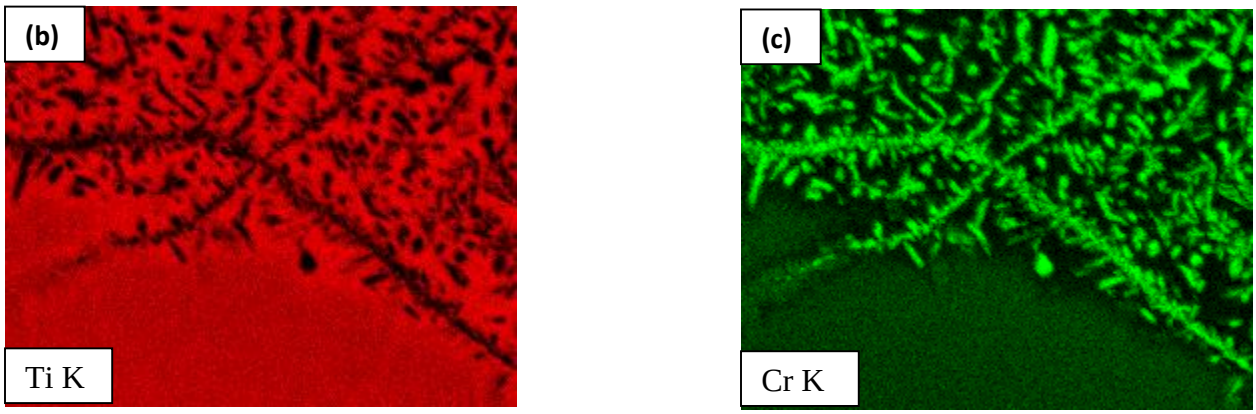

Fig 5.19: EDS map Scan 2: Ti-27.1Cr (a) BSE image, (b) Ti K map, and (c) Cr k map.

5.6 FIB Lift-Out

A FIB lift-out is carried out at Region 5a: Ti-22.4Cr. The area chosen as region of interest to be studied by TEM analysis is due to the presence of three phases (α, β and $TiCr_2$).

TEM analysis at this region also helps in determining the C15 Laves phase orientation of $TiCr_2$ intermetallic, and depletion of the α phase due to $TiCr_2$ intermetallic phase nucleation. Fig 5.20 (a)-(d) indicate the various stages of lift-out and sample polishing using FIB.

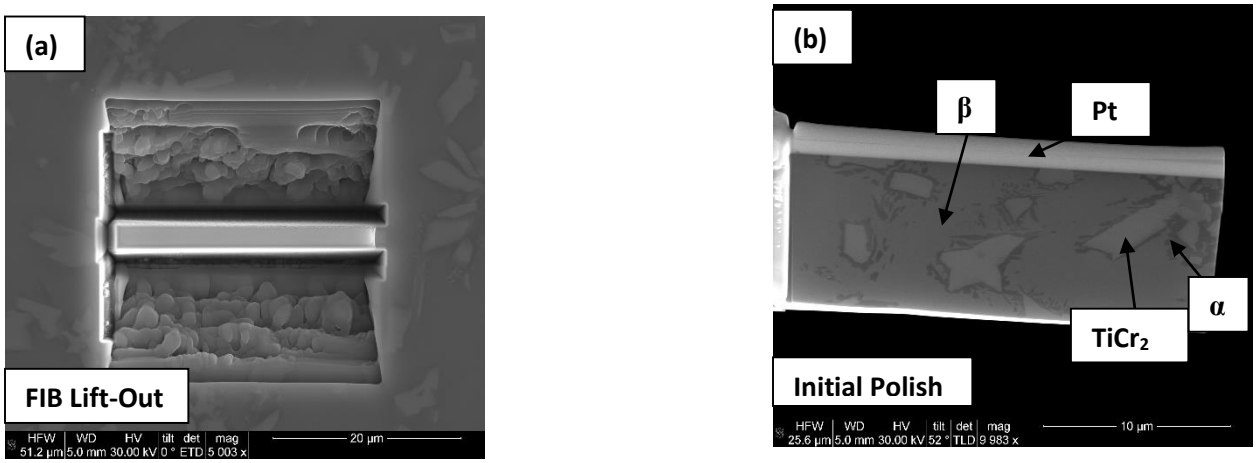

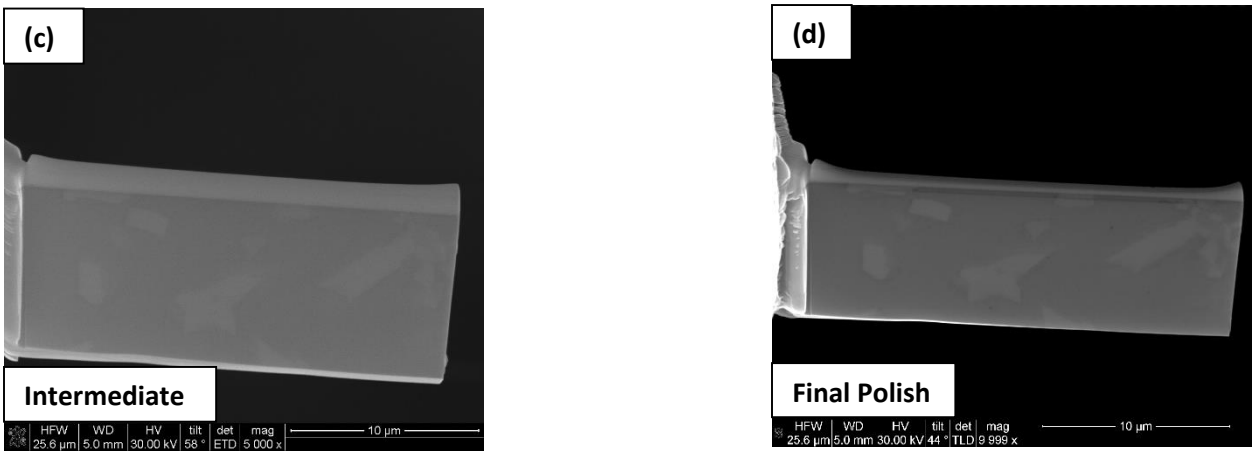

Fig 5.20: SEM images of (a) FIB Lift-out (b) Initial Polish, (b) Intermediate Polish, and (c) Final Polish

5.7 Transmission Electron Microscopy (TEM) and Micro-diffraction Studies

Electron diffraction patterns along with Bright field TEM images of Ti~21Cr from Region 5a of the sample indicate the presence of α, β and $TiCr_2$ intermetallic phases. Fig 5.21 (a) shows the overall microstructure of the region while Fig 5.21 (b) shows a higher magnification of the three phases. Fig 5.21(c), (d) and (e) are selected area diffraction patterns of $TiCr_2$ indexed at [011], [111] and [112] zone axes, respectively. The SAD pattern viewed from TEM imaging for the selected area of diffraction is done along axis indicated in Fig 5.21 (c) - (d) clearly indicates that the $TiCr_2$ intermetallic is the C15 Laves phase with Fd-3m symmetry, an FCC lattice.

In order to identify the concentration of elements present at each phase, an EDS line scan in the TEM from β to α to $TiCr_2$ intermetallic phase was performed. The area scanned along with their respective element compositions are shown in Fig 5.22: (a), (b) and Fig 5.23 (a) - (c).

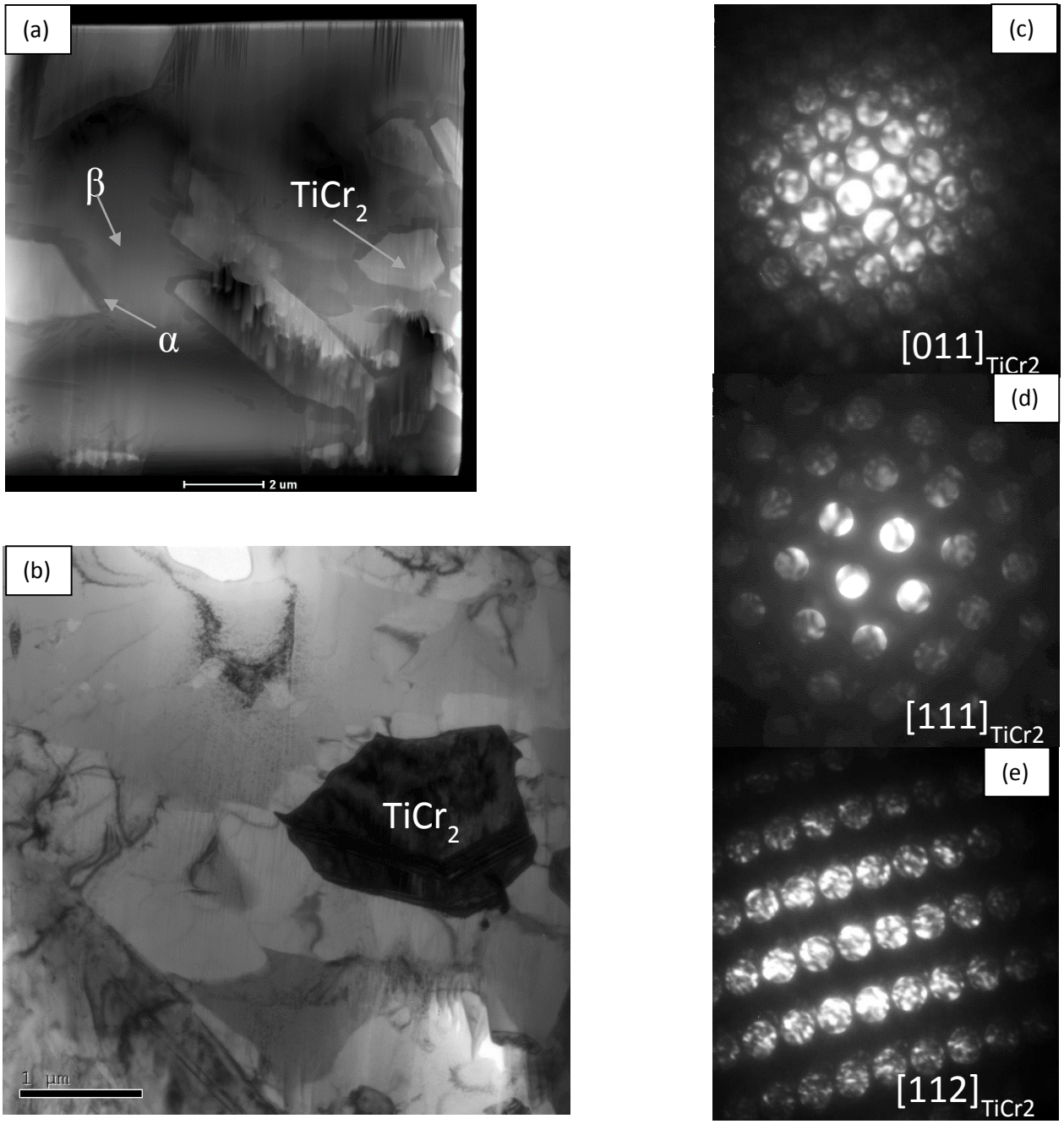

Fig 5.21: TEM-SAD analysis of Region 5 showing (a) BFTEM low magnification image, (b) high magnification BFTEM image of $TiCr_2$, and SAD pattern of $TiCr_2$ along (c) [011], (d) [111], and (e) [112] zone axes.

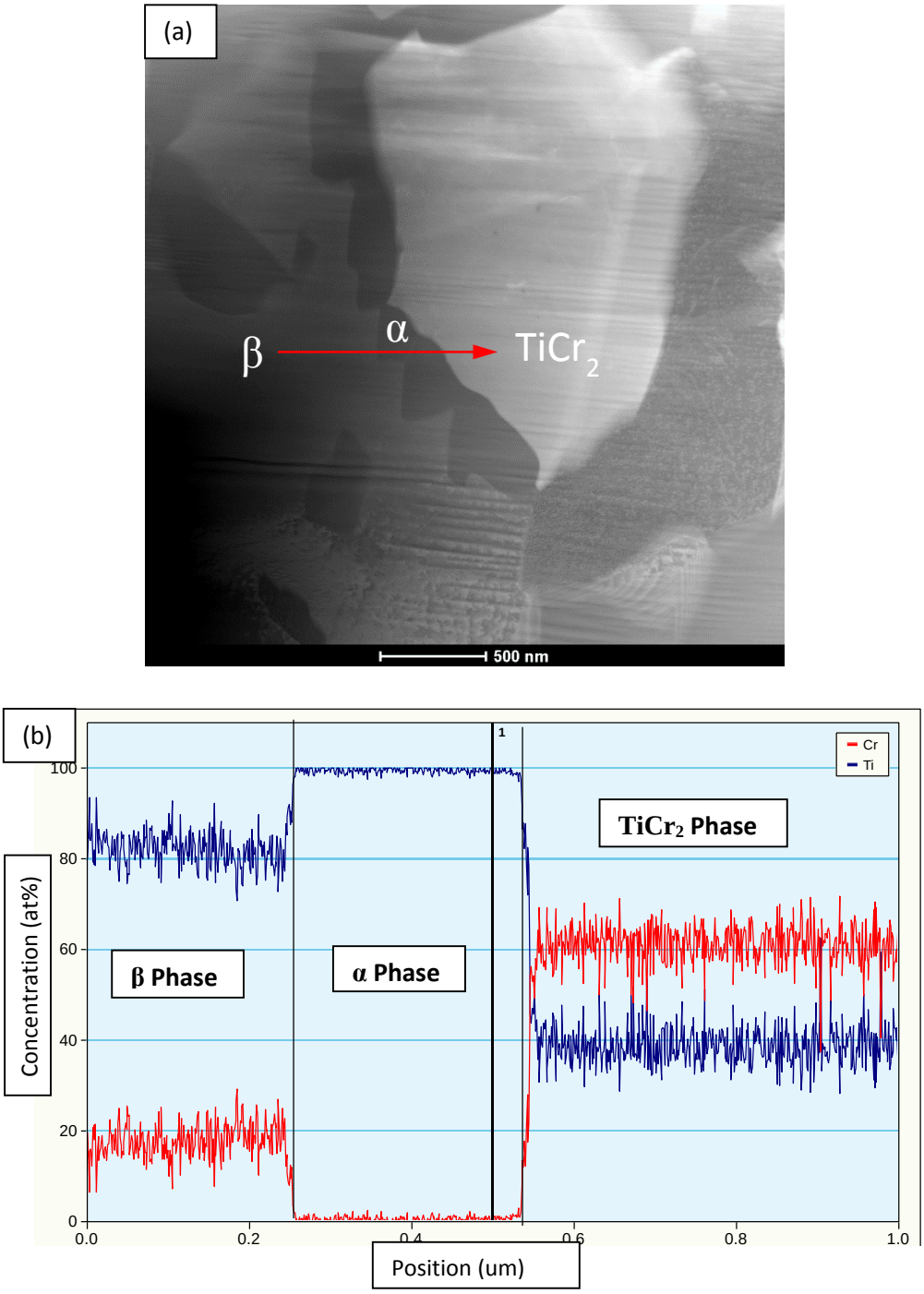

Fig 5.22: (a) STEM=ADF image and (b) EDS line scan of Region 5.

The EDS line scan shows β phase to be a mix of Ti and Cr with at% of Ti with respect to Cr. The α phase is shown to be only Ti, while the $TiCr_2$ intermetallic is

predominantly occupied by Cr with small amounts of Ti although not in a 2:1 ratio of 67:33 atomic % but 60:40 atomic %. These results are in agreement with EDS maps in Fig 5.18, 5.19.

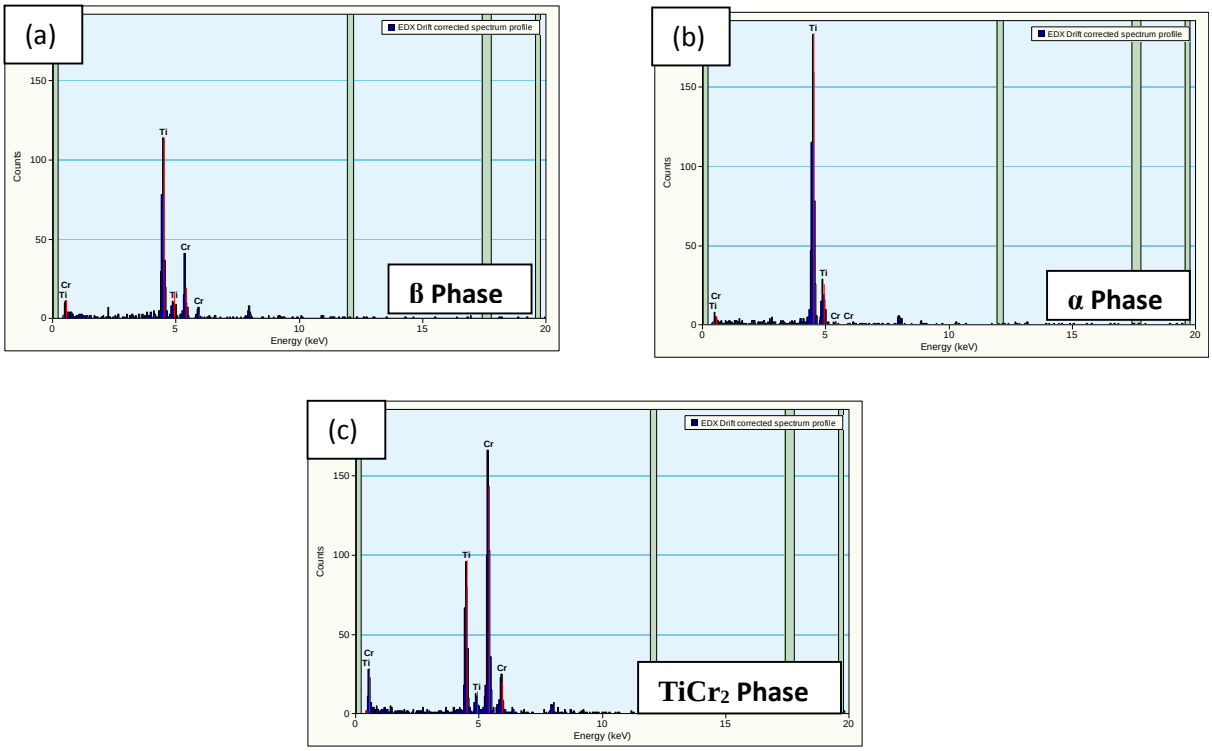

Fig 5.23: EDS line scan of (a) α phase, (b) β phase and (c) $TiCr_2$ phase

5.8 Micro-Hardness

Due to the microstructural phase evolution from Ti-10Cr to Ti-30Cr compositional range, there is a gradual change in micro-hardness, Vickers hardness measurements were made along the sample gradient with a spacing of 0.5 mm between indents with three measurements at each location or layer. The hardness values with respect to concentration of Chromium and distance along the gradient is shown in Fig 5.24(a) and (b), respectively.

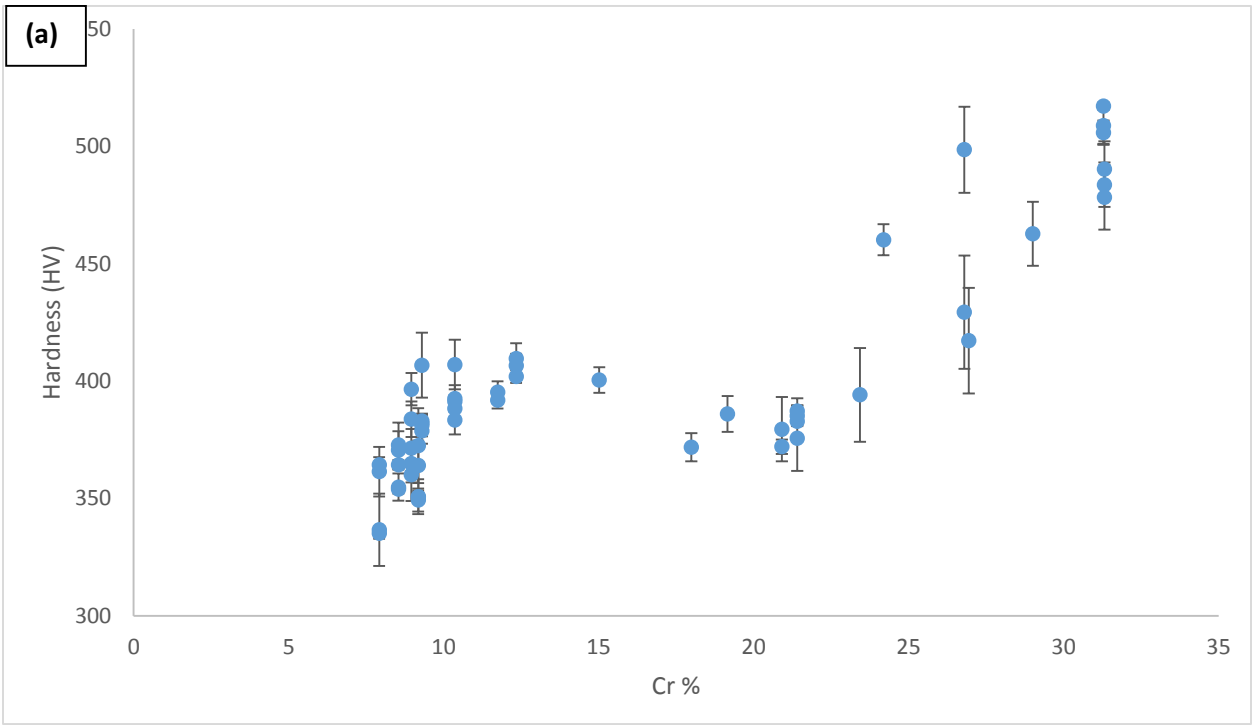

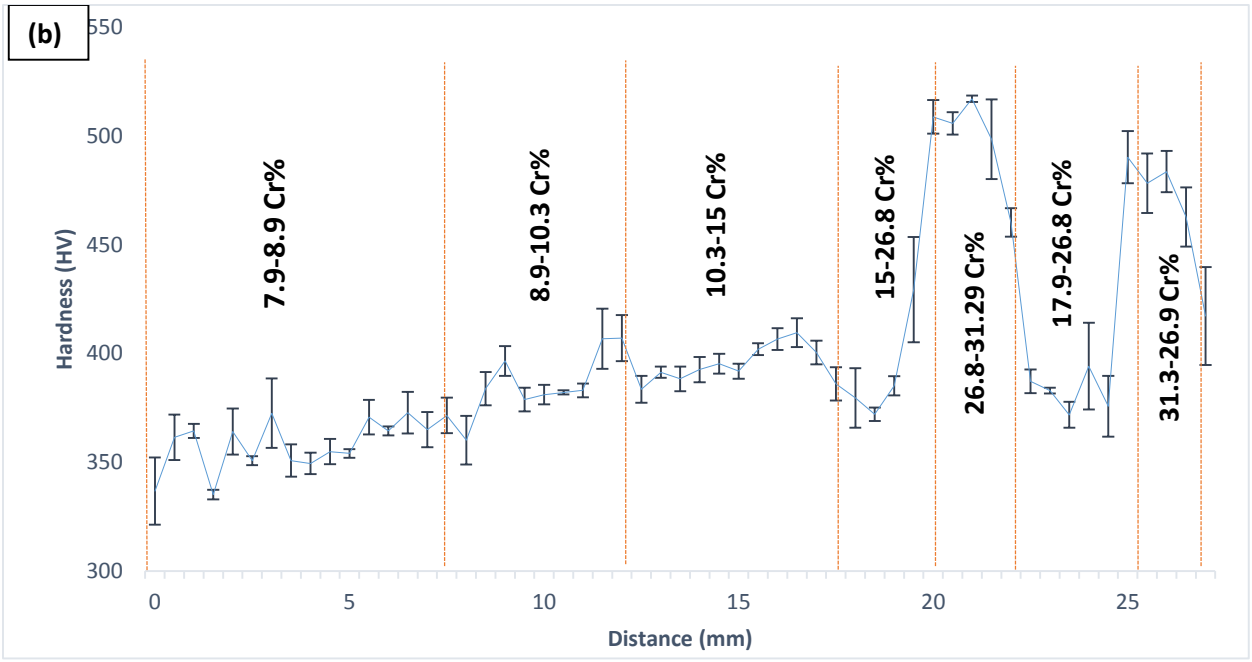

Fig 5.24: Vickers micro-hardness values as a function of (a) Cr wt% and (b) distance along the graded sample

The hardness of the heat treated sample at hyper eutectoid regions of high Cr wt% of Ti-(25-30)Cr has been determined to be around 500 HV. The hardness at the high Cr wt% region has been found to be higher than the “as deposited” alloy discussed in chapter 4.. The presence of three phase region of α, β and $TiCr_2$ is deemed responsible for the increase in hardness of the heat treated alloy. Unlike the “as deposited” alloy, the furnace cooled sample has undergone homogenous heat treatment and slow cooling. This facilitates the homogeneous nucleation of phases with a greater volume fraction, preventing two different readings of hardness at around 30 wt% Cr as seen in “as deposited” sample discussed in chapter 4.

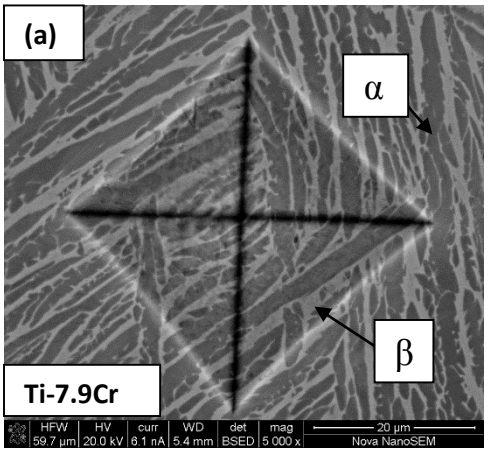

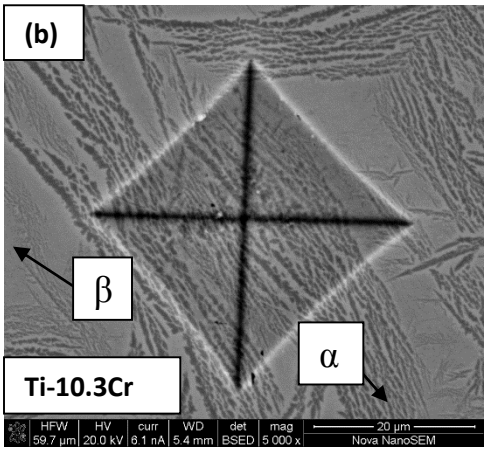

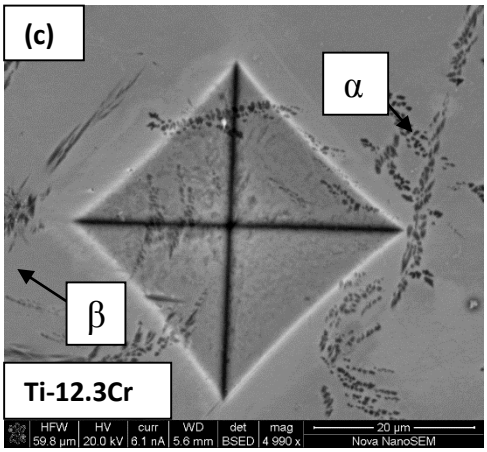

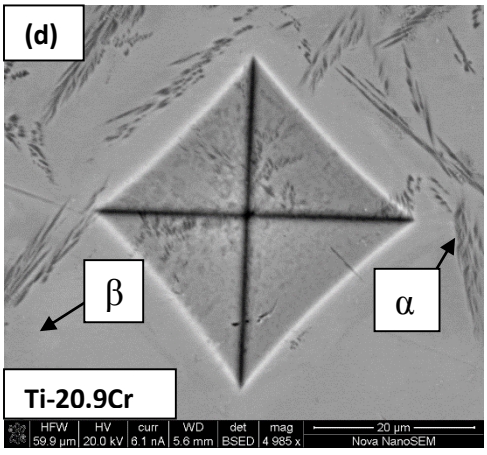

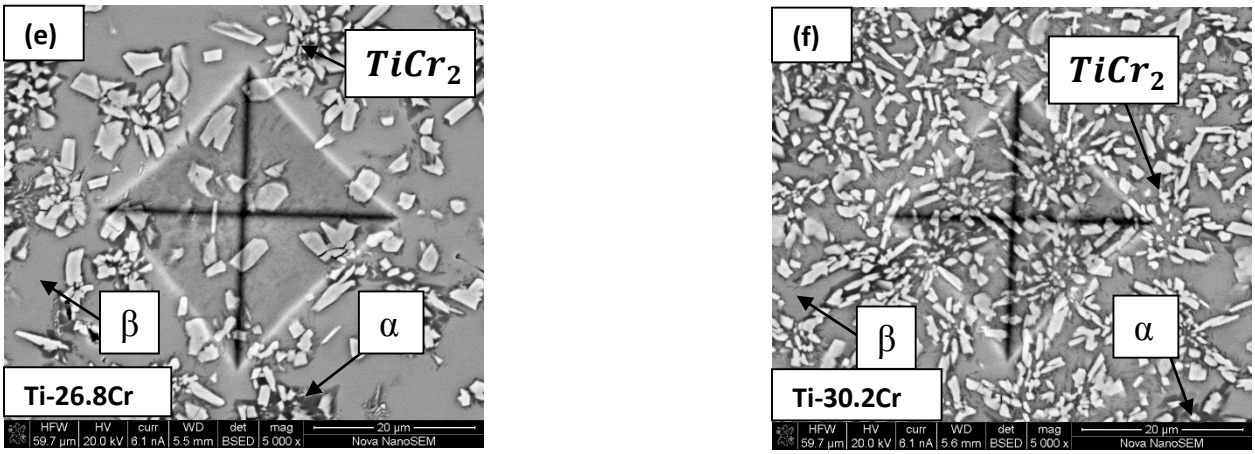

Fig 5.25: SEM images of Vickers indents for compositions of (a) Ti-7.9Cr, (b) Ti-10.3Cr, (c) Ti-12.3Cr, (d) Ti-20.9Cr, (e) Ti-26.8Cr, and (f) Ti-30.2Cr.

From Fig 5.25 (a)-(f), it is evident that the size of the Vickers hardness indentation decreases with increase in Cr wt%. In addition, while hardness increases with increasing Cr content due to TiCr2 phase formation, there is no evidence of shear bands propagating along corners of the indents shown in Fig. 5.25. Therefore, the heat treated alloy maintains an increase in hardness without compromising its toughness.

In summary, the heat treated and furnace cooled LENS^{TM} Ti-10Cr to Ti-30Cr compositionally graded alloy was characterized by SEM BSE imaging, EDS, XRD, EBSD, TEM-SAD in selected region, and micro-hardness measurements to determine processing-structure-property relations. The α-Ti, β-Ti, and $TiCr_2$ phases were identified in varying phase fractions which was influential in determining the hardness values. Slow cooling from elevated temperature enables diffusion based phase transformation. Nucleation of α phase throughout the sample and larger phase fraction of $TiCr_2$ in comparison to “as deposited” and “air cooled” sample is observed which increases the hardness without evidence of brittle fracture.

Chapter 6

INFLUENCE OF Cr CONCENTRATION ON MICROSTRUCTURAL PHASE EVOLUTION AND ITS EFFECT ON HARDNESS IN HEAT TREATED AND AIR COOLED Ti-xCr ALLOYS

6.1 Introduction

The effect of compositional variation of Cr concentration on heat treated (1000°C for 30 min) and air cooled LENS^{TM} processed Ti-xCr (Ti-xCr: 10≤x≤30wt %) is evaluated and discussed. The binary alloy is assessed, by means of XRD scans, SEM imaging, EBSD scans, TEM analysis on a few select regions, and Micro-Hardness measurements. The results obtained from the heat treated and air cooled alloy experiments are compared to the as-deposited and heat treated and furnace cooled alloys presented in Chapters 4 and 5, respectively.

6.2 Microstructural Evolution Studied by SEM

The microstructural and compositional evolution of air cooled Ti-10Cr to Ti-30Cr graded alloy were studied by BSE imaging and EDS, respectively. Fig. 6.1 shows a schematic of the analysis regions along which BSE imaging and EDS scans were conducted on the graded alloy. Fig 6.2 (a)-(g) and Fig. 6.3 (a)-(f) show representative BSE image comparisons for low and high wt% Cr contents, respectively, along the length of the different regions of the alloy. Fig. 6.4 (a)-(m) summarizes the entire compositional range at a higher BSE image magnification. The images in Figs. 6.2-6.4 have the corresponding Cr wt% values that were determined by EDS acquired along each region

from multiple scans. The compositional changes along the length of the sample are summarized in table 6.1. The height occupied by each region is approximated to be 1.25mm. While there is a trend of increasing Cr content along the length of the alloy, there is some statistical variation in sub-regions. Thus, it is not a uniformly compositionally graded alloy due to the variation in heat transfer during LENS™ processing.

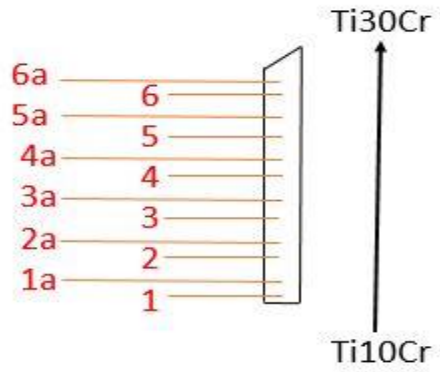

Fig 6.1: Schematic representation of Regions and Sub-regions for acquiring BSE images and EDS scans.

At low Chromium wt% concentration of Region 1: Ti-7.8Cr and Region 1a: Ti-8.5Cr there is the presence of α phase within a β matrix as shown in Fig 6.2 (a) and (b). The α phase has originated from a eutectoid reaction consistent with the Ti-Cr phase diagram. The α phase nucleation may have been facilitated by oxidation of the sample near the edges. Unlike the 'furnace cooled" and "as deposited" alloys, α phase is present only at the above mentioned regions and not throughout the sample. In Region 2: Ti-9.4Cr and Region 3: Ti-9.4Cr, a 100% retained metastable β phase is observed as shown in Fig 6.2 (c) - (e). However XRD scans, TEM analysis and hardness studies, presented later in this chapter, at these regions have suggested a wide spread phase formation of a well-structured ω phase within the β matrix phase. The ω phase cannot be viewed by SEM

imaging, since these phases can only be observed at a scale length of 50-100 nanometers. A sample portion at Region 2: Ti- 9.4Cr was prepared for TEM analysis to be presented later. Although no literature can be found on the composition for initiation of ω phase within the β matrix of Ti-xCr alloys, proof of existence at low Cr wt% has been seen by Peyman et al (41), Narayanan et al (32), and Hihong et al (42).

From composition of Region 4: Ti-11.0Cr and Region 4a: Ti-19.4Cr, a 100% retained β phase has been confirmed by SEM, shown in Fig. 6.2 and 6.3 which were also observed by WelschG et al (16), Luhman T et al (37). It is interesting to note that general studies have shown 100% β phase retention and ω phase nucleation occurs during quicker cooling via water quenching; however, similar results have been achieved via air cooling in this study.

Kinetics of heat transfer is bound to have played a role in the microstructure of the air cooled sample. The occurrence of ω phase, fully retained β phase, reduced nucleation of $TiCr_2$ intermetallic phase and absence of α phase is due to the undercooling at β-transus temperature followed by quick air cooling. This provides a microstructure completely different from what has been observed in the “as deposited” and “furnace cooled” alloys.

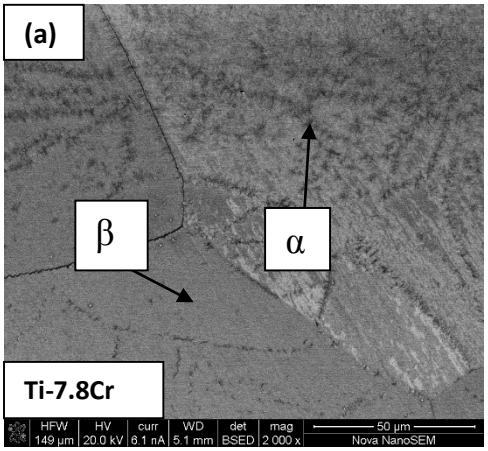

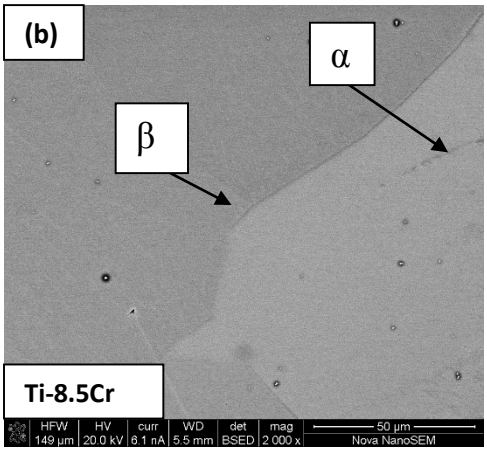

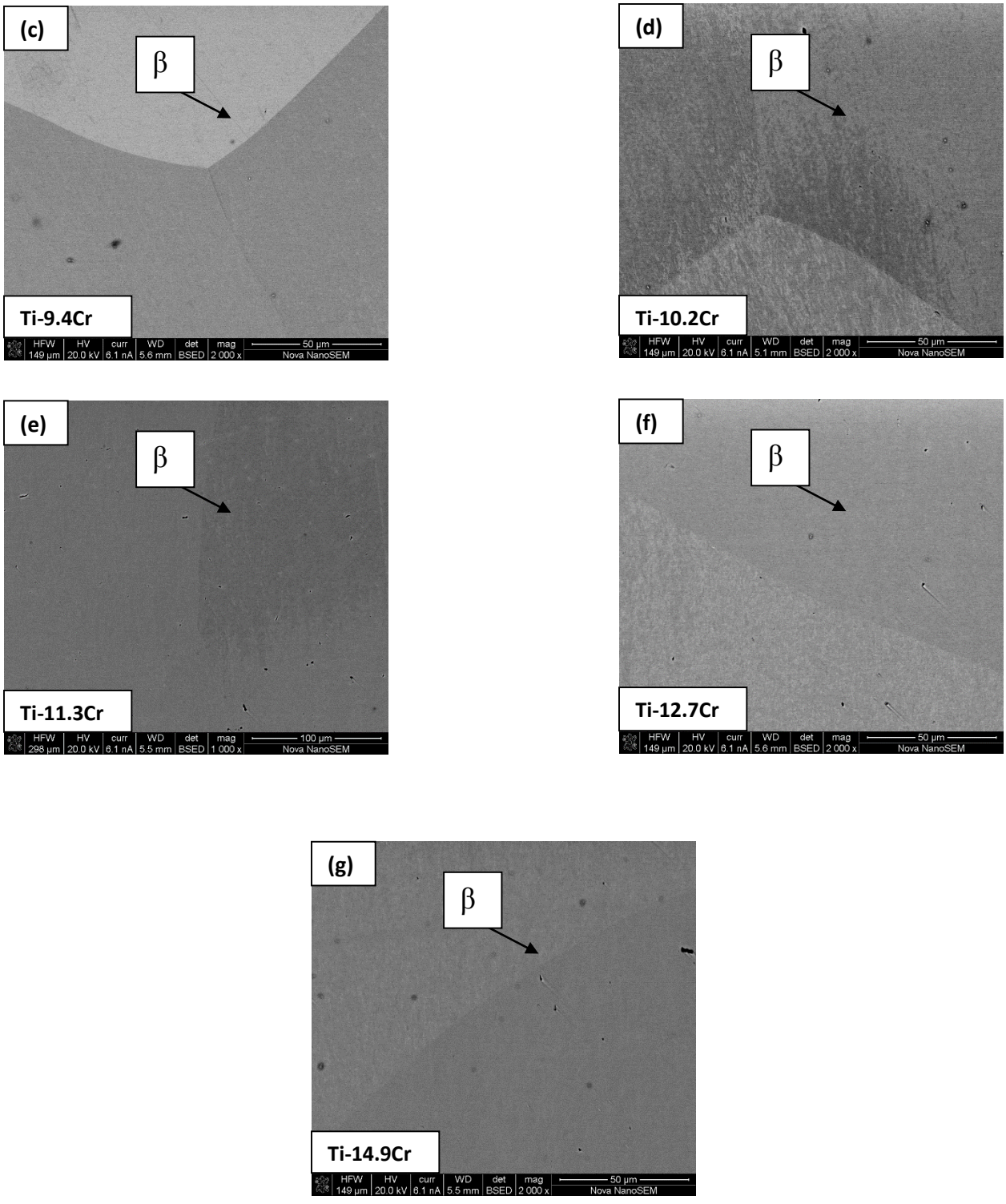

Fig 6.2: (a)-(g) BSE images showing microstructural changes for low Cr (7-15) wt% alloys.

REGION	COMPOSITION (wt%)	REGION	COMPOSITION (wt%)	REGION	COMPOSITION (wt%)
1	Ti-7.8Cr	3	Ti-9.1Cr	5	Ti-21.7Cr
					Ti-24.8Cr
					Ti-27.9Cr
1a	Ti-8.5Cr	3a	Ti-9.4Cr	5a	Ti-32.6Cr
			Ti-10.2Cr		Ti-23.1Cr
					Ti-19.2Cr
2	Ti-9.4Cr	4	Ti-11Cr	6	Ti-19.6Cr
					Ti-30Cr
2a	Ti-9.2Cr	4a	Ti-11.3Cr	Above 6	Ti-31.5Cr
			Ti-12.7Cr		Ti-27.6Cr
			Ti-14.9Cr		
			Ti-19.4Cr		

Table 6.1: EDS determined compositions of various Regions and sub-regions.

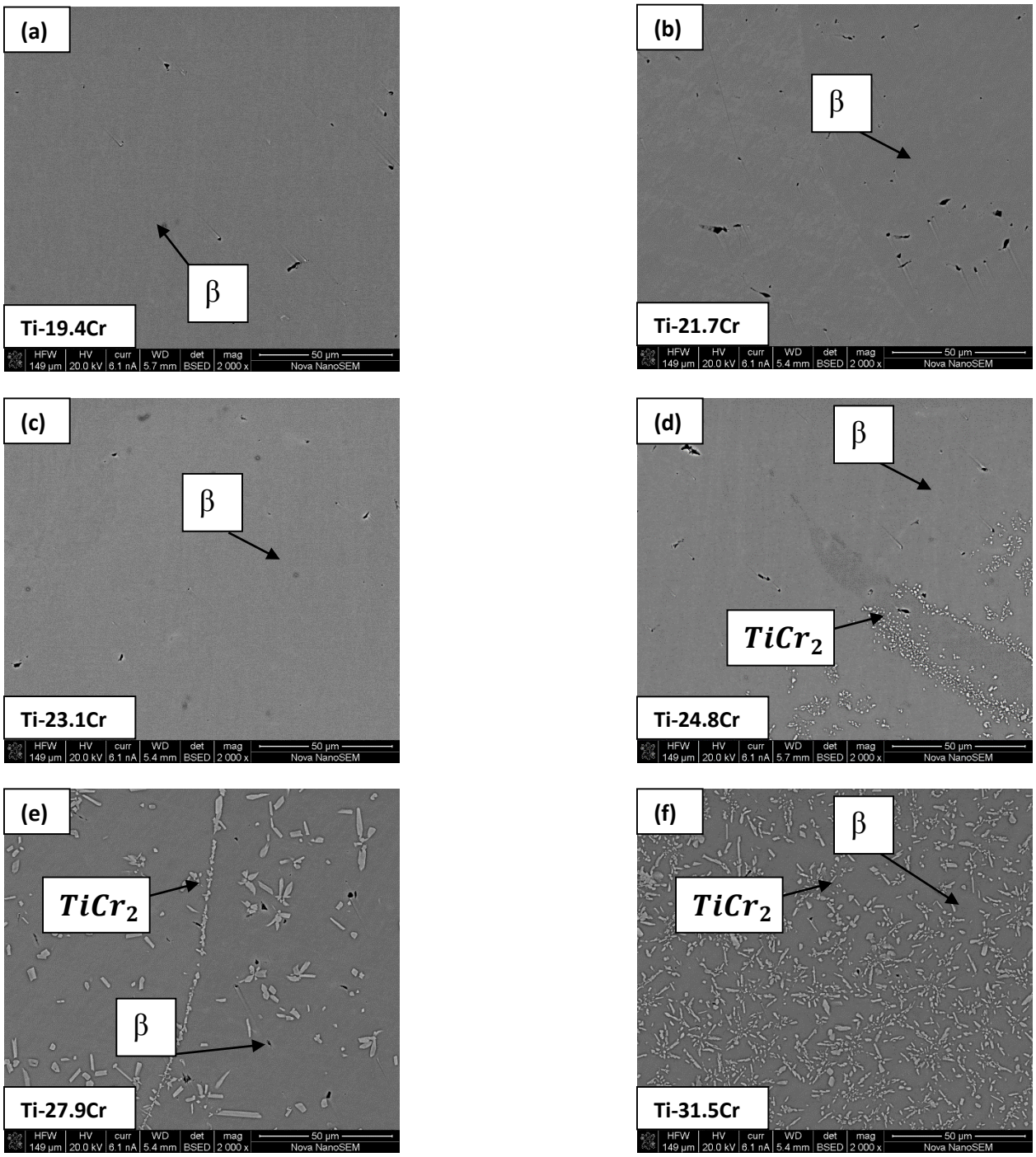

Fig 6.3: (a)-(f) BSE images showing microstructural changes at high Cr (19-31) wt%.

Narayanan et al (32) and Mebed et al (38) have also stated that Ti-Cr alloy system having a spinodal decomposition of the β phase, would prefer β_1 and β_2 metastable phases to transform into β + α or β + ω. At higher composition of Cr wt% from Region 4a:

Ti-19.4Cr and Region 5: Ti-23.1Cr, 100% β phase retention is also observed in the BSE images in Fig. 6.3.

The initial formation of intermetallic $TiCr_2$ (Laves phase C15) occurs at grain boundaries within the β matrix at Ti-24.8Cr, shown in Fig 6.3(d). $TiCr_2$ content continues to increases with increasing Cr content as shown in Fig 6.3(e) and (f). The presence of three phases observed in selective areas of "as deposited' and widely in 'furnace cooled" alloys has not been observed here for air cooled alloy. The kinetics of air cooled sample has prevented the extensive formation of α phase as observed in the other two samples in chapters 4 and 5. Although the formation of $TiCr_2$ intermetallic phase has been recorded as a sluggish reaction, Region 6: Ti-31.2Cr similar in composition with Region 5: Ti-29Cr, shows a dominant presence of $TiCr_2$ phase in both regions, similar to the furnace cooled alloy but dissimilar to the as deposited alloy. The heat treatment followed by air cooling enables Region 5 (lower layer) and Region 6 (upper region) to be undercooled evenly. This facilitates the formation of the sluggish $TiCr_2$ intermetallic phase. The rate of cooling being quite fast has prevented an extensive nucleation of $TiCr_2$ at Cr rich regions of the alloy. The phase fraction of $TiCr_2$ intermetallic in comparison to that observed in furnace cooled sample is quite less. The presence of ω phase at low Cr wt% content, fully retained β phase and $TiCr_2$ phase precipitation has been justified with the help of extensive XRD scans, hardness measurements and TEM imaging discussed in the later sections of this chapter.

A summary of SEM BSE images taken at higher magnification for the entire compositional range along the different regions is shown in Fig 6.4: (a)-(m).

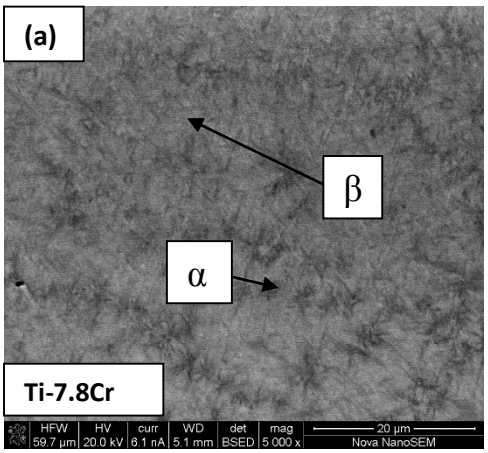
(a)
β
α
Ti-7.8Cr
HFW 59.7 µm | HV 20.0 kV | curr 6.1 nA | WD 5.1 mm | det BSED | mag 5 000 x | 20 µm | Nova NanoSEM

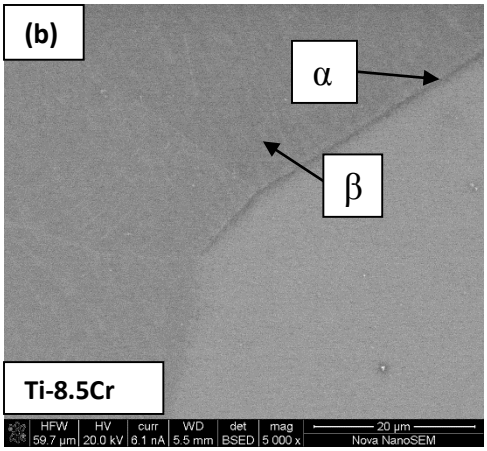
(b)
α
β
Ti-8.5Cr
HFW 59.7 µm | HV 20.0 kV | curr 6.1 nA | WD 5.5 mm | det BSED | mag 5 000 x | 20 µm | Nova NanoSEM

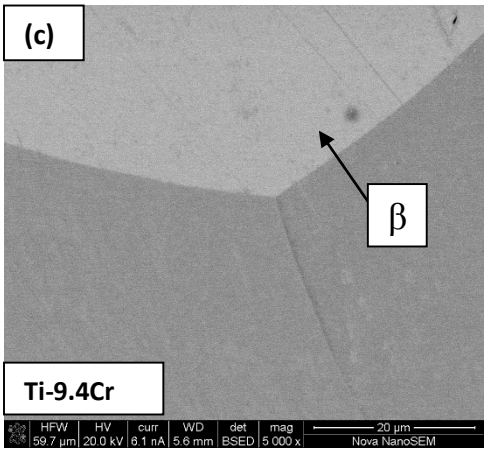
(c)
β
Ti-9.4Cr
HFW 59.7 µm | HV 20.0 kV | curr 6.1 nA | WD 5.6 mm | det BSED | mag 5 000 x | 20 µm | Nova NanoSEM

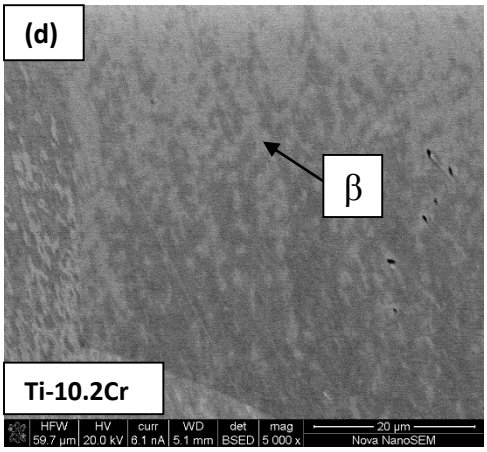
(d)
β
Ti-10.2Cr
HFW 59.7 µm | HV 20.0 kV | curr 6.1 nA | WD 5.1 mm | det BSED | mag 5 000 x | 20 µm | Nova NanoSEM

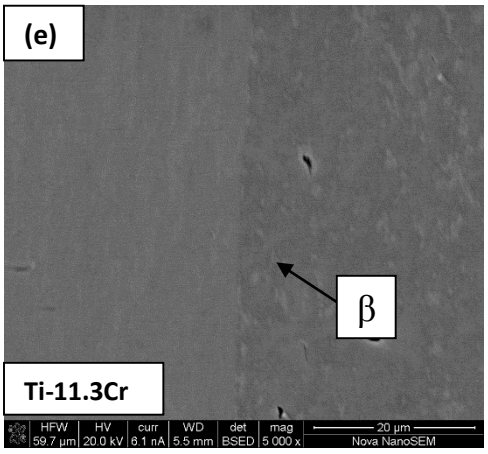
(e)
β
Ti-11.3Cr
HFW 59.7 µm | HV 20.0 kV | curr 6.1 nA | WD 5.5 mm | det BSED | mag 5 000 x | 20 µm | Nova NanoSEM

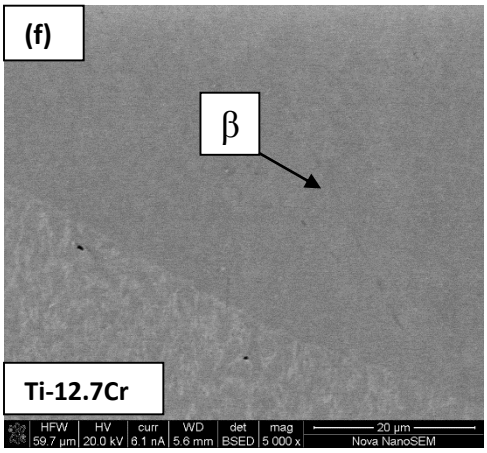
(f)
β
Ti-12.7Cr
HFW 59.7 µm | HV 20.0 kV | curr 6.1 nA | WD 5.6 mm | det BSED | mag 5 000 x | 20 µm | Nova NanoSEM

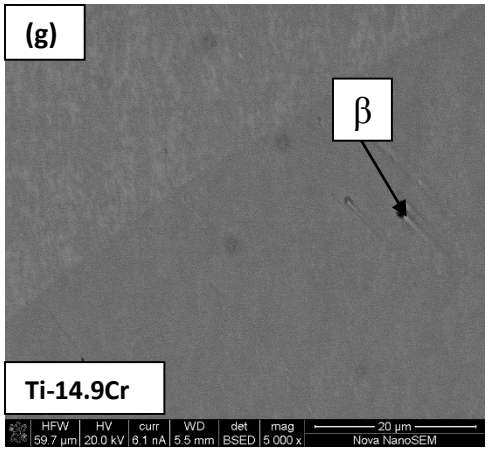
(g)
β
Ti-14.9Cr
HFW 59.7 µm | HV 20.0 kV | curr 6.1 nA | WD 5.5 mm | det BSED | mag 5 000 x | 20 µm | Nova NanoSEM

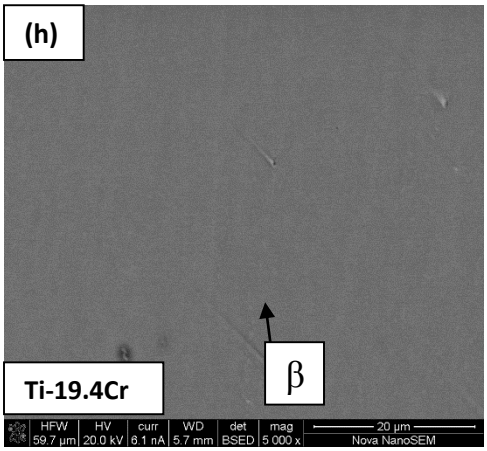
(h)
β
Ti-19.4Cr
HFW 59.7 µm | HV 20.0 kV | curr 6.1 nA | WD 5.7 mm | det BSED | mag 5 000 x | 20 µm | Nova NanoSEM

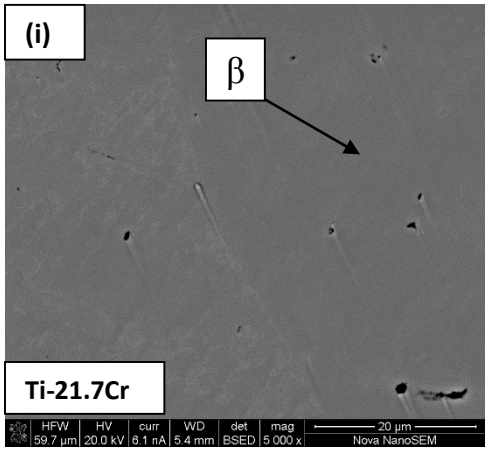
(i)
β
Ti-21.7Cr
HFW 59.7 µm | HV 20.0 kV | curr 6.1 nA | WD 5.4 mm | det BSED | mag 5 000 x | 20 µm | Nova NanoSEM

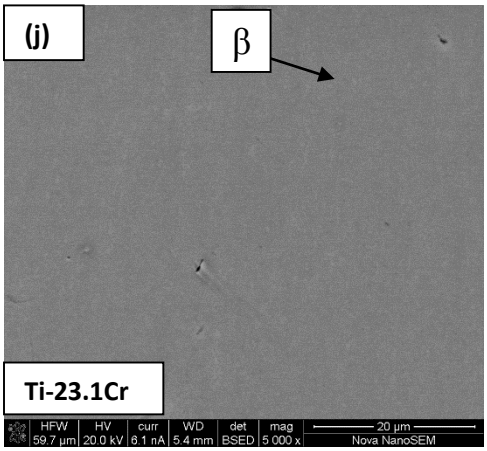
(j)
β
Ti-23.1Cr
HFW 59.7 µm | HV 20.0 kV | curr 6.1 nA | WD 5.4 mm | det BSED | mag 5 000 x | 20 µm | Nova NanoSEM

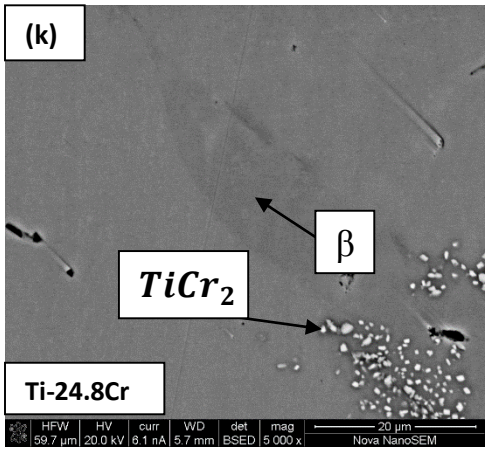
(k)
β
$TiCr_2$
Ti-24.8Cr
HFW 59.7 µm | HV 20.0 kV | curr 6.1 nA | WD 5.7 mm | det BSED | mag 5 000 x | 20 µm | Nova NanoSEM

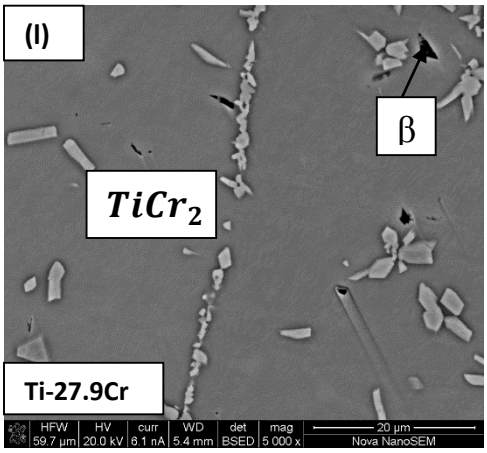
(l)
β
$TiCr_2$
Ti-27.9Cr
HFW 59.7 µm | HV 20.0 kV | curr 6.1 nA | WD 5.4 mm | det BSED | mag 5 000 x | 20 µm | Nova NanoSEM

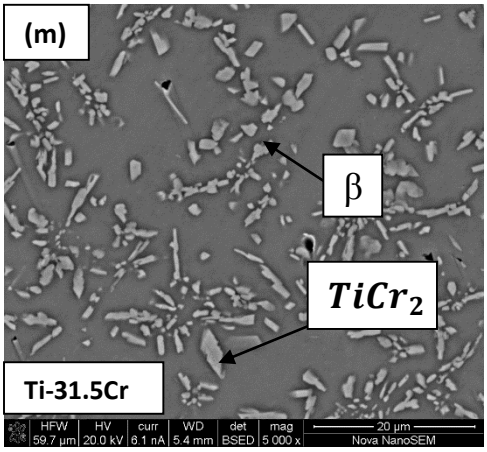

Fig 6.4: (a)-(m) Summary of higher magnification BSE images along entire Cr compositional range.

6.3 X-Ray Diffraction (XRD)

XRD of the graded alloy was conducted along 9 different regions shown schematically in Fig. 6.5. The regions were selected on basis of their compositional gradient and change in microstructure. A slit size of H2 was done for 9 scans to provide a more concise scan than a broad one at a particular region. Out of the 9 scans carried out, 7 scans are carried out extensively on ω phase regions to determine the start and end of the ω phase within the alloy. The other two scans were performed at regions of 100% β phase retention and higher Cr wt% regions with $TiCr_2$ intermetallic phase. The results obtained on ω phase regions will be discussed in detail later in the TEM analysis section.

The various XRD scans obtained for different regions with respect to increasing Cr content are shown in Fig 6.6 (a)-(g) [hypo eutectoid regions] and Fig 6.7 (a) and(b) [hyper eutectoid region] for low and higher wt% Cr contents, respectively.

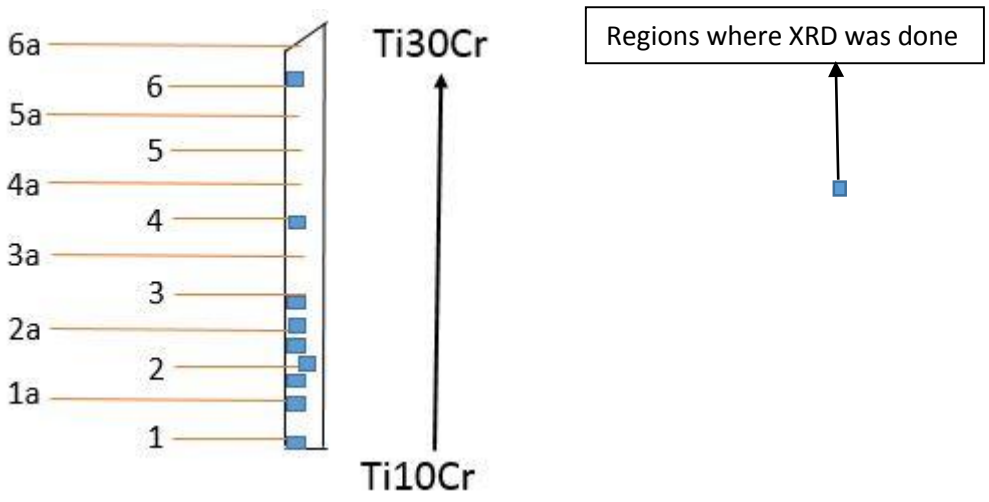

Fig 6.5: Schematic Representation of the Regions and Sub-regions for acquiring XRD scans.

XRD scans in Fig. 6.6(a) and (b) for Region 1: Ti-(7.8-8.5)Cr and Region 1a: Ti-(8.5-9.3)Cr, respectively, show the presence of α-Ti (HCP) and β-Ti (BCC) phases. The XRD scans in Fig. 6.6(c)-(e) for Region 1b: Ti-(9.3-9.8)Cr to Region 3: Ti(9.2-10.1)Cr, respectively, show the presence of β peaks and unknown peaks indexed as ω peaks, based on knowledge of TEM analysis presented later. The well-structured ω phase being a small phase fraction within the metastable β phase matrix, made it surprising to be detected in XRD scans. The ω phase indexing was carried out on basis of XRD studies of ω phase in β Ti alloys done by Shun Guo et al (47), Sergey Dubinsky et al (46), D.J.Lin et al (43), Wen-Fu Ho (44), and Bing Zhang et al (45). Since chromium is a β stabilizer, there is an increase in the content of β-Ti with increasing Cr wt% along the length of the graded alloy. The ω phase peaks indexed reduces as the wt% of Cr increases and finally disappears at above (12-13) wt% Cr.

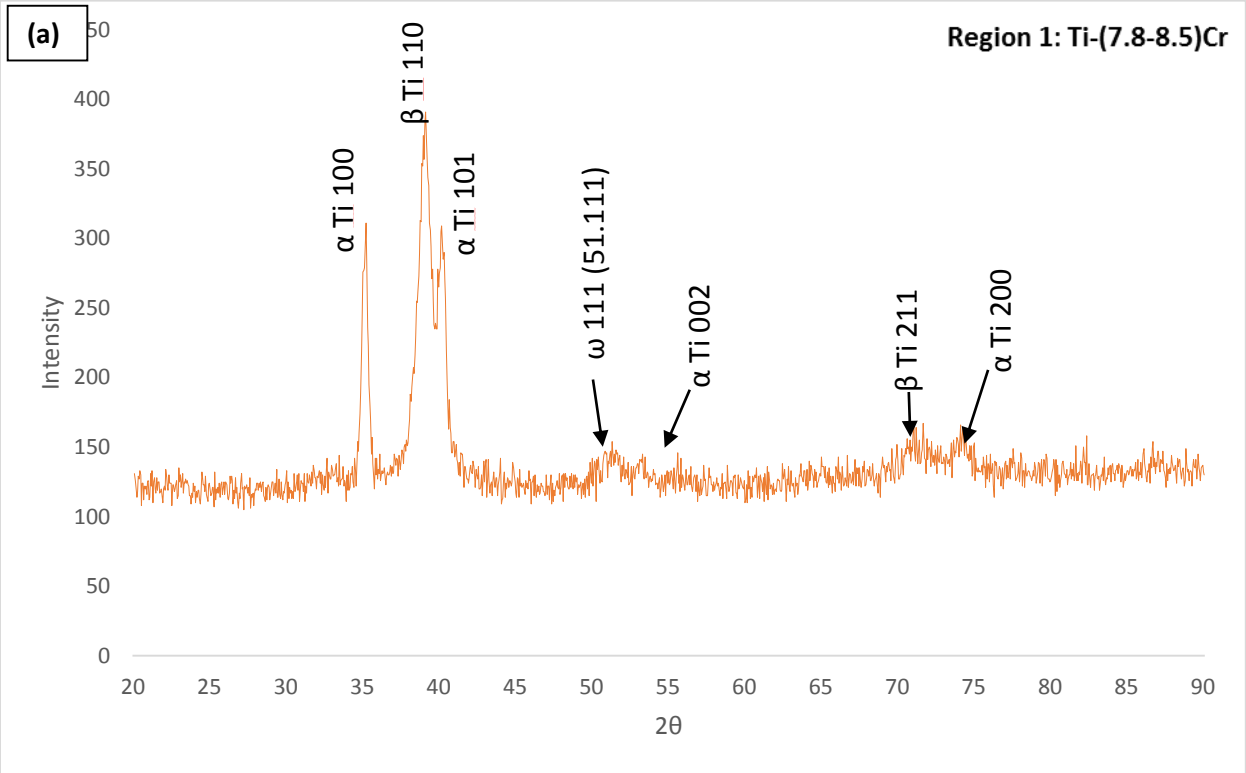
(a)
Region 1: Ti-(7.8-8.5)Cr
Intensity
2θ
α Ti 100
β Ti 110
α Ti 101
ω 111 (51.111)
α Ti 002
β Ti 211
α Ti 200

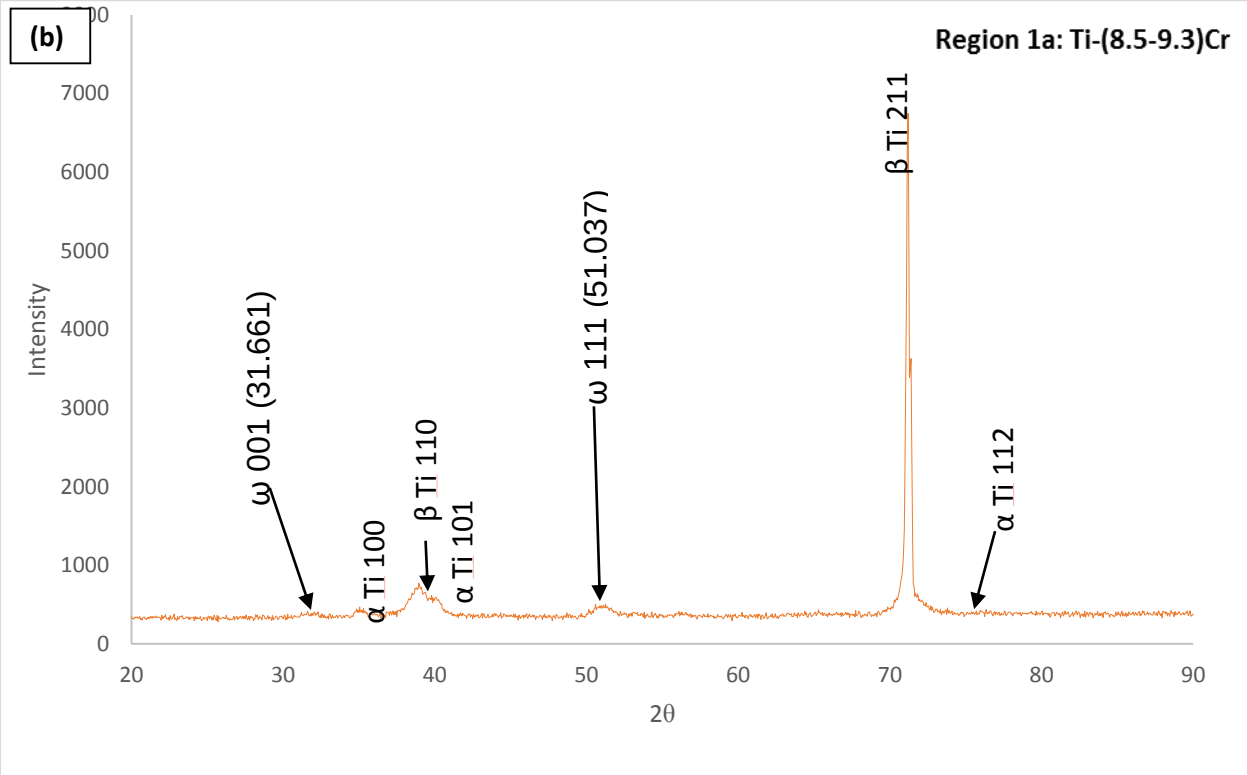
(b)
Region 1a: Ti-(8.5-9.3)Cr
Intensity
2θ
ω 001 (31.661)
α Ti 100
β Ti 110
α Ti 101
ω 111 (51.037)
β Ti 211
α Ti 112

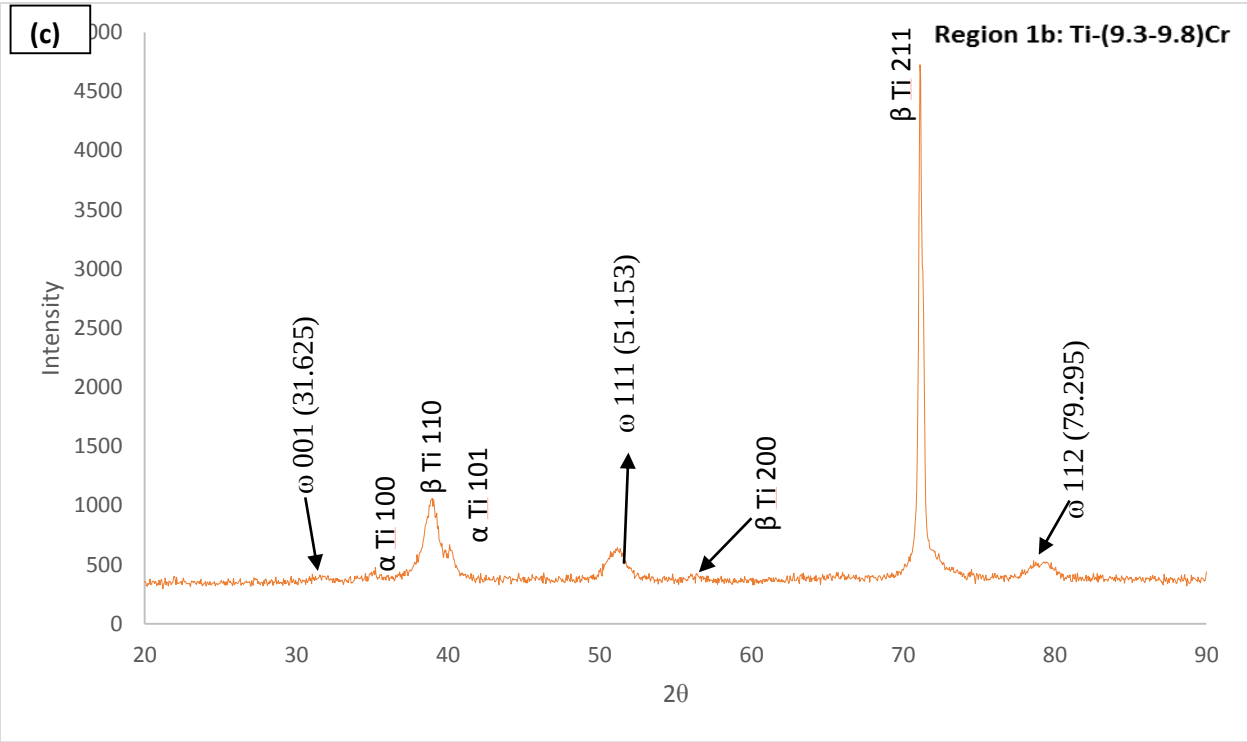
(c)
Region 1b: Ti-(9.3-9.8)Cr
Intensity
2θ
ω 001 (31.625)
α Ti 100
β Ti 110
α Ti 101
ω 111 (51.153)
β Ti 200
β Ti 211
ω 112 (79.295)

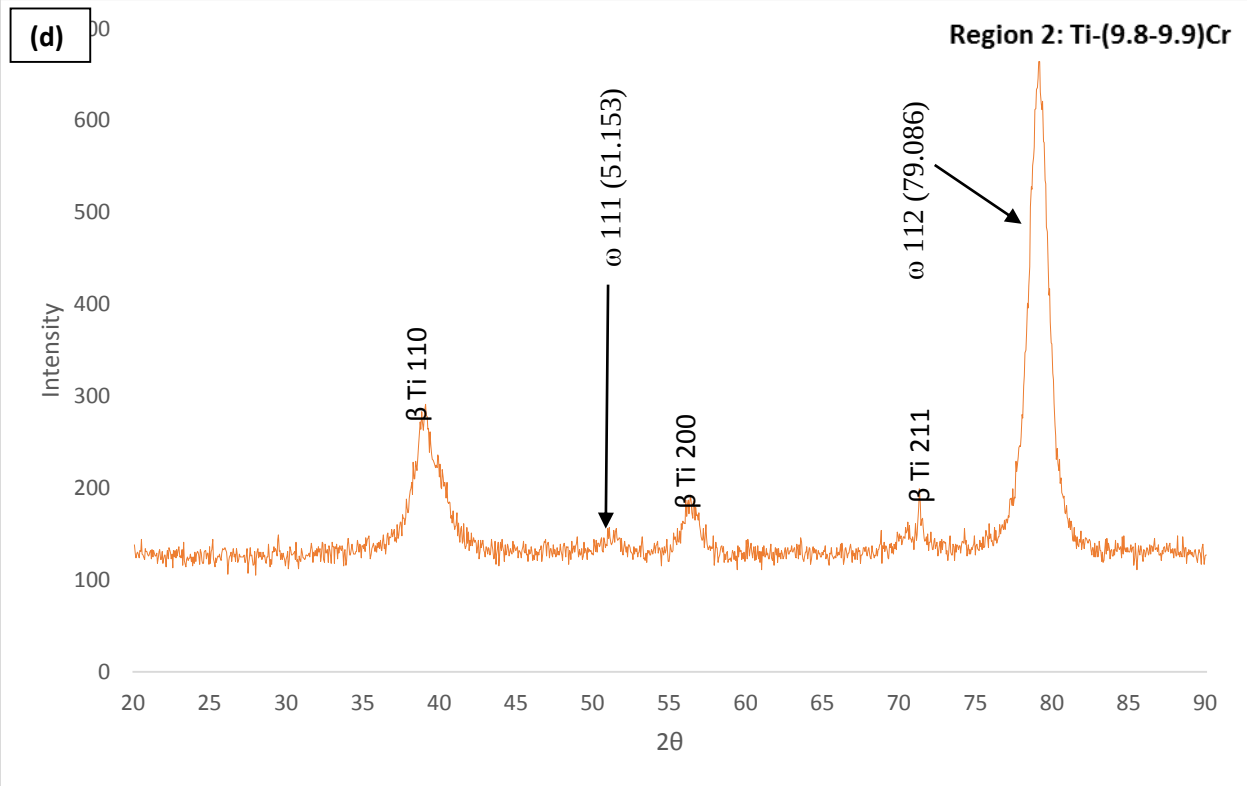
(d)
Region 2: Ti-(9.8-9.9)Cr
Intensity
2θ
β Ti 110
ω 111 (51.153)
β Ti 200
ω 112 (79.086)
β Ti 211

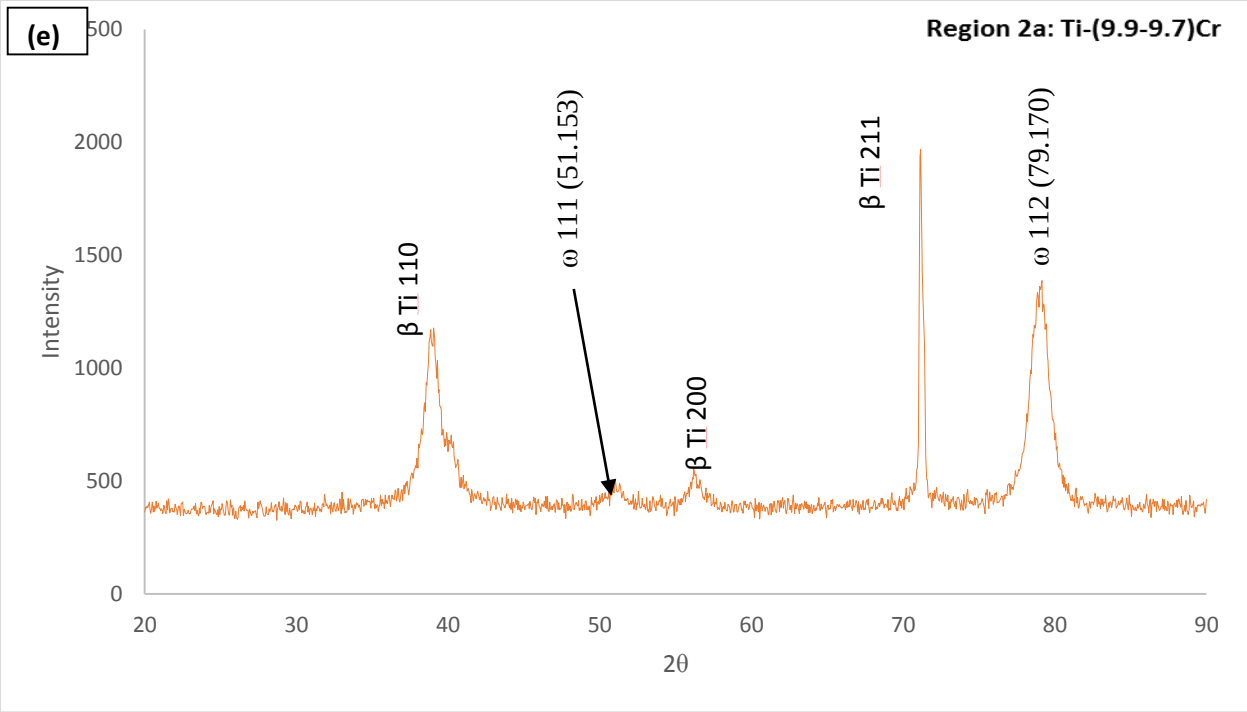
(e)
Region 2a: Ti-(9.9-9.7)Cr
Intensity
2θ
β Ti 110
ω 111 (51.153)
β Ti 200
β Ti 211
ω 112 (79.170)
0
500
1000
1500
2000
20
30
40
50
60
70
80
90

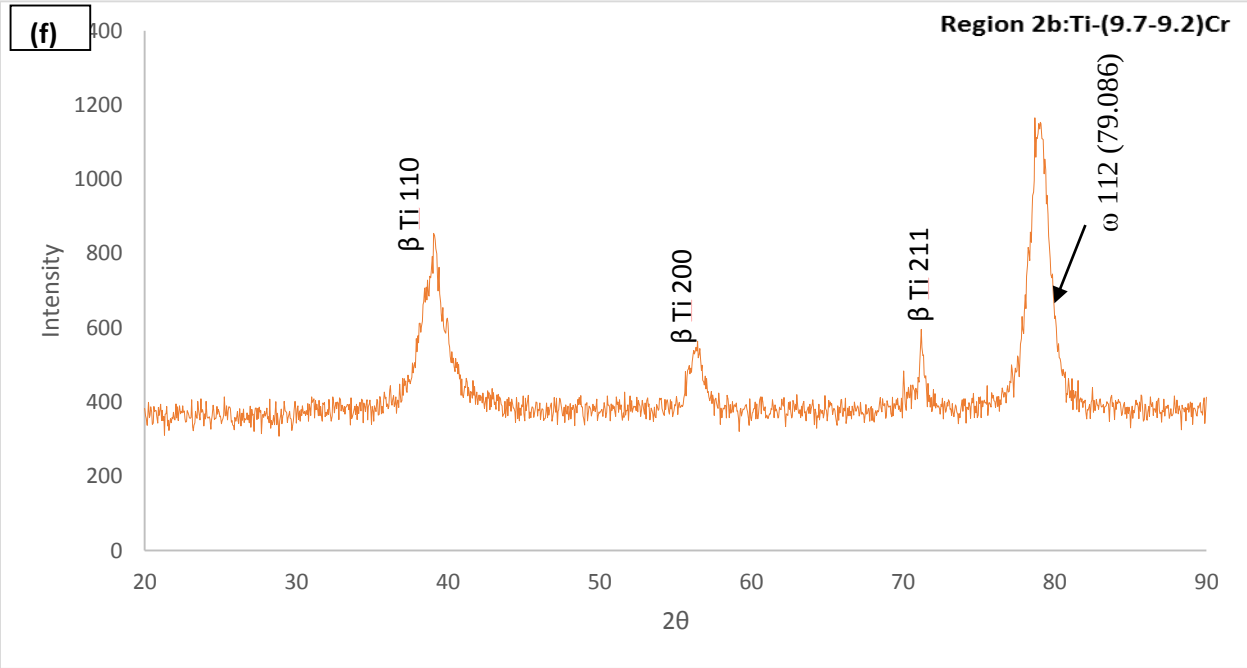
(f)
Region 2b:Ti-(9.7-9.2)Cr
Intensity
2θ
β Ti 110
β Ti 200
β Ti 211
ω 112 (79.086)
0
200
400
600
800
1000
1200
20
30
40
50
60
70
80
90

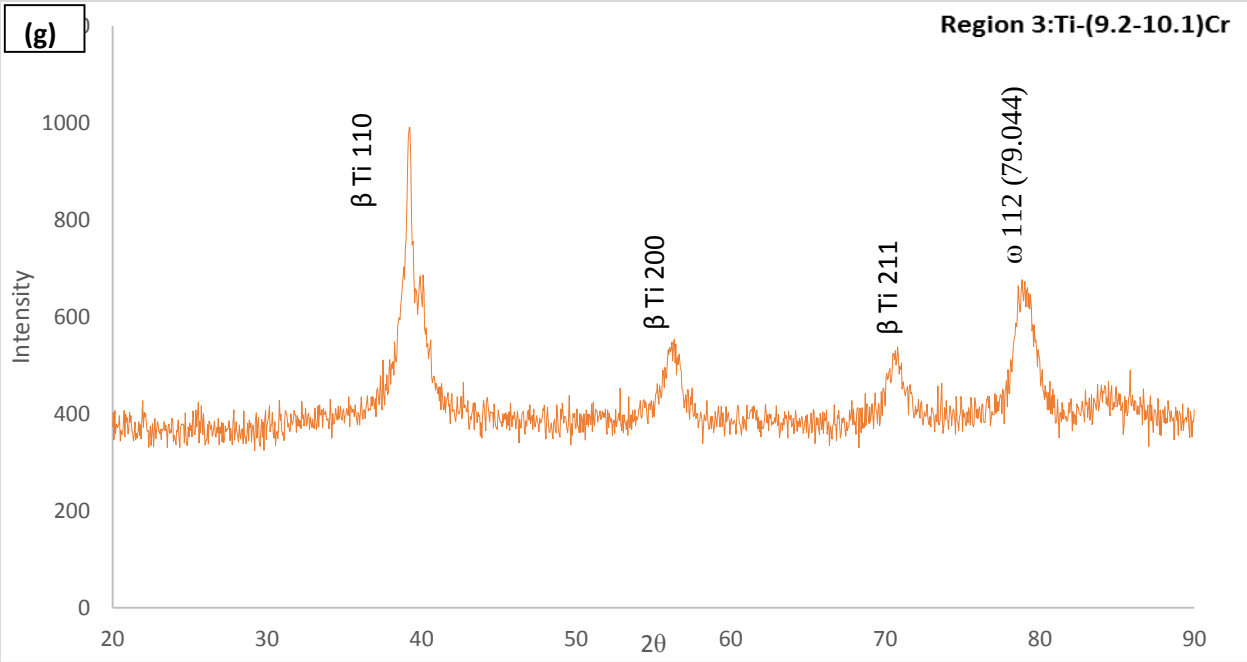

Fig 6.6: XRD scans of low Cr wt% Regions (a) Ti-(7.8-8.5)Cr, (b) Ti-(8.5-9.3)Cr, (c) Ti-(9.3-9.8)Cr, (d) Ti-(9.8-9.9)Cr, (e) Ti-(9.9-9.7)Cr, (f) Ti-(9.7-9.2)Cr, and (g) Ti-(9.2-10.1)Cr.

The microstructural evolution observed in Fig 6.6 (a)-(g) is completely different compared to “as deposited” alloy in chapter 4 and “furnace cooled” alloy in chapter 5. The probable cause for ω phase formation as discussed earlier is the spontaneous cooling from β transus temperature leading to prevention of α phase formation. The presence of α phase in Fig 6.6 (a) and (b) are most likely due to preference over $\beta_1+\beta_2$ metastable state or oxidation effect near the edges of the sample.

β peak shifts are negligible when compared to “as deposited” and “furnace cooled” samples. The lack of texturing, ω phase occupying a small volume fraction and minimal new phase nucleation, has been determined as the reason for the lack of β peak shifts in Fig. 6.6.

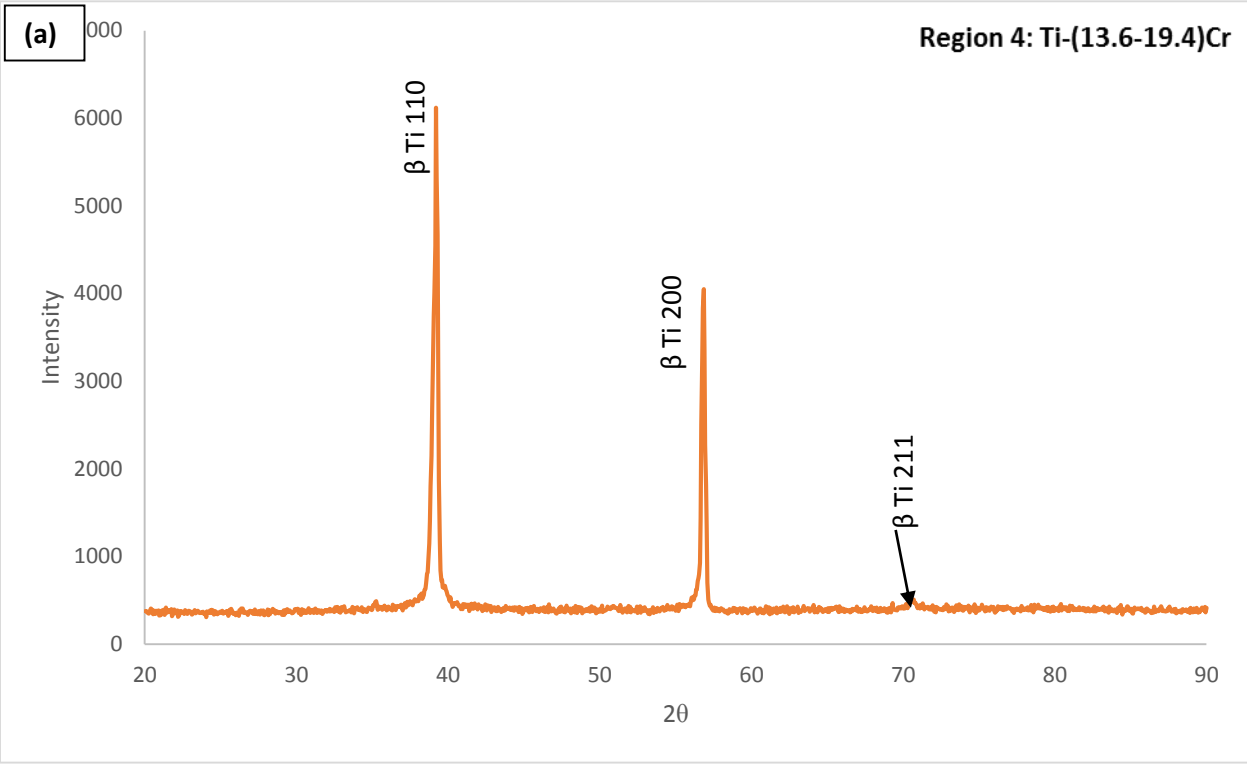

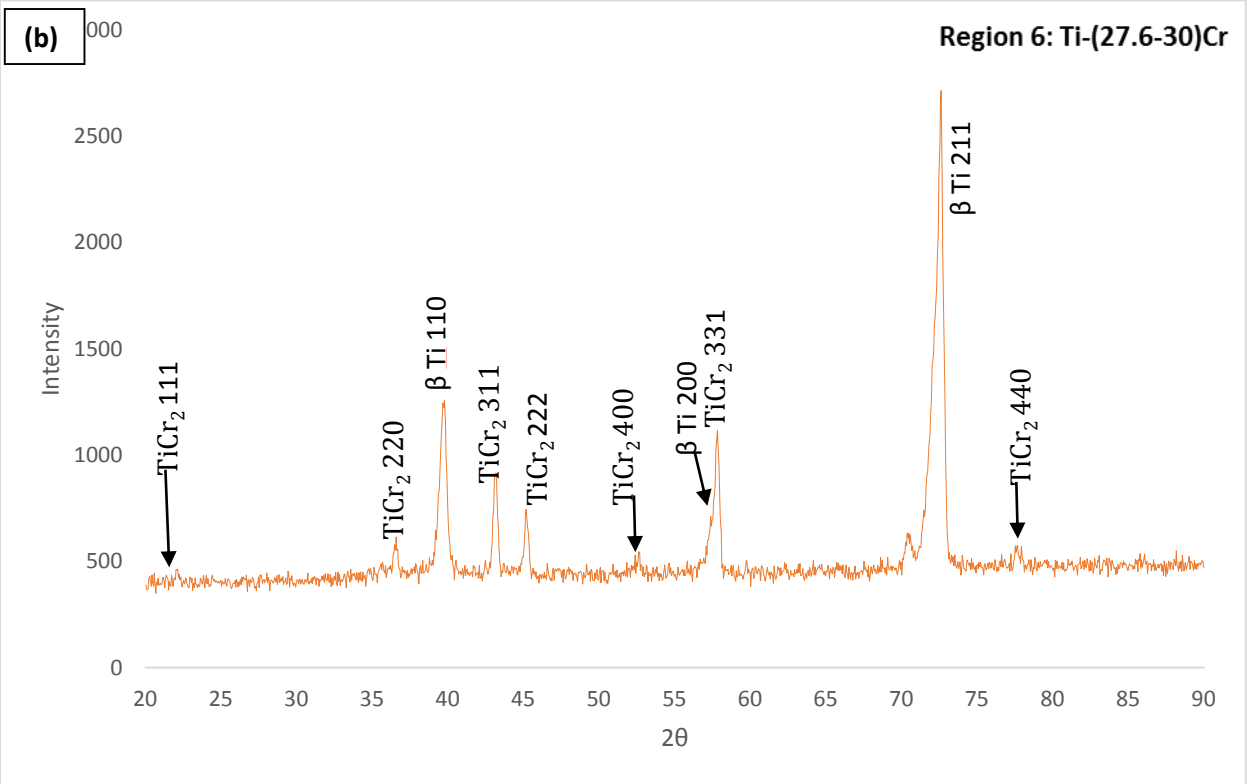

Fig 6.7: XRD scans of Higher Cr wt% Regions (a) Ti-(13.6-19.4)Cr and (b) Ti-(27.6-30)Cr.

Fig 6.7 shows XRD scans on the higher Cr wt% regions. Fig 6.7: (a) and (b) indicate Region 4: Ti-(13.6-19.7)Cr and Region 6: Ti-(27.6-30)Cr. Unlike the "as deposited" and "furnace cooled" samples co-existence of α, $TiCr_2$ and β phase is not observed. At Region 4: Ti(13.6-19.7)Cr, only β phase is observed, while at Region 6: Ti(27.6-30)Cr intermetallic $TiCr_2$ and β phase are observed which confirm the BSE images shown in Fig. 6.4. It was also observed that the volume fraction of $TiCr_2$ intermetallic phase in β matrix phase is not as dense as "furnace cooled" samples.

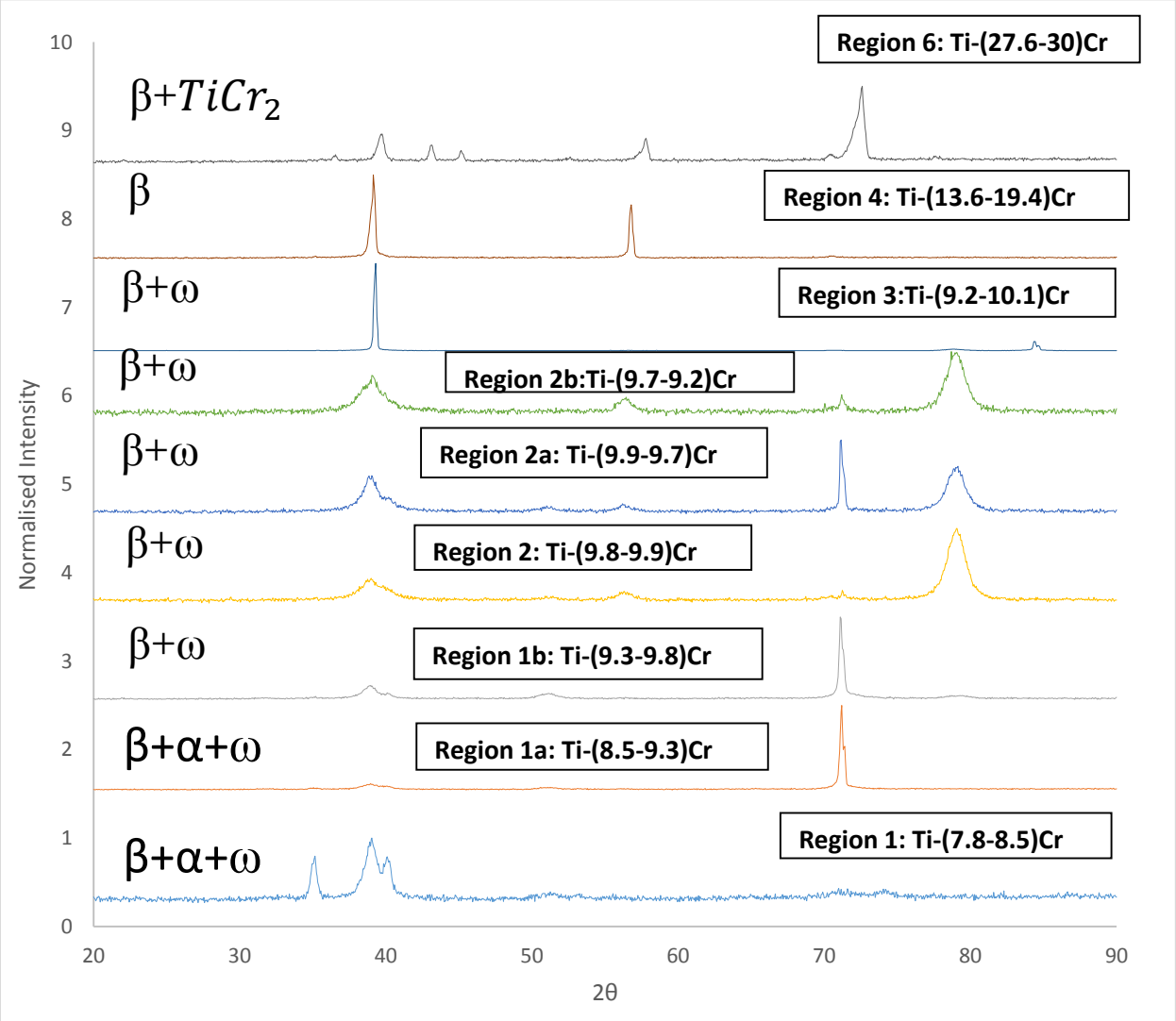

Fig 6.8: XRD scan summary along the regions of the graded alloy.

However, a reasonable amount of β phase peak shift was observed at higher Cr wt% especially in Region 6: Ti-(27.6-30)Cr, shown in Fig 6.7 (b). Stresses induced due to presence of $TiCr_2$ intermetallic on β phase at the same region leads to β peak shifts.

Region	Composition	Calculated lattice constant (a) in Å		PDF lattice constant (a) in Å (Vegards law)	
		β phase	$TiCr_2$ phase	β phase	$TiCr_2$ phase
1	Ti-(7.8-8.5)Cr	3.25	-	3.27	-
1a	Ti-(8.5-9.3)Cr	3.25	-	3.27	-
1b	Ti-(9.3-9.8)Cr	3.26	-	3.26	-
2	Ti-(9.8-9.9)Cr	3.25	-	3.26	-
2a	Ti-(9.9-9.7)Cr	3.25	-	3.26	-
2b	Ti-(9.7-9.2)Cr	3.28	-	3.26	-
3	Ti-(9.2-10.1)Cr	3.26	-	3.26	-
4	Ti-(13.6-19.4)Cr	3.25	-	3.23	-
6	Ti-(27.6-30)Cr	3.20	6.95	3.18	6.94

Table 6.2: Lattice Parameters of β and $TiCr_2$ Phases along the graded regions.

Fig 6.8 XRD scans summarize the phase changes along the length of the graded alloy. The lattice parameters of β and $TiCr_2$ phases versus the lattice parameters calculated theoretically based on Vegard's Law at different regions are listed in table 6.2.

There is relatively good agreement between experimentally measured and calculated values, e.g. trend of decreasing β phase lattice parameter with increasing Cr wt%.

In summary, from Region 1: Ti-(7.9-8.5)Cr to Region 1a: Ti-(8.5-9.3)Cr an increase in β phase with respect to α phase is seen. Region 1b: Ti-(9.3-9.8)Cr to Region 3: Ti-(9.2-10)Cr shows the presence of ω and β phase. Region 4:Ti-(13.6-19.4)Cr shows presence of β phase. Region 6:Ti-(27.6-30)Cr exhibits $TiCr_2$ intermetallic phase and β phase.

6.4 FIB Lift-Out

A FIB lift out is carried out at Region 2: Ti-9.4Cr. The area chosen as region of interest to be studied by TEM analysis is due to the presence of assumed ω phase mentioned previously in the XRD results.

TEM imaging at this region along with the XRD scans and high micro-hardness values presented next will help unequivocally determine the presence of ω phase. Fig 6.9 (a)-(d) show the various stages of FIB lift-out and polishing process

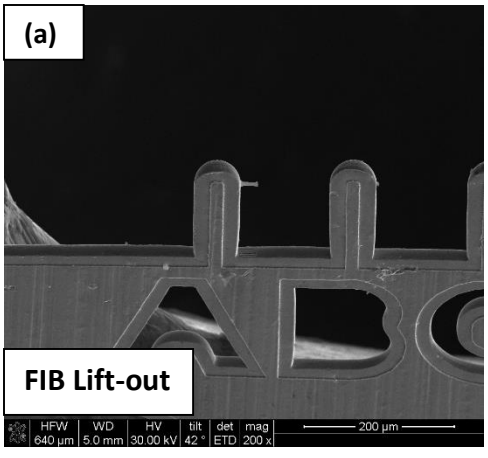

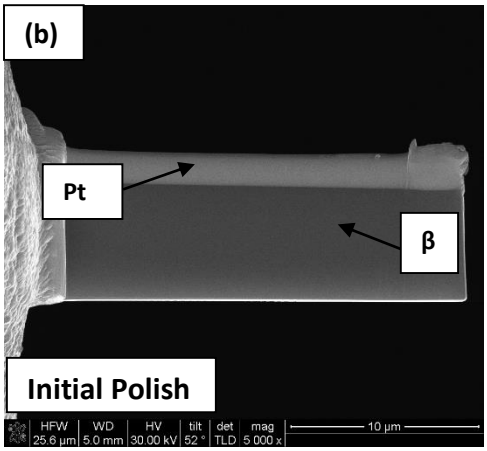

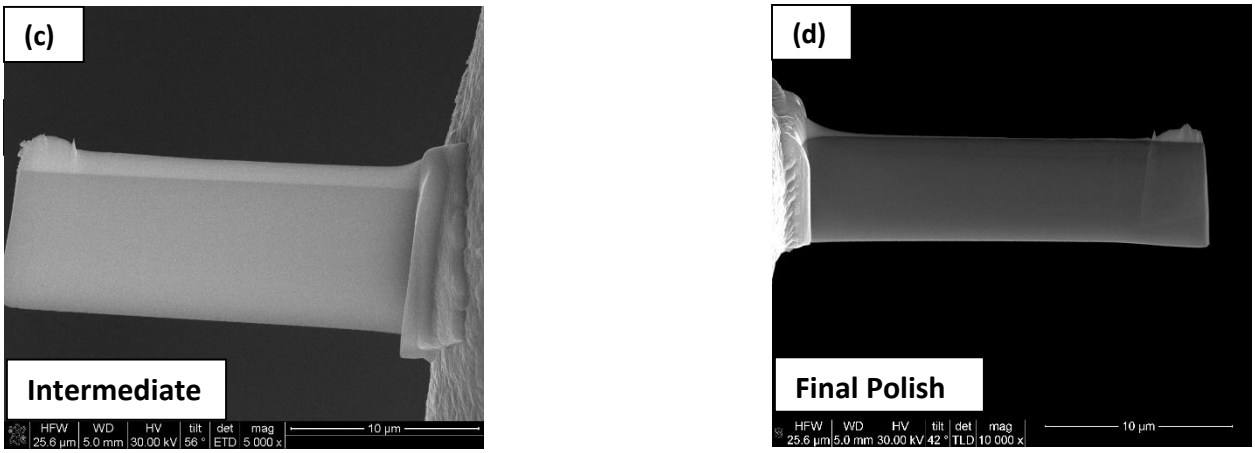

6.9: SEM images of (a) FIB Lift-out (b) Initial Polish, (c) Intermediate Polish, and (d) Final Polish.

6.5 Transmission Electron Microscopy (TEM) and Micro-diffraction Studies

Electron diffraction patterns along with Dark field TEM images of Ti-9.4Cr from Region 2 of the sample indicate the presence of well-structured ω phase within a β matrix. Fig 6.10 (a) shows the overall microstructure of the ω phase at lower magnification, while Fig 6.10 (b) shows a higher magnification of the ω phase. Fig 6.17(c) is a selected area diffraction pattern of ω phase indexed inside the β matrix phase. Fig 6.17 (c) clearly indicates that the ω phase as an HCP structure and β matrix phase as a BCC structure.

The size of ω phase from Fig 6.10 (b) calculated from image J software is ~4.6 nm which is in agreement with size observed by Wang et al (48). Fig 6.10 (c) shows the SAD pattern along with orientation relationship of ω phase within the β matrix. Fig 6.10 (a) and (b) are the respective DF diffractions of ω phase marked by a red circle in the SAD pattern from Fig 6.10 (c). The results verify the XRD results presented earlier.

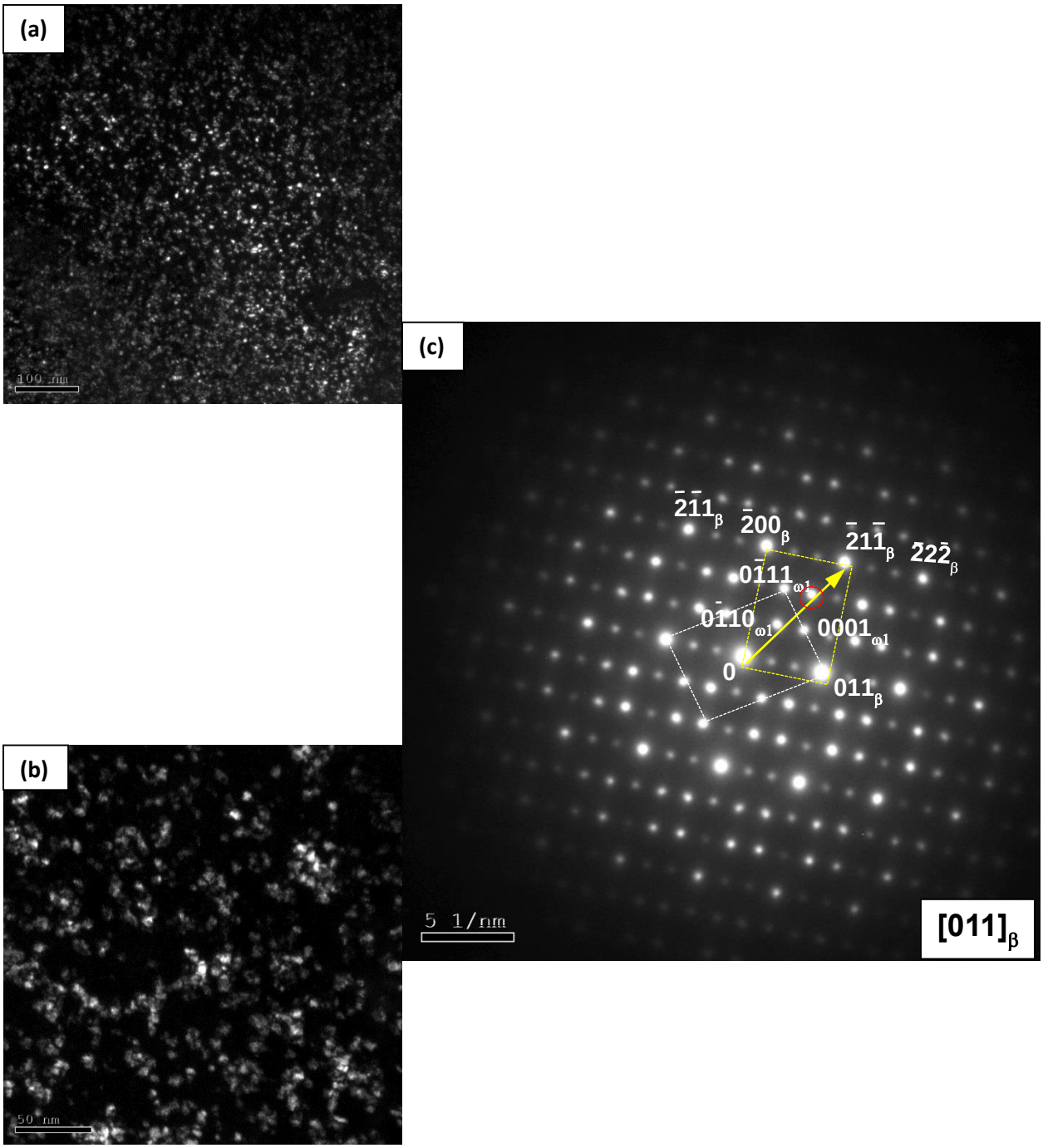

Fig 6.10: DF TEM images of ω phase at (a) low magnification and (b) high magnification, and (c) SAD pattern of ω phase within β matrix viewed down zone axis [011].

6.6 Micro-Hardness

Due to the microstructural phase evolution from Ti-10Cr to Ti-30Cr, there are corresponding changes in the micro-hardness values. Vickers hardness measurements were made along the sample gradient with a spacing of 0.5 mm between indents with three measurements at each location or layer. Fig. 6.11 (a) and (b) show the hardness values as a function of Cr wt% and distance along the sample, respectively. It is evident that the highest hardness is at Regions of 7.8-11 wt% Cr due to the presence of the harder ω phase with hardness approximating to 550HV. The ω phase nucleation accounted for a substantial increase in ~300 HV but decreases when the ω phase is depleted with increasing Cr wt%. In addition, the hardness of the "Air cooled" alloy at higher Cr wt% of Ti-(25-30)Cr has been determined to be around 500 HV.

The presence of $TiCr_2$ is responsible for the hardness increase at higher Cr wt%. However, the hardness at higher Cr wt% is less than that of the "Furnace cooled" alloy. The presence of three phase region of α, β and $TiCr_2$ is responsible for an increase in hardness of the "furnace cooled" sample. Unlike the "as deposited" alloy, the air cooled alloy has undergone even heat treatment and quick cooling. Hence there are not two different readings of hardness at around 30 wt% Cr as seen in "as deposited" alloys discussed in chapter 4. On basis of highest hardness amongst the three alloys, the ω phase region of the "air cooled" sample has the highest hardness.

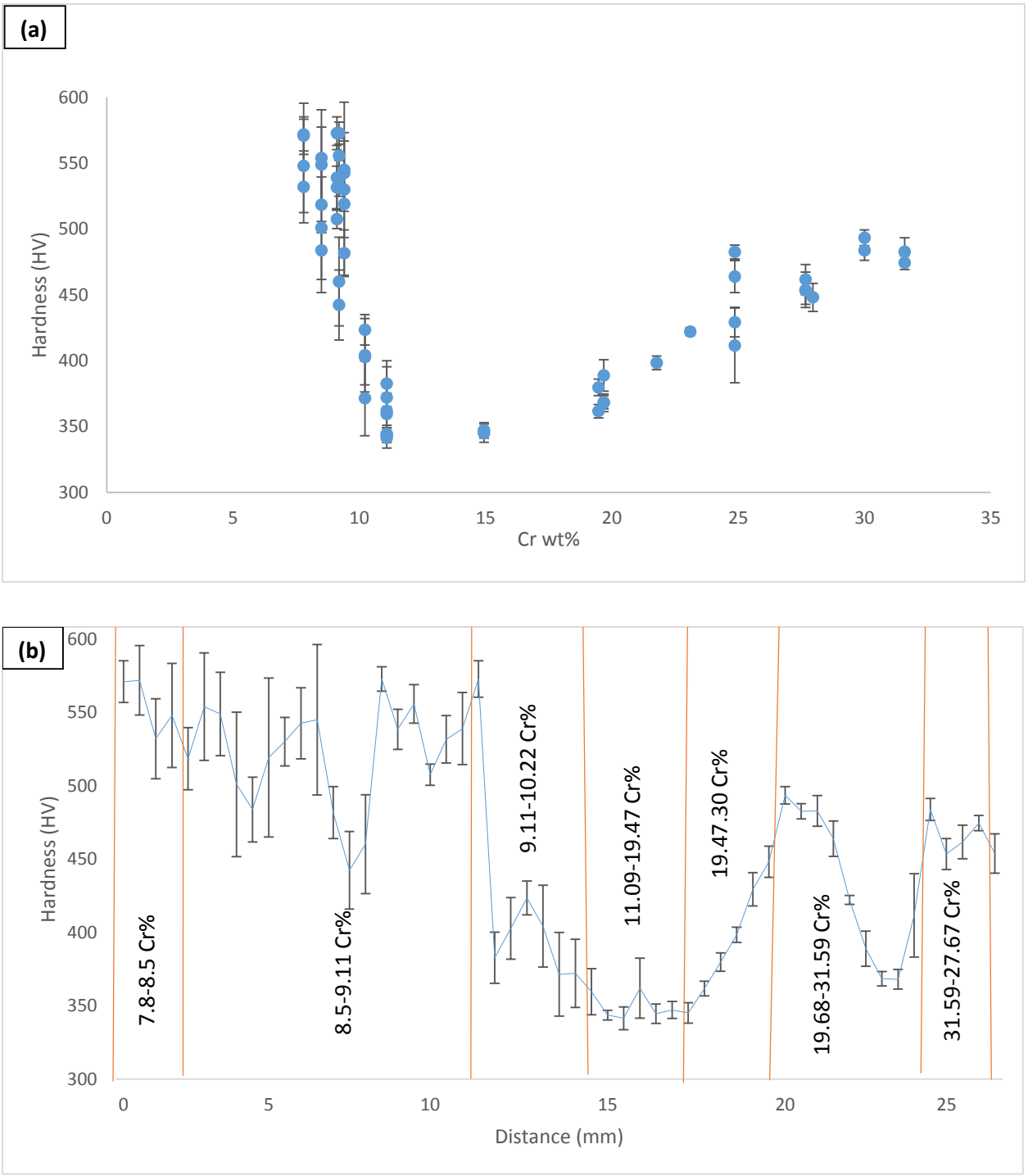

Fig 6.11: Vickers micro-hardness values as a function of (a) Cr wt% and (b) distance along the graded alloy.

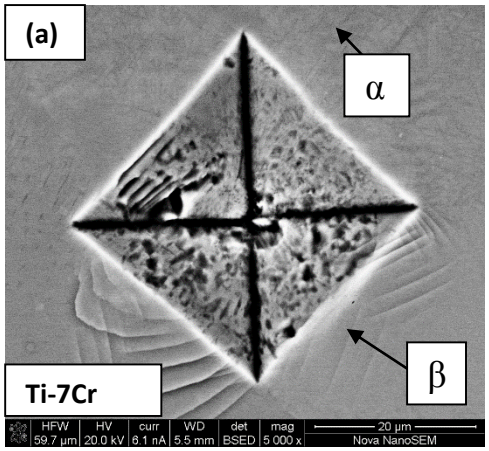
(a)
α
β
Ti-7Cr
HFW 59.7 µm | HV 20.0 kV | curr 6.1 nA | WD 5.5 mm | det BSED | mag 5 000 x | 20 µm | Nova NanoSEM

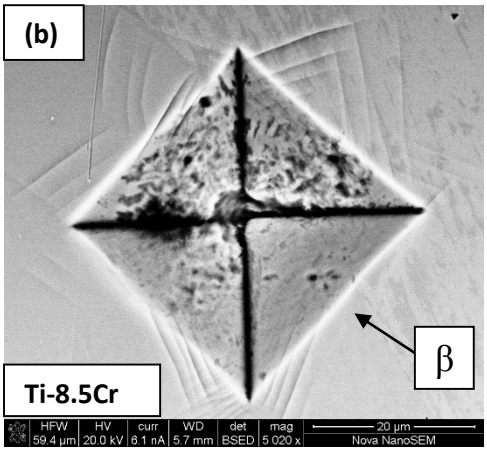
(b)
β
Ti-8.5Cr
HFW 59.4 µm | HV 20.0 kV | curr 6.1 nA | WD 5.7 mm | det BSED | mag 5 020 x | 20 µm | Nova NanoSEM

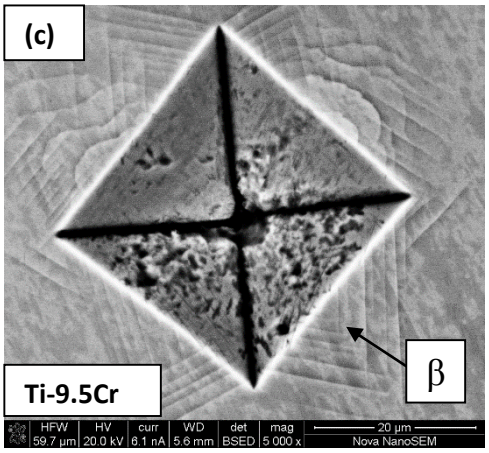
(c)
β
Ti-9.5Cr
HFW 59.7 µm | HV 20.0 kV | curr 6.1 nA | WD 5.6 mm | det BSED | mag 5 000 x | 20 µm | Nova NanoSEM

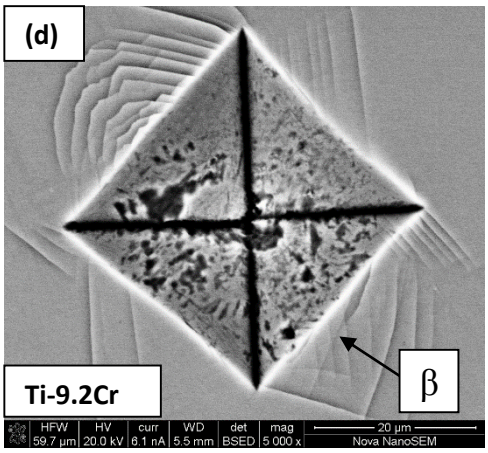
(d)
β
Ti-9.2Cr
HFW 59.7 µm | HV 20.0 kV | curr 6.1 nA | WD 5.5 mm | det BSED | mag 5 000 x | 20 µm | Nova NanoSEM

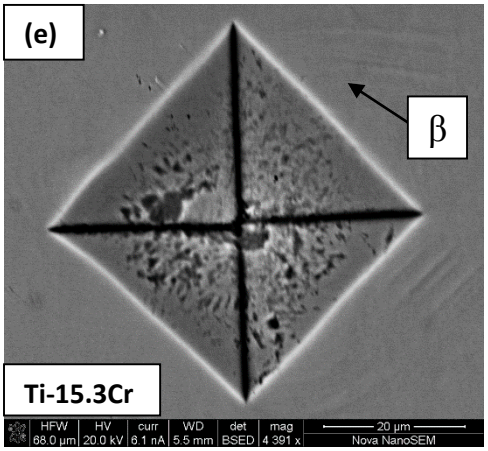
(e)
β
Ti-15.3Cr
HFW 88.0 µm | HV 20.0 kV | curr 6.1 nA | WD 5.5 mm | det BSED | mag 4 391 x | 20 µm | Nova NanoSEM

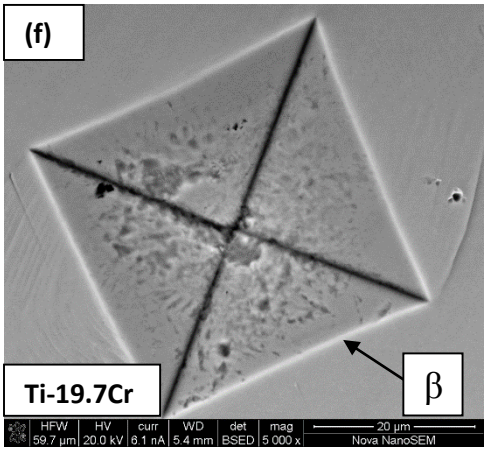
(f)
β
Ti-19.7Cr
HFW 59.7 µm | HV 20.0 kV | curr 6.1 nA | WD 5.4 mm | det BSED | mag 5 000 x | 20 µm | Nova NanoSEM

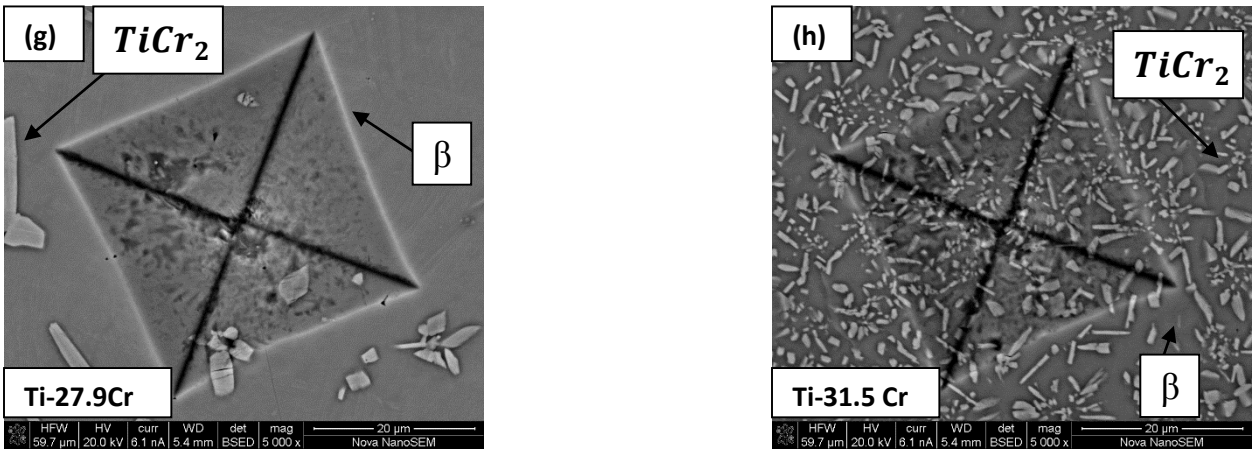

Fig 6.12: SEM images of Vickers indents for compositions of (a) Ti-7Cr, (b) Ti-8.5Cr, (c) Ti-9.5Cr, (d) Ti-9.2Cr, (e) Ti-15.3Cr, (f) Ti-19.7Cr, (g) Ti-27.9Cr, and (h) Ti-31.5Cr

Based on the SEM images of the Vickers indents shown in Fig 6.12 (a)-(d), it is evident that the highest hardness is at low Cr wt% where ω phase is present. With higher hardness in this region, there is corresponding brittleness indicated by presence of shear bands surrounding the indents, a sign of strain localization. The other images of the indents in Fig. 6.12 (e)-(h) do not show this deformation since there is no ω phase.

In summary, the heat treated and air cooled LENS^{TM} Ti-10Cr to Ti-30Cr compositionally graded alloy was characterized by SEM BSE imaging, XRD, TEM-SAD in selected region, and micro-hardness measurements to determine processing-structure-property relations. The ω, α-Ti, β-Ti, and $TiCr_2$ phases were identified in varying phase fractions which were influential in determining the hardness values. Absence of wide scale nucleation of α phase and formation of ω phase within the β phase is the result of quick cooling from elevated temperature. The kinetics involved causes a diffusion less phase transformation of the ω phase. In addition, the phase fraction of $TiCr_2$ intermetallic has been observed to be lesser than that of “furnace cooled” sample.

CHAPTER 7

SUMMARY AND CONCLUSIONS

A compositionally graded Ti-xCr (10≤x≤30 wt%) alloy has been fabricated using a Laser Engineered Net Shaping (LENS^{TM}) process from Ti and Cr powders in order to study the microstructural phase evolution along a compositional gradient for both as-deposited and heat treated alloys (1000°C followed by furnace cooling or air cooling). The alloys were characterized by SEM BSE imaging, XRD, EBSD and micro-hardness measurements to determine processing-structure-property relations.

"As Deposited alloy"

- At low Cr content,(Ti~7-10 wt%), wide scale selective non homogeneous α phase nucleation in β phase matrix is observed due to the reheating effect during the solidification process.
- The hardness at these regions has been approximated to ~360HV.The uneven α phase nucleation in β matrix is responsible for this hardness value.
- Eutectoid reaction of β decomposition to α and $TiCr_2$ occurs at Ti~13Cr wt%, with regions of Cr less than 13 wt% are hypo eutectoid, while those above 13 wt% Cr are hyper eutectoid regions.
- From Ti~13-20 Cr wt% minimal α phase nucleation in β matrix is observed and thus micro hardness is still around ~350HV.
- From Ti~25-30 Cr wt% an increase in hardness to ~450HV is observed due to the nucleation of the hard C15 $TiCr_2$ intermetallic phase.

- At Ti~31Cr wt% (lower deposited layer) the increased hardness of ~450 HV is due to nucleation of $TiCr_2$ intermetallic phase via selective reheating during LENS deposition of lower layers, while at Ti~29Cr wt% (upper deposited layer) being athermally heated exhibit only β phase with minimal or no nucleation of $TiCr_2$ intermetallic phase and a lower micro hardness of ~400HV.

"Furnace cooled alloy"

- At low Cr content(Ti~7-10 wt%), wide scale homogeneous α phase nucleation as dendritic structures in β phase matrix is observed due to the β solutionizing of the alloy at 1000°C for 30 minutes in an Ar atmosphere followed by slow furnace cooling. The hardness at these regions has been approximated to ~400HV.
- Unlike "as deposited" alloys, α phase has been observed throughout the sample, including regions of higher Cr wt%.
- From Ti~13-20 Cr wt%, α phase nucleation in β matrix decreases since Cr acts as a β stabilizer in Ti-Cr alloy. Being largely β phased, the micro hardness is around ~360HV.
- From Ti~25-30 Cr wt%, an increase in hardness to ~525HV is observed due to the nucleation of hard C15 $TiCr_2$ intermetallic and α phase within a β matrix phase.
- At 29.2 wt% Cr (upper layer) and 31.2 wt% Cr (lower layer), β, α and $TiCr_2$phases are observed. Undercooling followed by slow furnace cooling initiates a homogeneous phase nucleation throughout the sample unlike the "As Deposited" alloy where two different crystal structures are obtained due to athermal heating and selective reheating.

“Air cooled alloy”

- At low Cr content (Ti~7-10 wt%), wide scale ω phase nucleation in β phase matrix is observed with minimal amounts of α phase nucleation.
- β solutionizing of the alloy at 1000°C for 30 minutes in an Ar atmosphere followed by quick air cooling facilitates the formation of diffusionless ω phase. The hardness at these regions has been approximated to ~525HV.
- Unlike “furnace cooled” alloy, α phase has been observed only at the edges of the sample where Cr wt% is less.
- From Ti~13-20 Cr wt%, 100% β phase retention is observed with a micro hardness around ~360HV.
- From Ti~25-30 Cr wt%, an increase in hardness to ~475HV is observed due to the nucleation of hard C15 $TiCr_2$ phase within a β matrix phase.
- The phase fraction of $TiCr_2$ is comparatively less with respect to furnace cooled alloy due to quick air cooling.
- At 27.9 wt% Cr (upper layer) and 31.5 wt% Cr (lower layer), β and $TiCr_2$phases are observed. Undercooling followed by quick air cooling initiates a homogeneous phase nucleation throughout the sample unlike the “As Deposited” alloy where two different crystal structures are obtained due to athermal heating and selective reheating.

On basis of the study conducted, bone fixation plates require higher elastic moduli at the center of implant with respect to lower elastic moduli at the edges. Since elastic modulus is usually directly proportional to hardness, an assessment of suitable alloy for

use based on microstructure and hardness among the three alloy systems studied are as follows. Since the ω phase exhibits brittle fatigue issues, it would not be good in a load bearing implant material. Therefore, the microstructural evolution of β (more compliant on edges of implant) to α + β (stiffer in center of implant) regions would be more appropriate. The $TiCr_2$ phase, which results in increased hardness and likely stiffness, would also be acceptable in the center of the implant to avoid the stress shielding effect.

To summarize, the “furnace cooled” alloy with α and β phases at low Cr wt% is preferred at fracture sites that require high elastic modulus, while β phase regions of the “air cooled” alloy is preferred at edges where the elastic modulus required by the implant is less. The ω phase region of higher hardness is not recommended since there are deformation bands due to shear localization that promotes fatigue issues.

CHAPTER 8

RECOMMENDATIONS FOR FUTURE WORK

Further studies into the Ti-Cr alloy system could include:

1. Due to potential applications in high temperature tribology, wear tests should be conducted for the different compositions of “as deposited”, “furnace cooled” and “air cooled” alloys
2. Tribo-corrosion tests of the fabricated samples in a saline/corrosive environment.
3. More detailed TEM studies on other areas of interest and to determine their effects on hardness and wear resistance.

REFERENCES

1. Bihlman B. Titanium Supply Chain Trends For The Aerospace Industry. TITANIUM 2014. Chicago: International Titanium Association, 2014.
2. Lütjering G, Williams JC. Titanium: Springer, 2007.
3. Boyer R. Materials Science and Engineering: A 1996;213:103.
4. C.O. Brown, E.M. Breinan, and B.H. Kear: U.S. Patent 4,323,756,1982.
5. D.M. Keicher and W.D.Miller:Met. Powder Rep., 1998, vol. 53, p. 26.
6. G.K. Lewis, J.O. Milewski, R.B. Nemec, D.J. Thoma, M. Barbe, and 2 D. Cremers: LA-UR-95-2845, Los Alamos National Laboratories, Los Alamos, NM, 1995.
7. D. M. Keicher, J. L. jellison, L. P. Schanwald, J. A. Romero, D. H. Abbott, proceedings of the 27th International SAMPE Technical Conference, Vol. 27, Alburquerque, New Mexico, 1995, p. 1029.
8. J. Brooks, C. Robino, T. Headley, S. Goods, and M. Griffith: Solid Freeform Fabrication Proc., University of Texas, Austin, TX, 1999, p. 375.
9. T. Takeda, W.M. Steen, and D.R.F. West: Proc. ICALEO ’84, 1984, vol. 44, p. 151
10. W.M. Steen, R.M. Vilar, K.G. Watkins, M.G.S. Ferreira, P. Carvalho, C.L. Sexton, M. Pontinha, and M. McMohan: Proc. ICALEO ’92, 1992, vol. 52, p. 278.
11. Banerjee R, Collins PC, Fraser HL. Phase evolution in laser-deposited titanium chromium alloys. Metall Mater Trans A 2002;33(7):2129–38.
12. Xiao PA, Qu XH, Lei CM, et al. High temperature oxidation behaviors of Ti–Cr alloys with Laves phase TiCr2. Trans Nonfer Met Soc China 2002;12(2):200–3.
13. Ho WF, Chiang TY, Wu SC, Hsu HC. Mechanical properties deformation behavior of cast binary Ti–Cr alloys. J Alloys Compd 2009;468:533–8.

14. Ho WF, Chiang TY, Wu SC, Hsu HC. Evaluation of low-fusing porcelain bonded to dental cast Ti–Cr alloys. J Alloys Compd 2009;474:505–9.
15. http://web-o-rama.net/titanium/1properties.html
16. Welsch G, Boyer R, Collings EW. Materials Properties Handbook: Titanium Alloys: ASM International, 1993.
17. Molchanova EK. Phase Diagrams of Titanium Alloys. IPST, 1965.
18. Miller P, Holladay J. Wear 1958;2:133.
19. Margolin H, Neilson H. Modern Materials, Advances in Development and Applications 1960;2:225.
20. Collings EW. The physical metallurgy of titanium alloys: American Society for Metals, 1984.
21. R. Boyer, G. Welsch, and E. W. Collings, Materials properties handbook: Titanium alloys. Materials Park, OH: ASM International, 1994.
22. Matthew J. and Donachie Jr, Jeat treating of Titanium and its alloys, Heat Treating Progress, Volume 1, Issue, June 2001 (ASM International) June 01, 2001
23. Banerjee S, Mukhopadhyay P. Phase Transformations: Examples from Titanium and Zirconium Alloys: Elsevier Science, 2010.
24. Murray JL. Bulletin of Alloy Phase Diagrams 1981;2:174.
25. Gilbert, S., and R. Shannon. "Heat treating of titanium and titanium alloys."Mat. Sci. Rev (1992): 35-37
26. Hsu, Hsueh-Chuan, et al. "Structure and grindability of dental Ti–Cr alloys."Journal of Alloys and Compounds 476.1 (2009): 817-825.

27. Keicher DM, Smugeresky JE, Romero JA, Griffith ML, Harwell LD. Using the laser engineered net shaping (LENS) process to produce complex components from a CAD solid model. Photonics West'97: International Society for Optics and Photonics, 1997. p.91.
28. Hofmeister W, Griffith M. JOM 2001;53:30.
29. Kami, P., & Banarjee, R. (2013). Surface modifications to enhance the wear resistance and the osseo-integration properties of biomedical Ti-alloy.
30. Gopagoni, S., & Banerjee, R. (2010). Microstructure evolution in laser deposited nickel-titanium-carbon in situ metal matrix composite. Denton, Tex.: University of North Texas.
31. Mogonye, J.-E., & Scharf, T. W. (2012). Solid lubrication mechanisms in laser deposited nickel-titanium-carbon metal matrix composites.
32. Narayana, G. Hari, et al. “A phase separation reaction in a binary titanium=chromium alloy.” Metallography 4.4 (1971): 343-358
33. Keicher DM, Bullen JL, Gorman PH, Love JW, Dullea KJ, Smith ME. Forming structures from CAD solid models. Google Patents, 2002.
34. Goldenstein A, Metcalfe A, Rostoker W. Trans. ASM 1959;51:1036.
35. Narayanan GH, Luhman TS, Archbold TF, Taggart R, Polonis DH. Metallography 1971;4:343.
36. Luke CA, Taggart R, Polonis DH. Trans. ASM 1964;57:142.
37. Luhman T, Taggart R, Polonis D. Scripta Metallurgica 1969;3:777.
38. Mebed A, Miyazaki T. Metallurgical and Materials Transactions A 1998;29:739.

39. Behera, Amit Kishan. *A Study of Mechanisms to Engineer Fine Scale Alpha Phase Precipitation in Beta Titanium Alloy, Beta 21S*. Denton, Texas. UNT Digital Library.
40. Wang, Y. B., et al. "Grain size and reversible beta-to-omega phase transformation in a Ti alloy." Scripta Materialia 63.6 (2010): 613-616.
41. Samimi, Peyman, et al. "A new combinatorial approach to assess the influence of alloy composition on the oxidation behavior and concurrent oxygen-induced phase transformations for binary Ti–xCr alloys at 650 C."*Corrosion Science* 97 (2015): 150-160.
42. Liu, Huihong, et al. "Athermal and deformation-induced ω-phase transformations in biomedical beta-type alloy Ti–9Cr–0.2 O." *Acta Materialia*106 (2016): 162-170.
43. Lin, D. J., JH Chern Lin, and Chien-Ping Ju. "Effect of omega phase on deformation behavior of Ti–7.5 Mo–xFe alloys." *Materials chemistry and physics* 76.2 (2002): 191-197.
44. Ho, W. "Effect of omega phase on mechanical properties of Ti-Mo alloys for biomedical applications." *Journal of Medical and Biological Engineering* 28.1 (2008): 47.
45. Zhang, Bing et al. “A study on the beta and omega phases in a Ti-Al-Cr alloy." *Scripta metallurgica et materialia* 30.4 (1994): 399-404.
46. Dubinskiy, Sergey, et al. "In situ X-ray diffraction study of athermal and isothermal omega-phase crystal lattice in Ti-Nb-based shape memory alloys." *Materials Letters* 168 (2016): 155-157.
47. Guo Shun, et al. ‘Microstructural evolution and mechanical behavior of metastable β-type Ti–25Nb–2Mo–4Sn alloy with high strength and low modulusMicrostructural

evolution and mechanical behavior of metastable β-type Ti–25Nb–2Mo–4Sn alloy with high strength and low modulusretain-->."*Progress in Natural Science: Materials* International 23.2 (2013): 174-182